

MULTISPECTRAL SYNTHETIC SCENE GENERATION USING
ATMOSPHERIC PROPAGATION AND THERMODYNAMIC MODELS

by

Carl Salvaggio

A thesis
submitted in partial fulfillment
of the requirements for the
Doctor of Philosophy degree

State University of New York
College of Environmental Science and Forestry
Syracuse, New York

June 1994

Approved:
Faculty of the graduate program in
Environmental and Resource Engineering

Dr. Michael Duggin, Major Professor

Dr. Larry Van Druff, Chairperson,
Examining Committee

Dr. Robert Brock, Faculty Chairperson

Dr. Robert Frey, Dean, Instruction and
Graduate Studies

Dr. Robert Brock, Director, Division of
Environmental and Resource Engineering

I. ABSTRACT

SALVAGGIO, CARL. Multispectral synthetic scene generation using atmospheric propagation and thermodynamic models. Typed and bound thesis. 140 pages. 12 tables. 87 figures. 1994.

With today's economy and unprecedented rate of technological advancement, ideas for new remote sensing systems outpace the abilities of and funding levels for researchers and engineers to build and test these platforms. For these reasons, accurate modeling of new systems becomes a requirement. This document represents the current status of a first-principles physics-based synthetic image generation model, DIRSIG, capable of producing the radiance field reaching the front-end of an airborne or terrestrial imaging system. This model accounts for the major material interaction effect for objects in the scene in both the reflective and emissive portions of the electromagnetic spectrum, their thermodynamic behavior in a natural environment, and the propagation of energy through the atmosphere.

The model is demonstrated to produce viable imagery in both the qualitative and quantitative sense. In the thermal infrared portion of the spectrum, results are demonstrated in which temperatures are shown to be modeled within truth by 5°C in the longwave-infrared and 6°C in the midwave-infrared regions. Many of the phenomena observed in infrared imagery are also demonstrated including background radiance effects and thermal shadows (signatures). In developing a model to work in these two thermal infrared passbands, the model naturally had the capabilities to work in the reflective regions. Example imagery from the reflective portion of the spectra is presented illustrating the qualitative fidelity of the model in this region, however, no quantitative analysis was conducted at this time.

Author's name in full: Carl Salvaggio

Candidate for the degree of Ph.D. Date: June 1994

Major Professor: Dr. Michael Duggin

Faculty of the Division of Environmental and Resource Engineering

State University of New York, College of Environmental Science and Forestry, Syracuse, New York

Signature of Major Professor: _____

II. ACKNOWLEDGMENTS

I would like to thank all the members of the Digital Imaging and Remote Sensing Laboratory at the Rochester Institute of Technology for their assistance in all phases of this work. I would especially like to thank Dr. John Schott for his guidance in many aspects of the development of this model and for his encouragement over the years which has greatly influenced my career development.

For his unparalleled knowledge of the UNIX operating system and the C programming language, I want to thank Geordie Klueber for his help and patience in tracking down the many "bugs" which plagued this model during its development.

I would like to acknowledge the Office of Development and Engineering and the Office of Research and Development of the Central Intelligence Agency, the US Department of Energy, NASA's Jet Propulsion Laboratory, ITEK Corporation and the Federal Systems Division of Eastman Kodak Company for their financial and technical support during the development of this model. I hope my academic approach to this problem will prove to be useful in the applied scenarios for which they intend to use it.

I would also like to thank Dr. Michael Duggin for exposing me to new areas of study and to new ideas. I always enjoy our technical conversations and hope they will continue far into the future.

Finally, I would like to thank the remaining members of my committee; Dr. Paul Hopkins, Dr. Robert Brock, Dr. Lee Herrington, Dr. William Stiteler, Mr. Bill Johnson, Dr. Craig Davis and Dr. Larry Van Druff for serving on my steering and examination committees and being supportive of my efforts to finish this degree.

III. DEDICATION

To my wife, Nanette, whose unconditional support and devotion has allowed me to live out this dream and to my son, Philip, who has had to put up with a part-time dad for far too long.

IV. TABLE OF CONTENTS

I.	ABSTRACT	i
II.	ACKNOWLEDGMENTS	ii
III.	DEDICATION	iii
IV.	TABLE OF CONTENTS.....	iv
V.	LIST OF TABLES	vi
VI.	LIST OF FIGURES.....	vii
1.0	INTRODUCTION	1
2.0	EXPERIMENTAL APPROACH	4
2.1	Literature review	5
2.1.1	Thermal IR SIG activities at RIT	8
2.1.2	Project statement and objectives	10
2.2	Thermodynamic modeling.....	11
2.2.1	Solar insolation.....	15
2.3	Ray tracing algorithms	16
2.3.1	Ray-box intersections	19
2.3.2	Ray-plane intersections	22
2.3.3	Point-polygon inside-outside testing.....	24
2.4	Radiance field reaching the sensor.....	28
2.4.1	Downwelled sky radiance.....	37
2.4.2	Sky obstruction factor (shape factor).....	42
2.4.3	Radiometric interaction with clouds (transmissive objects).....	46
2.4.4	Correction of atmospheric profiles for surface weather data.....	50
2.4.5	Example propagation scenario.....	51
2.5	Integration of submodels	65
2.5.1	Geometric data base (.gdb) and material data base (.mat).....	65
2.5.2	Scene node parameters (.snd) and weather data base (.wth).....	67
2.5.3	Viewing (.adv) and sensor parameters (.sen)	67
2.5.4	Radiometry data base (.rad) file.....	69
2.5.5	Ray tracer algorithm flow	69
2.5.6	Target specularity	70
3.0	RESULTS AND DISCUSSION.....	72
3.1	Validation of the THERM submodel.....	86
3.1.1	Weather parameters	89

3.1.2	Object parameters	90
3.2	Validation of radiometric and thermal performance of DIRSIG	92
3.2.1	Radiometry sensitivity.....	93
3.2.2	DIRSIG final scene validation	96
4.0	CONCLUSIONS AND RECOMMENDATIONS.....	103
5.0	REFERENCES.....	105
VITA	140

V. LIST OF TABLES

Table 2.2-1	Input parameters to the DCS THERM model.....	13
Table 2.4-1	Origin of individual parameters used in the radiometric equations.....	36
Table 2.4.3-1	Parameters defining the geometric parameters governing the cloud models used in the LOWTRAN 7 code.....	50
Table 3.1-1	List of THERM's input variables and their sources.....	87
Table 3.1.1-1	Weather parameter errors and resulting temperature errors.....	89
Table 3.1.2-1	Material parameter errors and resulting temperature errors.....	90
Table 3.1.2-2	Root mean-square errors between actual thermistor measurements and THERM prediction of temperature for the 22-23 June 1992 data set.....	92
Table 3.2.1-1	Error associated with the individual parameters in the radiometric equations for the longwave and midwave infrared bandpass regions.....	94
Table 3.2.1-2	Error contribution in W/m^2sr to the total radiance for the longwave infrared of each of the parameters in the radiometric equation. The total error in radiance is also converted to apparent temperature.....	94
Table 3.2.1-3	Error contribution in W/m^2sr to the total radiance for the midwave infrared of each of the parameters in the radiometric equation. The total error in radiance is also converted to apparent temperature.....	95
Table B-1	Thickness of the default cloud layers used in the LOWTRAN 7 code.....	118
Table D-1	Material parameters (June 1992).....	139

VI. LIST OF FIGURES

Figure 2.2-1	Typical temporal (diurnal) meteorological data required for input to thermodynamic model.....	14
Figure 2.2-2	Actual object temperature versus THERM predicted temperature as a function of time.	15
Figure 2.2.1-1	Illustration of the computation of the modifying terms for direct solar insolation as input to the THERM model.....	16
Figure 2.3-1	A single object contained in a bounding volume, with additional bounding volumes around selected parts.....	18
Figure 2.3-2	Tree search used to facilitate the efficiency with which a search is conducted to find the intersected facet. The object and part levels within the tree are delineated by bounding volumes in the ray tracing process.	19
Figure 2.3.1-1	Illustration of ray-box intersection concept with a "hit" and a "miss" shown.	20
Figure 2.3.1-2	Illustration of the ray/box intersection testing algorithm (Haines, 1987).....	22
Figure 2.3.2-1	Illustration of plane-ray intersection testing: Case 1 - the ray does not intersect the plane when the angle between the ray and the facet normal is less than 90°; Case 2 - the ray does intersect the plane when the angle between the ray and the facet normal is greater than 90°.....	25
Figure 2.3.3-1	Test for whether or not an intersection point is contained within a polygon. This illustration shows three crossings of the +U' axis indicating that the point is within the polygon (Haines, 1987).	26
Figure 2.4-1	Ray interaction types allowed for by the DIRSIG model.....	29
Figure 2.4-2	Relevant angles needed to simulate the radiometric interactions which are simulated by the DIRSIG model.	33
Figure 2.4-3	Radiance database structure used for computation of the radiance field reaching the sensor.	35
Figure 2.4.1-1	Downwelled sky radiance database formed from repeated runs of the MODTRAN atmospheric transmission and path radiance code. The model is run in the vertical or slant path to space mode.	38
Figure 2.4.1-2	Spherical plot illustrating the downwelled sky radiance field in the 8 to 14 micron bandpass (longwave infrared portion of the spectrum, 750 to 1250 cm^{-1}). Simulated radiance produced for the following conditions: 39°46'24"N latitude, 84°06'32"W longitude, day number 172, 9:00AM local time (14:00 GMT).	39
Figure 2.4.1-3	Spherical plot illustrating the downwelled sky radiance field in the 0.4 to 0.7 micron bandpass (visible portion of the spectrum, 14200 to 25000	

	cm ⁻¹). Simulated radiance produced for the following conditions: 39°46'24"N latitude, 84°06'32"W longitude, day number 172, 9:00AM local time (14:00 GMT).	40
Figure 2.4.1-4	Illustration of the bilinear interpolation method for determining the downwelled sky radiance at a particular azimuth (ϕ) and zenith (θ) angle.	41
Figure 2.4.2-1	Background objects obscure a portion of the hemisphere above a target limiting the portion of the downwelled "sky radiance" field which can fall onto a target.	45
Figure 2.4.3-1	Simulated radiometric interactions caused by the presence of clouds in the scene.	47
Figure 2.4.3-2	Determination of object thickness along the path of propagation.	48
Figure 2.4.4-1	Illustration of possible modifications to descriptive atmospheric profiles of temperature.	51
Figure 2.4.5-1	Illustration of the spectral vectors produced by the SVGM.	53
Figure 2.4.5-2	Interactions between those vectors shown in Figure 2.4.5-1 in the formation of the sensor reaching radiance field.	55
Figure 2.5.1-1	Overall description of the ray tracer submodel's interactions with the supporting data structures.	66
Figure 2.5.5-1	Illustration of the ray tracer algorithm flow for a single pixel.	70
Figure 3-1	A pan visible (0.4 to 0.7 μ m) image for the Foxbat fighter scene created at ITEK's image simulation facility.	72
Figure 3-2	AutoCAD wire frame representation of the physical model created in the scene simulation facility.	73
Figure 3-3	A close-up view of a single facet with its associated attribute list. Attributes shown are material name, material code, attribute name, default facet temperature, facet thickness, self-generated power, exposed area, and three blank fields for future use.	74
Figure 3-4	Primary target material map illustrating the material code of which each facet is represented in the geometry database.	75
Figure 3-5	Secondary background material map illustrating the material code for the facet which makes up the background for a specular bounce from the current target facet (if one exists).	75
Figure 3-6	Sun/shadow maps depicting the illumination state for the current target pixel at the time of image simulation.	76
Figure 3-7	Sun/shadow maps depicting the illumination state for the current target's background facet (if there is one) at the time of image simulation.	76
Figure 3-8	Temperature map for the target as computed by THERM using the specified weather history and sun/shadow history for the current pixel.	77

Figure 3-9	Temperature map for the target's background (if there is one) as defined by an initial run of THERM (with no regard for sun/shadow history, e.g. it is kept sunlit).	77
Figure 3-10	Ray interaction map illustrating the type of radiometry computation to be carried out for each pixel (either a diffuse hit, a specular bounce to the sky, a specular bounce to a background object, or a missed scene).	78
Figure 3-11	Integrated angular emissivity over the bandpass being simulated for the target pixel.	78
Figure 3-12	Integrated angular emissivity over the bandpass being simulated for the target's background facet (if there is one).	79
Figure 3-13	Angle between the primary facet normal and the ray cast from the sensor to the primary target hit point (θ in the radiometric computations).	79
Figure 3-14	The sky obscuration factor for each pixel in the scene used to modify the downwelled sky radiance for diffuse pixels.	80
Figure 3-15	Simulated radiance field reaching the front end of the sensor from the Foxbat scene propagated through the atmosphere (the image simulates an acquisition with a sensor in the 8 to 13.3 micron bandpass region, at 10AM local time, on 6/24/87 at 39°46'24"N latitude and 84°06'32"W longitude).	80
Figure 3-16	True-color images depicting the scenes a westward viewing sensor would see at (a) 08:00, (b) 12:00, (c) 17:00, and (d) 19:00 local time. The plots beside the images illustrate the magnitude of the downwelling sky radiance for these acquisition times (the images simulate acquisitions with a sensor in the 0.4 to 0.5 micron, 0.5 to 0.6 micron, and 0.6 to 0.7 micron bandpass regions, on 6/24/87 at 39°46'24"N latitude and 84°06'32"W longitude).	82
Figure 3-17	A midwave (3 to 5 micron) infrared image of a desert scene illustrating the presence of both directly illuminated solar shadows as well as differential background heating caused by previous sun/shadow history effects (the image simulates an acquisition at 18:00 local time, on 6/24/87 at 39°46'24"N latitude and 84°06'32"W longitude).	84
Figure 3-18	Side-by-side comparison of a longwave infrared image collected using an Inframetrics 600L with a predicted scene from the DIRSIG model (the image simulates an acquisition at 12 noon local time, on 6/23/92 at 43°05'00"N latitude and 77°40'00"W longitude).	85
Figure 3-19	Side-by-side comparison of a midwave infrared image collected using a Mitsubishi IR 5120A with a predicted scene from the DIRSIG model (the image simulates an acquisition at 8:00AM local time, on 6/23/92 at 43°05'00"N latitude and 77°40'00"W longitude).	85
Figure 3.1-1	Rooftop collection experimental scene design carried out on 22-23 June 1992.	87
Figure 3.1-2	LWIR image derived temperatures vs. thermistor measurements for asphalt, 22-23 June 1992.	88

Figure 3.2.2-1	Photograph of validation scene taken from rooftop of RIT's Center for Imaging Science and enlarged. Objects used for validation analysis are labeled.	97
Figure 3.2.2-2	LWIR sensor blackbody calibration data.....	98
Figure 3.2.2-3	MWIR sensor blackbody calibration data.....	98
Figure 3.2.2-4	DIRSIG predicted versus measured LWIR radiance for (a) water, (b) the car roof, and (c) asphalt.	99
Figure 3.2.2-5	Root mean-square radiance error as a percent of average radiance over the 24-hour collection period.	100
Figure 3.2.2-6	Root mean-square apparent temperature error over the 24-hour collection period.	100
Figure 3.2.2-7	Truth vs. DIRSIG radiance values for water in the MWIR bandpass for June 23, 1992.	101
Figure B-1	Extinction coefficients derived for the different cloud types modeled in LOWTRAN7 code.	120
Figure B-2	Extinction coefficients derived for the different cloud types modeled in LOWTRAN7 code emphasizing absorption lines in the region between 350 to 10000 cm^{-1}	121
Figure C-1	Aluminum oxide angular emissivity.	122
Figure C-2	Polished aluminum angular emissivity.....	122
Figure C-3	New asphalt angular emissivity.	123
Figure C-4	Old asphalt angular emissivity.....	123
Figure C-5	Bare wood angular emissivity.....	124
Figure C-6	Blue panel angular emissivity.....	124
Figure C-7	Brick angular emissivity.	125
Figure C-8	Concrete angular emissivity.	125
Figure C-9	Glass angular emissivity.	126
Figure C-10	Gloss paint on steel angular emissivity.....	126
Figure C-11	Grass angular emissivity.	127
Figure C-12	Gravel angular emissivity.....	127
Figure C-13	Green panel angular emissivity.	128
Figure C-14	Grey panel #1 (lightest grey) angular emissivity.	128

Figure C-15	Grey panel #2 angular emissivity.	129
Figure C-16	Grey panel #3 angular emissivity.	129
Figure C-17	Grey panel #4 angular emissivity.	130
Figure C-18	Grey panel #5 (darkest grey) angular emissivity.	130
Figure C-19	Metallic paint on steel angular emissivity.....	131
Figure C-20	Plant leaf angular emissivity.....	131
Figure C-21	Plexiglass angular emissivity.....	132
Figure C-22	Polycarbonate angular emissivity.	132
Figure C-23	Red panel angular emissivity.	133
Figure C-24	Radome paint #1 angular emissivity.....	133
Figure C-25	Radome paint #2 angular emissivity.....	134
Figure C-26	Radome paint #3 angular emissivity.....	134
Figure C-27	Radome paint #4 angular emissivity.....	135
Figure C-28	Radome paint #5 angular emissivity.....	135
Figure C-29	Radome paint # 6 angular emissivity.....	136
Figure C-30	Sand angular emissivity.	136
Figure C-31	Roof shingles angular emissivity.	137
Figure C-32	Soil angular emissivity.	137
Figure C-33	Tire rubber angular emissivity.	138
Figure C-34	Water angular emissivity.....	138

1.0 INTRODUCTION

Recent years have seen a growing use of imagery acquired using electro-optical sensors. From the Gulf War where image sensors delivered missiles to their targets to the use of space-based systems to track ecological damage instilled by man's disrespect for our planet's environment, imagery is an essential part of all portions of our lives. The systems which acquire this imagery are often very expensive to build and operate. Training analyst's to use the imagery from these systems is a time-consuming process. For these two reasons, as well as many others, the need for synthetically generated imagery has become a top priority for many government, industrial, and academic research and development teams. Since much of the utilization of these simulation systems is to produce imagery from classified systems, many models are unavailable to the academic community as well as the general public. In response to this fact, the efforts described in this work summarize many years of research and development directed toward the creation of a synthetic scene generation model. The Digital Imaging and Remote Sensing laboratory's Image Generation model (DIRSIG) is the result of this effort and is available to the community at large.

DIRSIG is a full spectrum radiometrically rigorous image generation model. Directed at the creation of accurate radiance images reaching the front end of a sensor which exhibit proper phenomenology, DIRSIG attempts to account for most of the first-order physics-based phenomena that affect this propagation process. Starting with a computer generated three-dimensional model of a scene DIRSIG predicts the surface-leaving radiance. The radiance from a target is due to its kinetic temperature, its reflective properties and the energy falling onto the surface from the sun. Downwelled sky radiance due to scattering and emission, and energy reflected and emitted from background objects in the vicinity of the target also contribute to the field. This radiance field is then propagated through the atmosphere where it is attenuated by scattering and absorption and where path radiance due to atmospheric scattering and emission is added.

Originally designed as a thermal infrared image generation model DIRSIG pays particular attention to material properties and environmental effects which contribute to the prediction of target temperatures. To predict a target's temperature, a portion of the Air Force Infrared Simulated Image Model (AIRSIM) named THERM is utilized. THERM is a linear differential temperature generation model written by DCS Corporation, 1990, which predicts the temperature of a single target surrounded by a well defined environment. THERM is a radiative model which

does not account for conductive effects that adjacent targets may have on one another. THERM predicts temperature based on thermodynamic computations which account for a material's thermal conductivity, specific heat, thickness, exposed area, self-generated power, and visible and thermal emissivity. Also included is a detailed weather history with data on pressure, temperature, relative humidity, wind speed, direct and diffuse solar insolation for a period of more than 24 hours prior to the time of temperature prediction.

The predicted radiance field leaving the surface results from radiometric computations involving a target's emissivity/reflectivity. These terms are defined spectrally as well as a function of propagation angle. The MODTRAN atmospheric transmission and path radiance model (Berk *et al.*, 1989) is used to define the downwelled solar and emitted radiance field and the attenuating properties of the atmosphere. Attention is also paid to obstructions such as clouds which will influence the upwelling radiance field due to their absorptive, reflective, scattering and emissive properties. A full treatment of spectral extinction is implemented to account for the effects of these transmissive objects.

A simple sensor model accounts for the gain and bias applied to the detector's signal as well as a normalized spectral response function. With this radiance field reaching the front end of the sensor predicted, future work can be directed at the development of detailed sensor models. These models should account for sensor system degradations such as modulation transfer functions for optical and electronic components, sampling characteristics of the detector, image compression and reconstruction artifacts, and new image processing algorithms directed at the enhancement and exploitation of imagery.

The DIRSIG model gives researchers the capability to completely model the entire image chain without actually building a sensing system. The model performs full spectral computations over the wavelength limits of 0.4 to 20 μm . Scientists and engineers can use this model to perform trade-off analysis in the sensor design process and to visualize the impact of their decisions on the final image produced. DIRSIG can be used to perform "what-if" experiments to determine correct image interpretations. For example, an image analyst can use this model to decide whether the appearance of the fuel bladders in the wings of an aircraft result from the fact that these tanks were just filled or because the prevailing winds are very strong.

In reviewing the available literature, the DIRSIG model described in this work is among the most rigorous in the treatment of radiometry. Other models produce more detailed scenes with

complex backgrounds suitable for automatic target recognition (ATR) algorithm testing, some produce less accurate scenes at near real-time speeds for flight simulation applications, while remaining models fall somewhere in between. The DIRSIG model is designed to predict many of the physical interactions which produce an upwelling radiance field at the expense of computation time. Detailed backgrounds and targets can easily be obtained with this model at the added expense of more computation time. DIRSIG represents a major contribution to the scene generation community for applications which require detailed radiometric accuracy and phenomena prediction.

2.0 EXPERIMENTAL APPROACH

Over the past 25 years, the need for artificially created images has developed in such applications as animation, computer-aided design and manufacturing (CAD/CAM), and flight simulation. Most of these applications developed within the computer graphics community are collectively known as synthetic image generation (SIG) models. All of these techniques create images in the visible portion of the electromagnetic spectrum. To generate images over the entire electromagnetic spectrum, including the thermal infrared region, different factors need to be considered making it a challenge to produce radiometrically accurate synthetic images.

Creation of credible computer images requires realistic 3-D modeling where realism is, in the visible wavelengths, based largely on the lighting cast upon objects within the scene. Simulating proper illumination conditions is therefore a crucial and complex task for radiometrically accurate images. The path this illuminating radiation takes must be traced from its source to the various objects in the scene. The radiation is then absorbed, transmitted, or scattered from the objects.

Radiation leaving an object can be absorbed, transmitted, or scattered in passing through the atmosphere. Therefore, atmospheric propagation must be included to realistically synthesize a scene. Atmospheric models, such as LOWTRAN (Kneizys *et al.*, 1988), MODTRAN (Berk *et al.*, 1989) and FASCODE (Clough *et al.*, 1986) are used to simulate the effects of the atmosphere on radiation. Atmospheric modeling combined with SIG allows for the creation of radiometrically accurate synthetic images.

The apparent brightness of an object in the thermal IR is primarily due to its temperature and its material characteristics. The thermal environment of an object also has a major impact on its thermal IR appearance. The thermal response measured by a remote sensor often permits assessment of the type and/or condition of features. The specific set of these responses are often called thermal signatures (Lillesand and Kiefer, 1987). Sometimes an object's environment may cause a change in the object's temperature and thus alter its thermal signature. For example, an object's temperature may rise due to exposure to sunlight, being near other hot objects, or from internal heat sources (e.g. an engine). Other additional environmental variables that effect an object's temperature include wind speed and cloud cover. All of these factors must be addressed for accurate thermal IR SIG. This section contains a review of the literature illustrating how some of the problems have been addressed by others.

2.1 Literature review

This section contains a review of the current literature summarizing aspects of available thermal IR SIG models. This review will allow the reader to develop a sense of what capabilities exist. Many of the models have classified components or are corporate confidential, so the literature is often limited to general descriptions making it difficult to evaluate the true capabilities of the approach. These same limitations often make it difficult to incorporate components of these existing models into improved methodologies. Within these constraints DCS Corporation and Schott, 1987, conducted an extensive literature review of models related to thermal IR SIG which included CAD/CAM models, IR radiation propagation models, thermodynamic models, energy-matter interaction models, ray tracing methods and IR sensor models. They described over 30 models. Many of these models have several submodels. In many cases, these models only perform some part of the overall requirements or are very specific to a particular set of targets or sensors. The summary of the more useful approaches which follows draws heavily on the review by Shor, 1990.

Most existing thermal IR SIG models require similar types of data for input. To properly simulate an object in an environment, the following are required: (1) a geometrical representation of an object, (2) some form of an atmospheric transmission model, and (3) material characteristics (e.g. emissivity or absorptivity). Some of the more elaborate simulators also include thermodynamic models and pixel-to-pixel texturing capabilities.

Georgia Tech has developed a good example of thermal IR SIG. This section will use the Georgia Tech's work as a case study and look at other researchers who have used significantly different approaches.

The Electromagnetics Laboratory of Georgia Tech Research Institute (GTRI) has developed a program for generating synthetic images of scenes called the Georgia Tech Visible and Infrared Synthetic Imagery Testbed, GTVISIT (Cathcart and Sheffer, 1988; Sheffer and Cathcart, 1988). GTVISIT requires the outputs from other modeling programs, such as GTSIG and IRMA which are also discussed in this section.

With GTVISIT, scenes are separated into two component types: a gridded terrain background and a faceted object placed into that scene. A gridded background means that the area has been divided into cells or grid blocks. Backgrounds may be terrain, ocean, sky, or a combination

of the three.

GTVISIT uses four gridded databases: feature (material type), elevation, radiance, and thermal IR reflectance. The feature and elevation data may come from real-world sources (such as satellite imagery and elevation measurements), from synthetic data, or from a hybrid combination. The radiance and thermal IR reflectance data are generated from the temperature and/or reflectivity of each material. Such assignments typically are obtained from measured data or thermal predictions.

GTVISIT creates images by using a z-buffer algorithm. Z-buffering is a computer graphics technique used to display (or not display) hidden surfaces. First, elevation databases are projected upon a view screen and the sensor-target range values for the overlapping pixels are compared (in the event of multiple projections on a pixel). Second, the objects are projected in the same way and visibility tests from the point of view of the sensor are performed. If any part of the scene element is visible, it is projected facet-by-facet.

Next, the atmospheric attenuation and emission along the viewing path are computed. To save computation time, GTVISIT pre-computes radiance values for 12 different orientations of each object in the scene. Radiance values are also pre-computed and assigned to each vertex of a 4-sided rectangular facet. If a pixel lies inside the facet, the pixel radiance is computed by bilinear interpolation. The code can include backgrounds and diurnal variation, as well as dynamic processes such as fire, smoke, and dust clouds.

GTSIG, a separate modeling program developed by Georgia Tech, computes the thermal radiance of objects from first-principles physics. It employs a 3-D thermal network analyzer and a multi-surface radiosity technique in the computations. The physical processes included in the thermal model are solar and sky radiation (direct and occluded), mass-transfer processes (evaporation, condensation, sublimation, and precipitation), fluid flow effects, shadowing, and multi-surface reflections.

IRMA was developed for the Air Force by Grumman Aerospace Corporation (Botkin, 1981). It is a semi-empirical, one-dimensional heat transfer approach for computing the radiance for each facet of an object based on thermal history of the object. An IRMA model is easier to construct than a GTSIG model and is used when solar radiance and self-shadowing effects are important.

Computations for GTSIG are reasonably robust, but it does not account for angular emissivities which are critical in the infrared (Schott, 1986). The pre-computation of radiance values is acceptable, but is inappropriate when attempting to generate an exact radiometric image. GTSIG does not address target-background radiance interactions in the radiometry computations but Georgia Tech has suggested this improvement. Solar shadow history for each pixel is also not treated by this model.

Evans and Sutherland Computer Corporation has developed a real-time system to simulate Forward Looking Infrared (FLIR) imagery (Biesel and Rohlfing, 1987). By assuming thermal equilibrium of the object with its environment, and limiting temperature to 256 distinct values, real-time scene simulation may be achieved. Object warming is limited to solar radiation or diffuse sky contributions. Specular reflection is neglected and atmospheric attenuation is calculated using Beer's law approximations. The Evans and Sutherland approach provides real-time simulation at the expense of precise radiometry. This type of approach is often suitable for tactical purposes but is of less value for reconnaissance applications.

Nichols Research Corporation has simulated high spectral and spatial resolution of a downlooking thermal IR sensor (Dunn *et al.*, 1987). Their technique addresses hardware limitations of large-scale images. Z-buffering techniques are used to superimpose the contribution of each objects radiance to a final thermal IR SIG image. The simulator was constrained by the limitations of the computation environment.

The US Army Night Vision and Electro-Optics Laboratory (NVEOL) has developed a thermal IR model that predicts the thermal radiation distributions of a scene (Kornfeld, 1987). The thermal signatures are calculated via an empirical model based upon measured data. A specialized atmospheric attenuation routine (LTR) was validated against LOWTRAN 6. The technique has the limitation that it relies on the artistic talents of the model builder to create individual frames, making it difficult to use for the general practitioner.

Grumman Corporate Research Center has used mathematical textural functions along with simple surfaces to simulate features such as hills, trees, and clouds in the visible wavelengths (Gardner *et al.*, 1987). The US Army Tank and Automotive Command (TACOM) has extended this technique to the thermal IR by substituting statistical characteristics of measured thermal IR data for the texture function. This approach may be used for low interest background regions for tactical applications, but generally a more complete modeling will again be required for

reconnaissance.

Aerodyne Research, Inc. has developed code (AERIE) for simulating aircraft with various backgrounds (Stets *et al.*, 1988). AERIE is very specialized for particular targets and has the ability to calculate the thermal plume of the exhaust from aircraft engines. It can also include the influence of clouds on a target. The radiometry is calculated using SPIRITS 2.0, (Spectral Infrared Imaging of Targets and Scenes). Again, LOWTRAN 6 is used for atmospheric attenuation computation.

The review presented here of currently available models has pointed out their capabilities in an effort to highlight the features which may be available and desirable in improved models. At the same time, several limitations should be noted. First, most of the models are not spectrally dependent (i.e. the solution is not done wavelength-by-wavelength for all dependent variables). Second, many of the thermal models ignore the thermal history of an individual pixel in terms of temporal environmental variables such as sun/shadow history, air temperature, wind speed, etc. Third, most of the models do not include emissivity values that are a function of view angle. Fourth, most of the models do not include a capability to deal with specular reflections to a sky whose radiance varies with angle or to background objects. Finally, many of the models are not heavily based on fundamental physical principles making them difficult to validate, integrate or update. With this context in mind, the Digital Imaging and Remote Sensing laboratory (DIRS) at Rochester Institute of Technology has been working with and evolving certain thermal IR SIG tools for several years aimed at filling gaps in the SIG modeling process.

2.1.1 Thermal IR SIG activities at RIT

The Digital Imaging and Remote Sensing laboratory, DIRS, at Rochester Institute of Technology's Center for Imaging Science has had a long term interest in absolute radiometric calibration of thermal IR imagery with a special interest in correcting atmospheric effects (Byrnes and Schott, 1986; Schott and Schimming, 1981; Schott and Volchok, 1985). This interest in quantitative measurements led to development of methods and devices for measuring thermal IR normal and angular hemispheric emissivity values (Schott *et al.*, 1990). These bandpass values were then used to estimate how emissivity variations affected imaging sensors as described in Schott, 1986. The synthetic scenes used at this time were simple 2-D silhouettes with temperature values assigned to each segment. Bandpass values of atmospheric

transmission and upwelled and downwelled atmospheric radiance were also included in these models. While the SIG process used in these studies was primitive, the process clearly demonstrated the need for inclusion of emissivity effects in thermal IR scene generation. This work was extended by Schwartz *et al.*, 1985, to include the effects of specular reflection of background surfaces and downwelled sky radiance. These scenes were still very "flat" with each scene segment treated the same. This effect was addressed by Schott and Salvaggio, 1989, who describe incorporating brightness variations within segments by taking texture from images of laboratory physical models or from actual thermal IR images. This work was the first effort to make the thermal IR SIG images begin to look real. Previous work had been concentrated on using SIG to help visualize target-to-background signature assessments and to help "visually" evaluate the importance of various quantitative improvements to the radiation propagation models. As part of these initial efforts to improve the "realism" of the SIG images, Schott and Salvaggio, 1987, used a sensor response model incorporating image degradation using asymmetric two-dimensional convolution kernels to simulate atmospheric and optical detector sampling and scanning effects on the modulation transfer function of the imaging sensor. In addition, an ability to add random and periodic detector noise was developed and implemented. As the scenes became increasingly "real," the interest in simulation and its applications expanded. A full three-dimensional scene generation capability was needed to permit visualization of more diverse and complex scenes. This was achieved by incorporation of CAD/CAM 3-D wire frame models and ray tracing techniques as reported by Warnick *et al.*, 1988. In parallel with these improvements, a series of small scale validation efforts kept pace with and paralleled the advances in the SIG modeling, radiation propagation modeling, and materials measurement. The emissivity modeling was extended by Schott *et al.*, 1990, to field measurements and to encompass 3-5 μm , as well as the 8-14 μm region with improved accuracy achieved. In addition, improved methods for measurement of spectral bi-directional reflectance distribution functions (BRDF) in the visible and SWIR region were demonstrated by Feng, 1990. Schott and Salvaggio, 1989, performed a validation study of the surface-leaving radiance portion of the model, validating the treatment of angular emissivity effects and the background and sky radiance equations used in the models. Shor *et al.*, 1990, performed a preliminary validation of the radiometry and ray tracing scheme used in conjunction with the 3-D wire frame modeling.

These studies affirmed the basic quantitative integrity of the methodology used but suggested the need for a variety of improvements. One of the most critical needs was for the incorporation of a thermal model so that temperatures could be predicted for each scene element, facet, or pixel based on object parameters and scene conditions. A second major improvement called for

the inclusion of solar reflection effects. The modeling described above had been restricted to the LWIR bandpass where solar reflection and scattering effects are vanishingly small compared to self-emission effects. However, in the midwave region and at shorter wavelengths, solar reflection becomes very important and must be included in the SIG process. Spector *et al.*, 1991, completed a study which included validation of a thermodynamic model which could be used in the SIG process and which appeared to be quite accurate, at least for passive objects. Salvaggio *et al.*, 1991, also completed a study which was aimed at generation of spectral atmospheric radiation propagation and energy matter interaction terms needed for modeling solar and thermal radiometric effects associated with horizontal surfaces. This model could be modified for use in the SIG process and could also potentially be used spectrally to improve the quantitative accuracy of the process. This spectral treatment is particularly important in wavelength regions where the source, sensor or atmospheric spectral response is varying such as in the MWIR or near the ozone absorption line in the LWIR.

2.1.2 Project statement and objectives

Based on the assessment of the state of the art as described in the literature review (Section 2.1) and the status of the work of the DIRS laboratory at RIT, a decision was made to assemble a SIG capability with all the base line capability for end-to-end image generation. This model would take advantage of existing approaches and software whenever practical and would emphasize the generation of quantitative radiometrically correct scenes. The objectives of the model were as follows: it should 1) function over a wide portion of the electromagnetic spectrum from 0.4 to 20 μ m, 2) emphasize radiometry in terms of dealing with as much radiometric phenomena as necessary to achieve as much radiometric accuracy as practical, 3) be capable of dealing with scene elements which would be observed by high resolution airborne systems, 4) use first principles physical models as much as possible, and 5) use simple target and sensor models in the initial versions to emphasize phenomena.

The approach taken in this work pays strict attention to the physical phenomena affecting the radiance field reaching the front end of a remote sensing system. As most ray tracing/synthetic scene generation models try to achieve "realistic" looking scenes as far as appearance is concerned, the model presented here strives to achieve the correct absolute radiance value for each pixel at the expense of "realistic" looking scenes. With more effort in the up front 3-D model building process, "realism" can be obtained at the expense of run-time. For now, scenes

will be kept fairly simple in order to allow radiometry to be treated more rigorously.

The following sections will deal with the major submodels necessary to construct a full spectrum synthetic scene generation model. These models include a thermodynamic model for prediction of target and background temperatures, a ray tracing submodel to render a two-dimensional image from a three-dimensional wire frame model, and a radiometry model which accounts for energy-matter interactions of scene elements as well as propagation of the radiance field through the atmosphere. Finally, the interactions between these submodels and the methods for tying them together into a model named the Digital Imaging and Remote Sensing laboratory's Image Generation model, DIRSIG, will be discussed.

2.2 Thermodynamic modeling

The fundamental purpose of thermodynamic modeling is to calculate the time-dependent temperatures of objects within the scene as influenced by their environment. This section contains an overview of the thermodynamic model, THERM, which is part of the Air Force Infrared Simulated Image Model (AIRSIM). THERM is a linear differential temperature generation model written by DCS Corporation, 1990, and tested for validity at RIT (Spector *et al.*, 1991). Temperatures are calculated separately for each object facet as a function of time based on first principles models. These models determine the rate of heat transfer corresponding to a specific temperature difference between an object and its environment. The assumption is made that a facet is thermally independent of the other facets and that each exhibits isothermal behavior over its entire surface. THERM predicts an object's thermal signature based on solar parameters, meteorological conditions, and material properties. As a stand-alone model, THERM has been shown to produce accurate temporal predictions of temperatures of real world objects.

THERM requires various object and environmental parameters for input to the linear differential heat transfer equation in order to calculate the effects of radiative heat exchange, convection, conduction (within facet only), and absorption of solar insolation. Each parameter impacts in some way the temperature of the various objects within the scene as a function of time. The object parameters consist of (1) heat capacity, thermal conductivity, and thickness to determine the thermal mass (which impacts the rate at which the temperature of an object can react to a

given amount of heat), (2) self-generated power (to allow for internal heat sources), (3) exposed area, slope and azimuth angles (to describe the facet's geometric relationship with its environment), and (4) solar absorptivities (to determine the effect of solar warming). These parameters must be supplied for each material type contained in the scene.

The environmental parameters can be divided into two categories, the location parameters and the meteorological parameters. The location parameters include (1) latitude and longitude, (2) date, time, and time interval for the weather data description, and (3) time of sunrise/sunset. THERM will calculate the sunrise/sunset times from the latitude, longitude, date, and time parameters if necessary. The meteorological parameters include (1) direct and diffuse insolation along with high noon transmission, (2) air temperature (sunrise, peak, and peak time), (3) air pressure, (4) relative humidity, (5) dew point, (6) wind speed, (7) sky exposure (calculated as the percent of sky not obscured by clouds), (8) cloud type (as either cirrus, cirrostratus, altocumulus, altostratus, stratocumulus, stratus, and fog), and (9) precipitation type/rate/temperature. Table 2.2-1 lists the typical input parameters for this model.

THERM can either accept the input of temporal meteorological data or can compute the temporal data using simple environmental models when supplied a limited input. With the first method, the location parameters are input along with a file containing the remaining temporal meteorological data. Figure 2.2-1 shows the temporal nature (diurnal cycle) of various meteorological parameters and the effects that one parameter can have on another. User-input temporal meteorological data is the most accurate method as it provides the model with the maximum amount of information needed to create a weather history and predict temporal object temperatures. However, such data is often unavailable, particularly when one is trying to simulate a future day's imaging scenario. In such cases, THERM will predict the necessary temporal parameters given a limited input of average parameter values. Usually, an average value over the entire day for the parameter in question is selected unless a specific value is requested, such as the maximum temperature for the day. Given the inputs for one point in time, the program computes an estimate of the weather history for the entire day. THERM can then calculate the direct and diffuse insolation from these estimated temporal environmental and location parameters including latitude, season, sun elevation, cloud type, sky cover, air temperature, air pressure and humidity. From these data, THERM can create an estimated weather history and predict temporal object temperatures. This estimated weather history can be further refined by

Table 2.2-1 Input parameters to the DCS THERM model.

<u>Location Parameters</u>	<u>Material Parameters</u>	
Latitude*	Heat Capacity*	
Longitude*	Thermal Conductivity*	
Date*	Thickness*	
Time (Difference from GMT)*	Solar Absorptivities*	
Time Interval*	Exposed Area*	
Time of Sunrise	Self Generated Power*	
Time of Sunset	Slope & Azimuth Angles*	
<u>Meteorological Parameters</u>		
Direct Insolation		
Diffuse Insolation		
High Noon Transmission		
Air Temperature†		
Sunrise Air Temperature*		
Peak Air Temperature*		
Peak Air Temperature Time*		
Air Pressure†		
Relative Humidity†		
Dew Point†		
Wind Speed†		
Sky Exposure†		
Cloud Type†		
Precipitation Type/Rate/Temperature†		

* Required input parameter

† Can be input as a temporal file or as a single value for THERM to compute temporal values which can be edited by the user

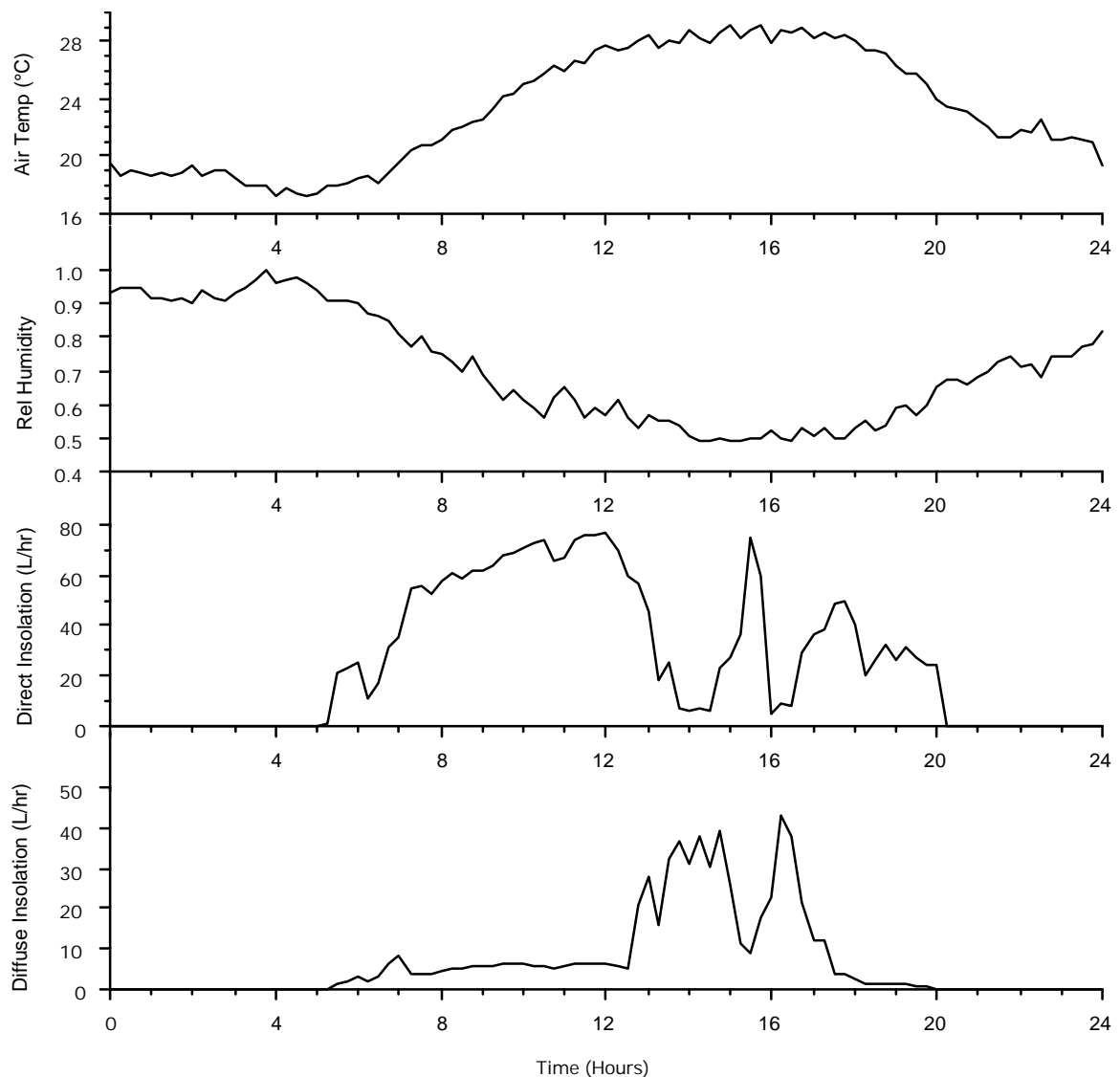


Figure 2.2-1 Typical temporal (diurnal) meteorological data required for input to thermodynamic model.

the user to correspond to a specific scenario's requirements, such as rain, cloud cover, etc., thus allowing the analyst to observe the effects of such variables on the final image.

The weather history for a 24-hour period or longer is initialized using one of the two methods described above. THERM proceeds to compute the temperature of object facets at any point in time based upon the input parameters, either estimated or actual. Since there are no "real" initial object temperatures when THERM starts the process, an approximation is made by setting all object temperatures to the initial equilibrium value. For purposes of accurate temperature prediction, it will be necessary to start the extrapolation process several hours before the desired

time of simulation. This will allow the model to reach a dynamic equilibrium in which the effects of all the parameters in THERM interact to reach a stable contribution to the objects temperature.

As stated earlier, THERM has been shown to produce accurate temporal predictions of temperatures of passive real world objects. Figure 2.2-2 shows an actual object's temperatures compared to THERM predicted values. THERM does not compute the conduction between adjacent facets and therefore does not have all of the functionality of a fully lateral conduction model which would require the use finite element analysis. Such models are complex and require substantial amounts of computing time to add facet-to-facet conduction. THERM does allow for facets with self-generated (internal) power which can, when properly implemented, be used to overcome some of the limitations of non-conduction between facets.

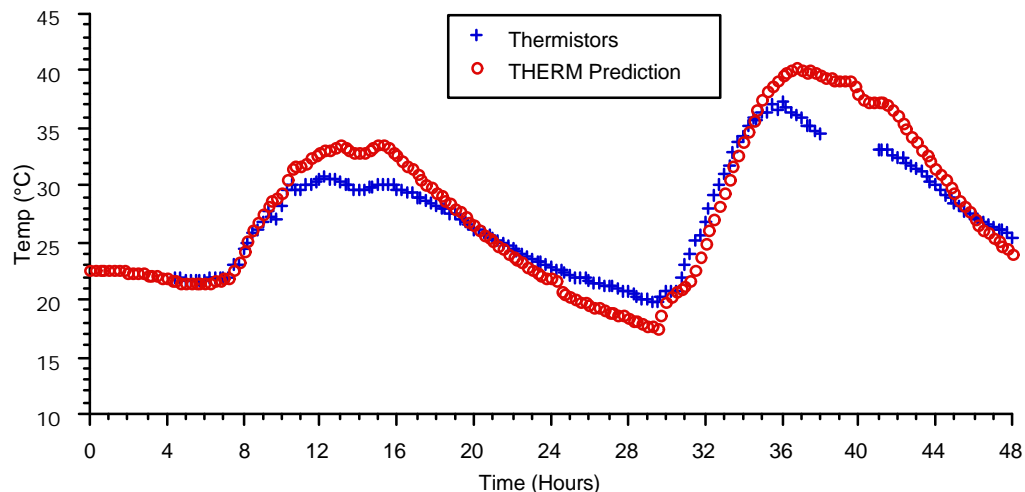


Figure 2.2-2 Actual object temperature versus THERM predicted temperature as a function of time.

2.2.1 Solar insolation

In order to properly model the direct solar insolation term in the thermodynamic model, shadowing of scene elements must be taken into account. For shadows caused by opaque objects such as buildings, vehicles, etc., the direct solar insolation term in the weather history is set to zero for those times in which the current target is in shadow. For those times when the

target is in direct sunlight, the measured or predicted direct insolation term is used without modification. When a translucent object is present in the sun-target path, such as a cloud, the direct solar insolation term is multiplied by the predicted transmittance of the obscuring object. Figure 2.2.1-1 illustrates the concept of modifying the direct solar insolation term for both opaque and transparent objects for several time periods throughout the simulated day. The THERM model as implemented in this effort can accept direct solar insolation on intervals as small as 15 minutes.

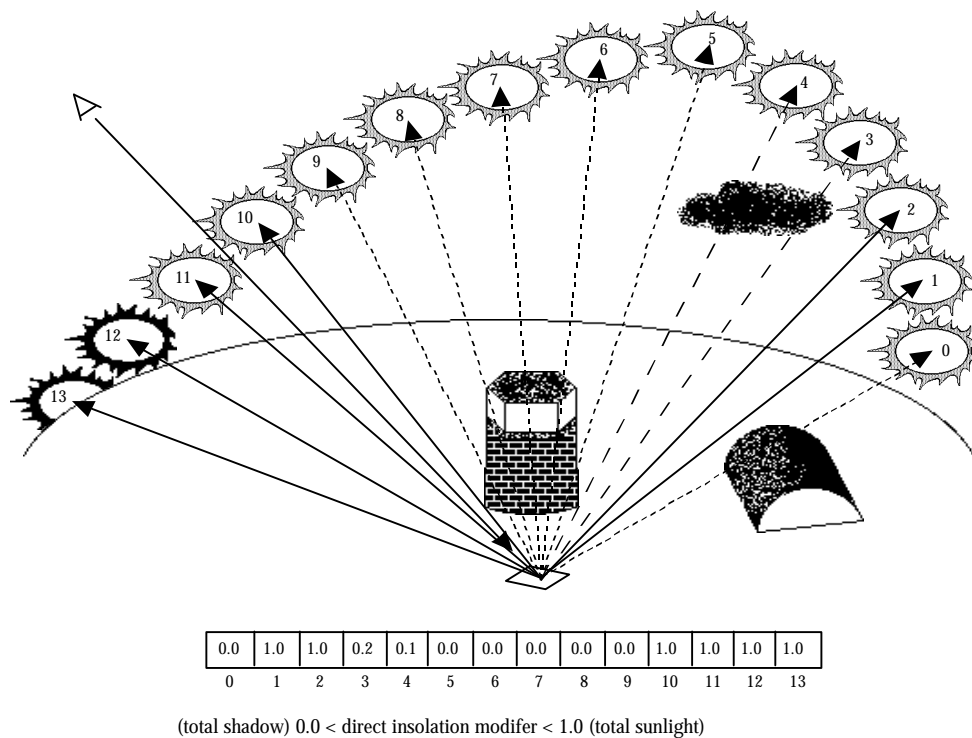


Figure 2.2.1-1 Illustration of the computation of the modifying terms for direct solar insolation as input to the THERM model.

2.3 Ray tracing algorithms

In order to render a three-dimensional scene constructed in a CAD/CAM package such as AutoCAD (Autodesk Inc., 1989) as a two-dimensional image, ray tracing techniques will be employed. It is not the purpose of this research to develop state-of-the-art algorithms for ray tracing, nor will the techniques used be on the cutting edge. Standard algorithms for scene rendering will be employed which are described by Haines, 1987. The ray tracing philosophy

employed will first be described followed by a detailed explanation of the algorithms used.

In order to understand the concepts to follow, some definitions need to be presented describing the geometry of the three-dimensional model which makes up the scene to be simulated. A scene is made up of *objects*. Examples of objects are airplanes, runways, buildings, and trees. The objects are then broken up into *parts*. For instance, the object airplane may be broken into the following parts, left wing, right wing, fuselage, cockpit, radome, and left engine. In turn, each part is broken up into the finest components of the scene, *facets*. Facets are either three- or four-sided polygons which make up elements of the wire frame composing a part. Each facet is described by its vertices which are three-dimensional coordinates in a world-coordinate system.

This breakdown of a scene into objects, parts, and facets gives rise to a very efficient mechanism in ray tracing known as the use of bounding volumes. If one simply looked at a scene as a collection of facets, how would one decide which facet was hit by a ray? You might consider determining the intersection point of the ray with a plane formed by the 3 or 4 vertices making up each facet. Once this intersection point is found, one could determine whether the point falls within the polygonal boundaries formed by the facet vertices. This search would need to be carried out in a linear fashion, investigating every facet in the scene to find which hit facet is closest to the simulated sensor. While complete and sufficient, this approach is very slow and cumbersome. The breakdown of the scene into objects, parts, and facets as described above gives rise to a higher level of efficiency.

Before describing the algorithms used in this effort, one more definition needs to be introduced. If one has an object, a "box" can be constructed which encloses the object. By simply finding the minimum and maximum coordinates for all facets along the x, y, and z axes in the world-coordinate system, a "box" can be made which encloses the object. This box is referred to as a *bounding volume* and can be formed for objects as well as parts in a scene. The advantage of forming these bounding volumes is that facets that make up a particular part (or parts that make up a particular object) are searched if and only if a ray intersects their bounding volume. This technique greatly accelerates the search for the closest intersected facet.

As an example, suppose you have a scene made up of 25 objects, each with 20 parts, each composed of 200 facets (an overly simplified but illustrative example). This results in a scene with 100,000 facets. If carried out in a linear fashion, 100,000 ray-plane intersections would need to be carried out. Using the object, part, facet approach the search for the intersected facet

you would need to determine a maximum of 25 ray-bounding volume intersections for the objects, 20 ray-bounding volume intersections for the parts within an object and 200 ray-plane intersections for the facets making up a part for a total of 245 intersection determinations. This represents approximately a 400:1 increase in efficiency. Figure 2.3-1 depicts a wire-frame object with bounding volumes surrounding each part and Figure 2.3-2 illustrates the tree search layout for finding the intersected facet.

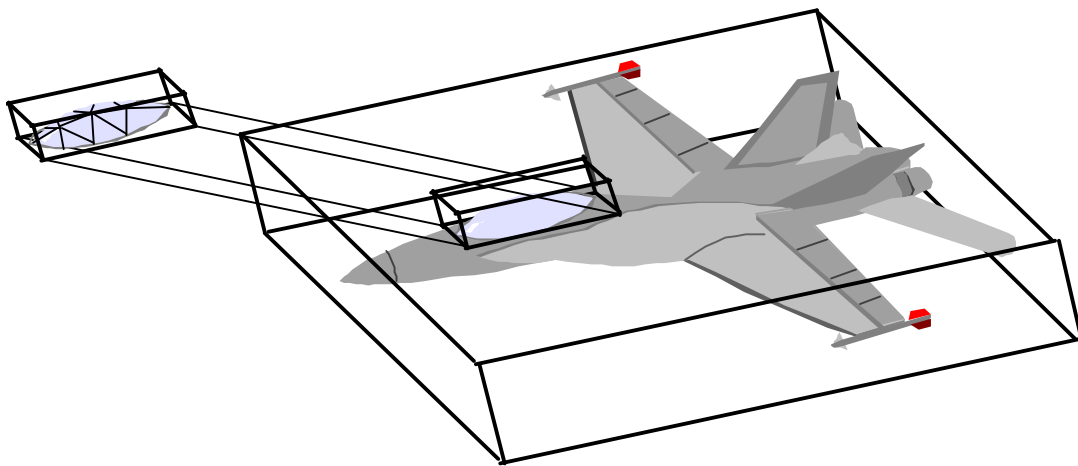


Figure 2.3-1 A single object contained in a bounding volume, with additional bounding volumes around selected parts.

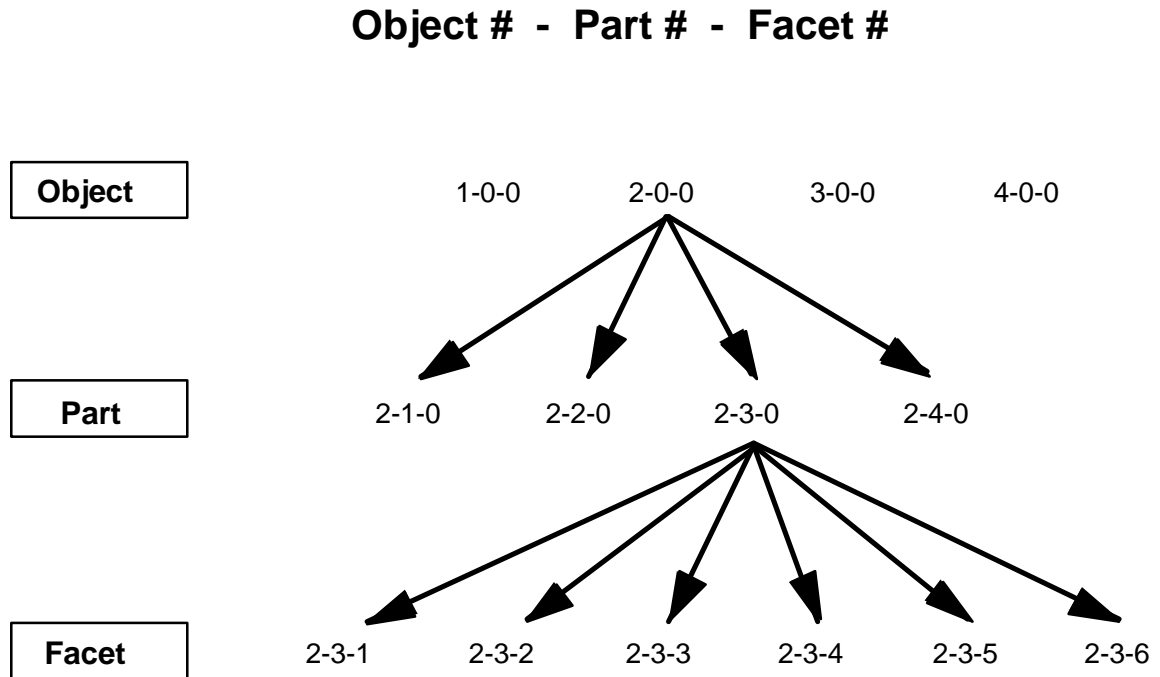


Figure 2.3-2

Tree search used to facilitate the efficiency with which a search is conducted to find the intersected facet. The object and part levels within the tree are delineated by bounding volumes in the ray tracing process.

The following sections will describe in detail the algorithms used for determining the intersection of a ray with a bounding volume, a ray with a plane or facet, and whether or not a ray-plane intersection falls within the vertices making up a facet.

2.3.1 Ray-box intersections

Figure 2.3.1-1 illustrates a ray intersecting a bounding volume or box. For the purposes of ray tracing we need only determine if the box is hit by the ray or not. If the box is hit by the ray, then the bounding volumes or facets within the box need to be searched.

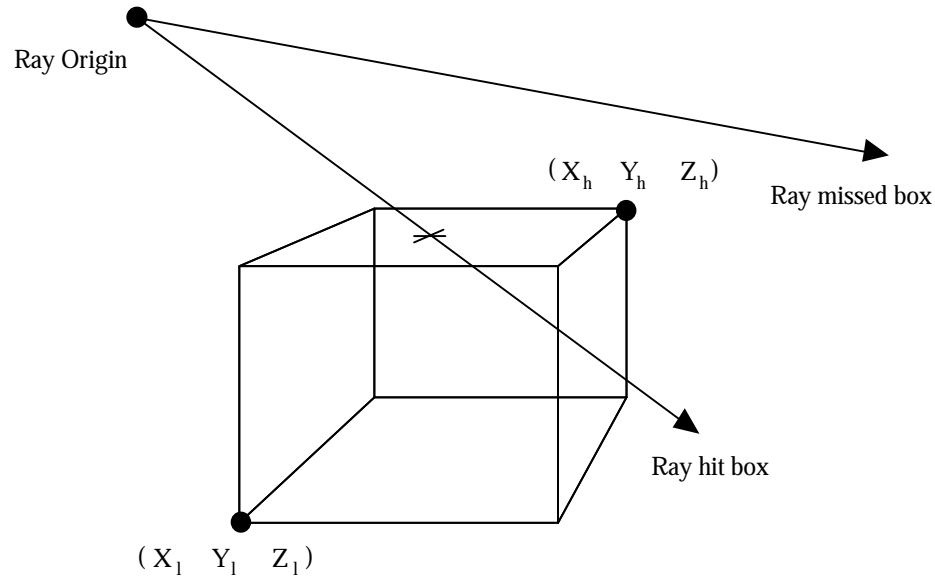


Figure 2.3.1-1 Illustration of ray-box intersection concept with a "hit" and a "miss" shown.

To determine whether a ray has hit a bounding volume we first need some definitions. A ray is defined as having an origin and a direction vector. The ray's origin, R_o , is defined by the coordinate (X_o, Y_o, Z_o) . The ray's direction vector, \mathbf{R}_d , is defined as the normalized vector (X_d, Y_d, Z_d) . A ray of length T , $R(T)$, is then defined as

$$R(T) = R_o + \mathbf{R}_d T \quad 2.3.1-1$$

where $T > 0$. The bounding volume (orthogonal box) as shown in Figure 2.3.1-1 is defined using two extreme coordinates. These are the box's minimum extent, B_l , given as (X_l, Y_l, Z_l) and the box's maximum extent, B_h , given by (X_h, Y_h, Z_h) . The algorithm for determining whether or not a ray hits a bounding volume is as follows (Haines, 1987).

SET $T_{\text{near}} = -$ and $T_{\text{far}} = +$

FOR each pair of planes P associated with X, Y and Z (shown here for the set of X planes):

IF the direction vector component $X_d=0$, the ray is parallel to the planes so:

IF the origin X_o is not between the slabs ($X_o < X_l$ or $X_o > X_h$) then RETURN *MISS*.

ELSE, if the ray is not parallel to the planes

BEGIN:

Calculate intersection distances of planes:

$$T_1 = \frac{X_l - X_o}{X_d}$$

$$T_2 = \frac{X_h - X_o}{X_d}$$

IF $T_1 > T_2$, swap T_1 and T_2 .

IF $T_1 > T_{\text{near}}$, set $T_{\text{near}} = T_1$.

IF $T_2 < T_{\text{far}}$, set $T_{\text{far}} = T_2$.

IF $T_{\text{near}} > T_{\text{far}}$, box is missed so RETURN *MISS*.

IF $T_{\text{far}} < 0$, box is behind ray so RETURN *MISS*.
END.

End of FOR loop.

Since box survived all tests, RETURN *HIT*.

If the box is hit, the intersection distance is equal to T_{near} and the distance to the ray's exit point is T_{far} . Figure 2.3.1-2 illustrates the geometry described by the algorithm above.

2.3.2 Ray-plane intersections

If a ray intersects a bounding volume, each facet within the bounding volume is checked to see whether or not the ray intersects it. This procedure takes two steps, first it is determined whether or not the plane formed by the vertices is intersected by the ray, then the intersection point is checked to see if it falls within the polygon formed by the vertices. To determine whether or not the plane is intersected, the following procedure can be followed.

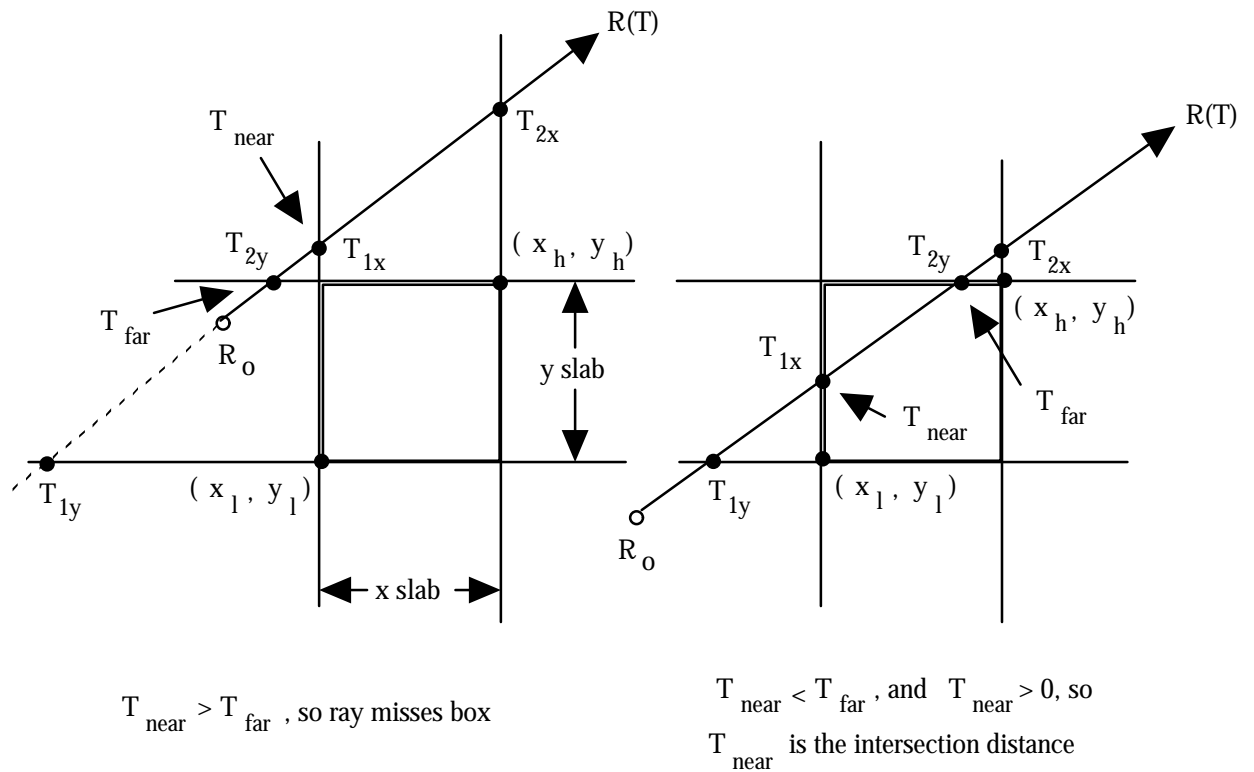


Figure 2.3.1-2

Illustration of the ray/box intersection testing algorithm (Haines, 1987).

One can define a plane in terms of [A,B,C,D] as

$$plane == AX + BY + CZ + D \quad 2.3.2-1$$

where

$$A^2 + B^2 + C^2 = 1 \quad 2.3.2-2$$

and the unit vector normal to the plane is given by

$$\mathbf{P}_n = [A, B, C] \quad 2.3.2-3$$

and the distance from the coordinate system origin [0,0,0] to the plane is simply D, where the sign of D indicates which side of the plane the normal is on (the origin is located). Again we define a ray in terms of its origin and direction vector

$$\begin{aligned} \mathbf{R}_o &= [X_o, Y_o, Z_o] \\ \mathbf{R}_d &= [X_d, Y_d, Z_d] \end{aligned} \quad 2.3.2-4$$

which defines a ray as

$$\mathbf{R}(T) = \mathbf{R}_o + \mathbf{R}_d T \quad 2.3.2-5$$

where $T > 0$. The distance from the ray's origin to the intersection with the plane is obtained by substituting the expansion of Equation 2.3.2-5 into 2.3.2-1 and solving for T as

$$\begin{aligned} A(X_o + X_d T) + B(Y_o + Y_d T) + C(Z_o + Z_d T) + D &= 0 \\ T &= \frac{-(AX_o + BY_o + CZ_o + D)}{(AX_d + BY_d + CZ_d)} = \frac{-(\mathbf{P}_n \bullet \mathbf{R}_o + D)}{(\mathbf{P}_n \bullet \mathbf{R}_d)} \\ T &= \frac{-V_{pro}}{V_{prd}} \end{aligned} \quad 2.3.2-6$$

where V_{prd} is the dot product of the normal with the ray's direction vector and V_{pro} is the dot

product of the normal with the ray's origin, plus the distance from the origin. During the course of computation of these values, if V_{prd} is 0, the ray is parallel to the plane (i.e. the angle between the ray and the normal is 90°) and all testing can be stopped. Also, if $V_{\text{prd}} > 0$, the normal of the plane is pointing away from the ray (i.e. the angle between the ray and normal is less than 90°) and therefore the surface of the plane cannot be seen (for one-sided ray tracing models such as the one used in this work) and testing can be stopped. Figure 2.3.2-1 helps to visualize this concept. If $T < 0$, then the ray intersects the plane behind the ray's origin so no actual intersection occurs. If none of these conditions are true, then the ray does intersect the plane and the intersection point can be computed as

$$R_i = [X_i, Y_i, Z_i] = [X_o + X_d T, X_o + X_d T, X_o + X_d T] \quad 2.3.2-7$$

and the sign of the normal facing the ray can be determined by comparing V_{prd} with zero. If $V_{\text{prd}} > 0$, the sign of the normal needs to be reversed in order for it to point towards the ray. The distance from the ray's origin to the intersection point, L_o , is computed as

$$L_o = T \sqrt{X_d^2 + Y_d^2 + Z_d^2} \quad 2.3.2-8$$

These computations supply all the relevant information for a ray/plane intersection. To finish the ray tracing procedure, one needs to determine if the intersection point falls within the boundary of the polygon formed by the vertices of the facet.

2.3.3 Point-polygon inside-outside testing

To determine whether the intersection point falls within a polygon, the three-dimensional facet and intersection point is projected onto a two-dimensional plane. The number of polygon side/projected axis intersections are counted. If the number of intersections of the polygon sides with the axis is odd, then the intersection point falls within the polygon, if the number of intersections is even, then the point falls outside the facet. This procedure is illustrated in Figure 2.3.3-1 and the algorithm as given by Haines, 1987, follows.

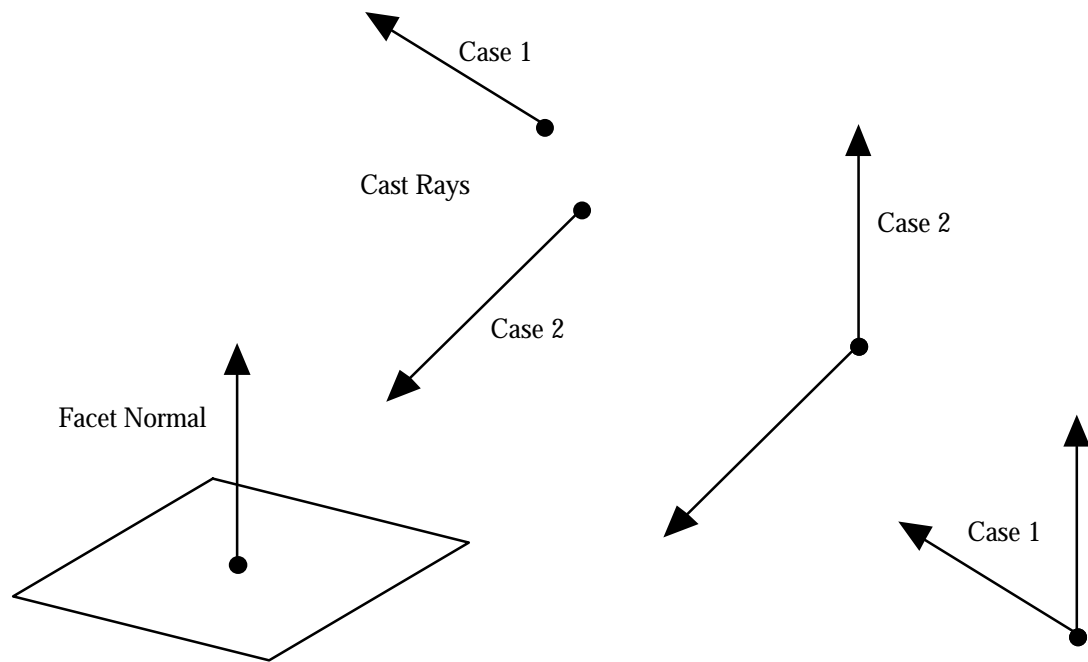


Figure 2.3.2-1

Illustration of plane-ray intersection testing: Case 1 - the ray does not intersect the plane when the angle between the ray and the facet normal is less than 90° ; Case 2 - the ray does intersect the plane when the angle between the ray and the facet normal is greater than 90° .

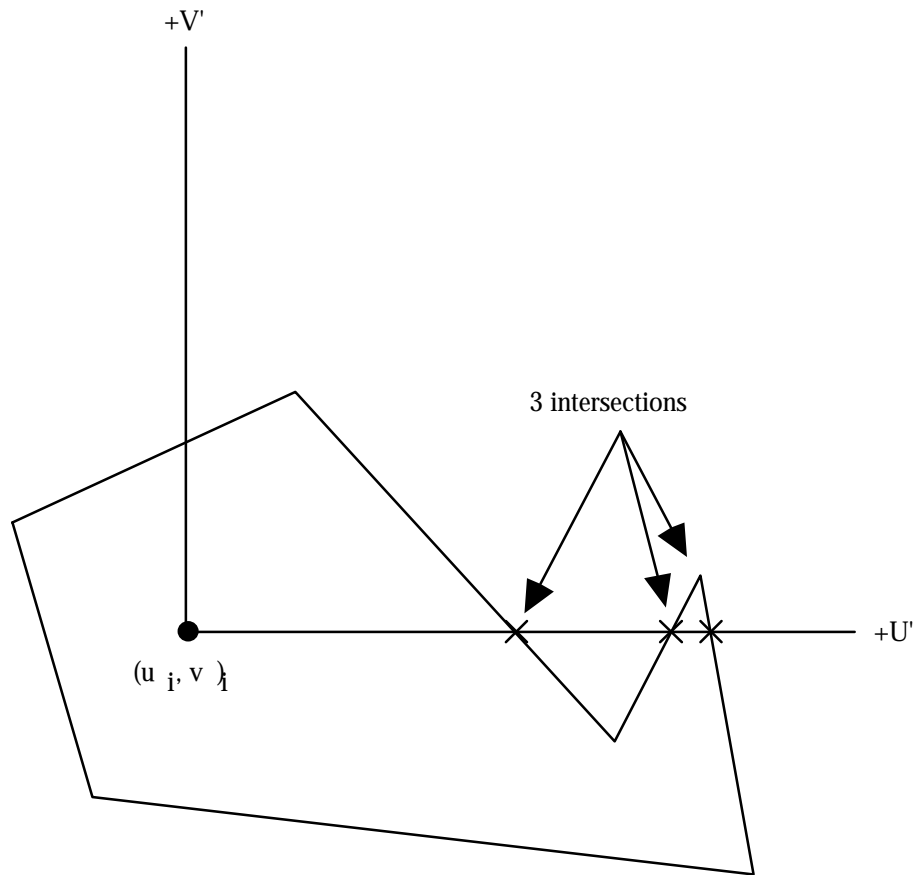


Figure 2.3.3-1

Test for whether or not an intersection point is contained within a polygon. This illustration shows three crossings of the $+U'$ axis indicating that the point is within the polygon (Haines, 1987).

The following is the algorithm used to perform the test to determine whether the intersection point falls within the polygon defined by the facet vertices.

FOR the NV vertices of the polygon, project these onto the dominant coordinate's plane, creating a list of vertices (U_n, V_n):

TRANSLATE the (U, V) polygon so that the intersection point is at the origin, calling these points (U'_n, V'_n).

SET the number of crossings NC to 0.

SET the sign holder SH as a function of V'_0 , the V' value of the first vertex of the first side of the polygon being examined:

SET to -1 if V' is negative.

SET to +1 if V' is zero or positive.

FOR each edge of the polygon formed by the points (U'_a, V'_a) and (U'_b, V'_b) where $a=0$ to $NV-1$, $b=(a+1) \bmod NV$:

SET the next sign holder NSH as a function of V'_b :

SET to -1 if V'_b is negative.

SET to +1 if V'_b is zero or positive.

IF SH is not equal to NSH:

IF U'_a and U'_b are both positive then the side must cross $+U'$, so $NC=NC+1$.

ELSE IF either U'_a or U'_b is positive then the line might cross, so compute the intersection with the U' axis:

$$\text{IF } U'_a - V'_a \frac{U'_b - U'_a}{V'_b - V'_a} \text{ is positive then the line}$$

must cross the $+U'$ axis, so $NC=NC+1$.

SET SH equal to NSH.

NEXT edge.

IF NC is odd, THEN the intersection point is with the polygon.

2.4 Radiance field reaching the sensor

Once the geometric characteristics for each facet comprising the scene have been described by the scene geometry and ray tracer submodels and the temperature for these facets determined by the thermal submodel, radiance leaving these facets and arriving at the front end of the sensor needs to be determined. In order to accomplish this determination, a modeled characterization of the intervening atmosphere needs to be established which includes the following: transmission between each element in the scene and both the sensor and source, the upwelling path radiance in the sensor-target path, and the downwelled sky radiance from each point on a hemisphere above the scene. The exoatmospheric source radiance as well as the facet emitted radiance also need to be determined.

The Air Force Geophysics Laboratory (AFGL)/Spectral Sciences Incorporated MODTRAN Atmospheric Transmission/Radiance Code (Berk *et al.*, 1989; Kneizys *et al.*, 1988) was chosen as the model to be used for this purpose because of its wide acceptance and availability throughout the remote sensing community and its increased spectral resolution over the LOWTRAN 7 model (to a frequency of 2 cm^{-1}). MODTRAN models the atmosphere as many individual layers, each of which exhibits either pre-defined or user-specified meteorological conditions, atmospheric composition of gases, aerosol type and specific scattering phase functions, as well as sensitivity to global position. This model can be executed to produce exoatmospheric solar irradiance, transmission from space to the target, transmission from the target to the sensing platform, path radiance from atmospheric self-emission as well as scattered sunlight and target self-emission. MODTRAN is a multiple scattering model which exhibits many of the real-world scattering phenomena that occurs in actual radiance propagation. Many modifications have been implemented to this model and a subsequent superset model formed called the Spectral Vector Generating Model (SVGM) (Salvaggio *et al.*, 1991). This model separates out the individual factors contributing to the radiance field as defined by MODTRAN. Spectral representations of exoatmospheric solar irradiance, transmission, and path radiance are extracted from the MODTRAN code. In addition, the SVGM produces values for solar and emitted downwelling sky radiance. The radiometry submodel fully encompasses the SVGM and places it in combination with a numerical integration routine to produce integrated radiance values over a user-specified bandpass.

The SVGM portion of the radiometry submodel is currently run prior to the execution of the ray tracer submodel. The output is a radiance data structure completely describing the radiance field within the angular field-of-view of the sensor, accounting for all path differences and angular changes presented across the target field. This data structure is specific to a particular time-of-day and day-of-year. A separate data structure is created for each point in time. Appendix A contains a description of this data structure.

The interaction of the ray tracing routines with the simulated scene give rise to four different scenarios. The scenarios will be referred to using the following ray interaction types: the ray will encounter a diffuse object, the ray will encounter a specular object and bounce to a background, the ray will encounter a specular object and bounce to the sky, or the ray will miss all scene elements. These ray interaction types are shown in Figure 2.4-1.

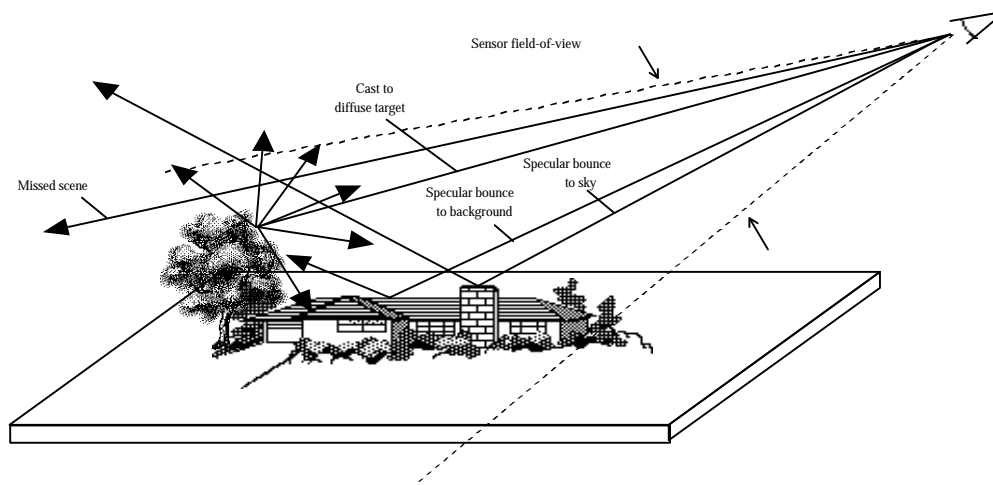


Figure 2.4-1 Ray interaction types allowed for by the DIRSIG model.

The spectral radiance reaching a sensor from a target with specular reflectance characteristics is described by

$$\begin{aligned}
 L(\mathbf{q}, \mathbf{f}, \mathbf{l}) = & \left\{ \mathbf{e}_T(\mathbf{q}, \mathbf{l}) L_T(\mathbf{l}) + \right. \\
 & \left[\frac{E_S(\mathbf{l})}{p} \mathbf{t}_1(\mathbf{l}) \mathbf{t}_{1c}(\mathbf{l}) \cos(\mathbf{q}_S) + \right. \\
 & \left(F[L_{DE}(\mathbf{q}_{SK}, \mathbf{f}_{SK}, \mathbf{l}) + L_{DS}(\mathbf{q}_{SK}, \mathbf{f}_{SK}, \mathbf{l})] + \right. \\
 & (1 - F)\{\mathbf{e}_B(\mathbf{q}_{BT}, \mathbf{l}) L_{TB}(\mathbf{l}) + \\
 & \frac{E_S(\mathbf{l})}{p} \mathbf{t}_1(\mathbf{l}) \mathbf{t}_{SB}(\mathbf{l}) \cos(\mathbf{q}_B)[1 - \mathbf{e}_B(\mathbf{q}_{BT}, \mathbf{l})] \mathbf{t}_{TB}(\mathbf{l}) + \\
 & \left. [1 - \mathbf{t}_{TB}(\mathbf{l})] L_{T(TBE)}(\mathbf{l}) \} \right] \\
 & \left. (1 - \mathbf{e}_T(\mathbf{q}, \mathbf{l})) \right\} \\
 & \mathbf{t}_2(\mathbf{q}_E, p, \mathbf{l}) \mathbf{t}_{2c}(\mathbf{l}) + \\
 & L_{uE}(\mathbf{q}_E, p, \mathbf{l}) + L_{uS}(\mathbf{q}_E, p, \mathbf{l}) + [1 - \mathbf{t}_{2c}(\mathbf{l})] L_{T(STE)}(\mathbf{l})
 \end{aligned} \tag{2.4-1}$$

where the shape factor F is set to unity for a secondary specular bounce to the sky or to zero for a bounce to a background object. The spectral reflectance for a target exhibiting diffuse reflectance characteristics is given by

$$\begin{aligned}
 L(\mathbf{q}, \mathbf{f}, \mathbf{l}) = & \left\{ \mathbf{e}_T(0, \mathbf{l}) L_T(\mathbf{l}) + \right. \\
 & \left[\frac{E_S(\mathbf{l})}{p} \mathbf{t}_1(\mathbf{l}) \mathbf{t}_{1c}(\mathbf{l}) \cos(\mathbf{q}_S) + \right. \\
 & \left(F[L_{DE}(\mathbf{l}) + L_{DS}(\mathbf{l})] + \right. \\
 & (1 - F)\{\mathbf{e}_B(\mathbf{q}_{BT}, \mathbf{l}) L_{TB}(\mathbf{l}) + \\
 & \frac{E_S(\mathbf{l})}{p} \mathbf{t}_1(\mathbf{l}) \mathbf{t}_{SB}(\mathbf{l}) \cos(\mathbf{q}_B)[1 - \mathbf{e}_B(\mathbf{q}_{BT}, \mathbf{l})] \} \right] \\
 & \left. [1 - \mathbf{e}_T(0, \mathbf{l})] \right\} \\
 & \mathbf{t}_2(\mathbf{q}_E, p, \mathbf{l}) \mathbf{t}_{2c}(\mathbf{l}) + \\
 & L_{uE}(\mathbf{q}_E, p, \mathbf{l}) + L_{uS}(\mathbf{q}_E, p, \mathbf{l}) + [1 - \mathbf{t}_{2c}(\mathbf{l})] L_{T(STE)}(\mathbf{l})
 \end{aligned} \tag{2.4-2}$$

where the background emitted radiance, $L_{TB}(\lambda)$, is the radiance due to a blackbody at a temperature, T_B , equal to the average temperature of all possible background objects which the target is exposed to while the emissivity, $\varepsilon_B(\theta_{BT}, \lambda)$, is the angular spectral emissivity of the most common background to which the target is exposed. This method is carried out as an approximation of the numerical integration of the radiance emitted by all background objects which are visible from the target.

The final integrated radiance field is computed as the integral of the above spectral radiance values,

$$L(\mathbf{q}, \mathbf{f}) = \int_l L(\mathbf{q}, \mathbf{f}, l) b(l) dl \quad 2.4-3$$

The variables used in Equations 2.4-1 through 2.4-3 are defined as follows:

$L(\theta, \phi, \lambda)$	spectral radiance reaching the front end of the sensor
$E_s(\lambda)$	the exoatmospheric solar spectral irradiance
$L_T(\lambda)$	the emitted spectral radiance from a blackbody at temperature T (target)
$L_{TB}(\lambda)$	the emitted spectral radiance from a blackbody at temperature T (background)
$L_{T(TBE)}(\lambda)$	the emitted spectral radiance from a blackbody at temperature T (extinction source between the target and the background)
$L_{T(STE)}(\lambda)$	the emitted spectral radiance from a blackbody at temperature T (extinction source between the sensor and the target)
$L_{DE}(\lambda)$	the downwelled spectral radiance due to self-emission of the atmosphere integrated over the skydome
$L_{DS}(\lambda)$	the downwelled spectral radiance due to scattering integrated over the skydome
$L_{DE}(\theta_{SK}, \phi_{SK}, \lambda)$	the directional downwelled spectral radiance due to self-emission of the atmosphere
$L_{DS}(\theta_{SK}, \phi_{SK}, \lambda)$	the directional downwelled spectral radiance due to scattering
$L_{UE}(\theta_E, \lambda)$	the upwelled spectral radiance due to self-emission of the atmosphere along the target-sensor path

$L_{uS}(\theta_E, \lambda)$	the upwelled spectral radiance due to scattering along the target-sensor path
$\tau_1(\lambda)$	the atmospheric spectral transmission along the source-target path
$\tau_2(\theta_E, \lambda)$	the atmospheric spectral transmission along the target -sensor path
$\tau_{1c}(\lambda)$	the spectral transmission through all transparent objects encountered along the sun-target path
$\tau_{SB}(\lambda)$	the spectral transmission through all transparent objects encountered along the sun-background path
$\tau_{TB}(\lambda)$	the spectral transmission through all transparent objects encountered along the target-background path
$\tau_{2c}(\lambda)$	the spectral transmission through all transparent objects encountered along the sensor-target path
$\varepsilon_T(\theta, \lambda)$	angular spectral emissivity for the target
$\varepsilon_B(\theta, \lambda)$	angular spectral emissivity for the background
θ	the angle between the normal to the surface and the sensor-target path
θ_S	the angle between the normal to the surface and the sun-target path
θ_B	the angle between the normal to the background and the sun-background path
θ_E	the angle between normal to the earth at the target and the sensor-target path
θ_{SK}	the angle between the normal to the earth and the specularly reflected ray from the sensor to target cast
θ_{BT}	the angle between the normal to the background and the target hit point
ϕ	the azimuth angle between the projection of the sensor-target path on the ground and the scene's reference direction
ϕ_{SK}	the azimuth angle between the projection of the ray cast to the sky on the ground and the scene's reference direction
F	shape factor, the fraction of exposed skydome
p	the range between the target and the sensor
$\beta(\lambda)$	the spectral response of the sensor

The angles between the radiometric contributors in the scene are illustrated in Figure 2.4-2.

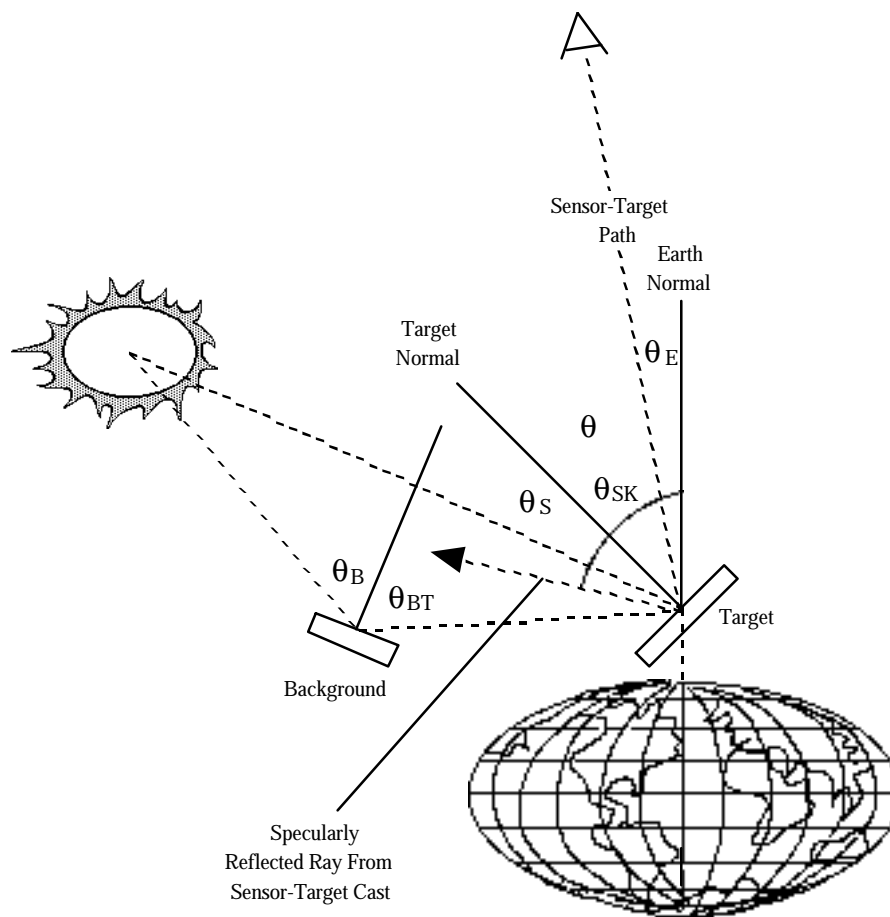


Figure 2.4-2 Relevant angles needed to simulate the radiometric interactions which are simulated by the DIRSIG model.

Many of the terms in the Equations 2.4-1 and 2.4-2 are arrived at by repeated runs of SVGSM atmospheric propagation code. A single run of the code is made to obtain the exoatmospheric solar irradiance and the transmission term along the sun/target path. The code is then run to simulate a series of different look angles with the sensor at a fixed altitude. For each look angle, the atmospheric transmission, solar scattered and emitted path radiance are recorded along with the range to the target (in this case the ground). Finally, a series of runs are made with the sensor located at the nominal target point (scene center) pointing up to the sky with a slant path to space at a series of azimuth and zenith angles. This series fills the downwelled sky radiance database to be described later. All of this data is stored in a radiance database having the form shown in Figure 2.4-3. Table 2.4-1 describes the origin of all the terms used in these radiance equations.

h	sensor altitude (km)
λ_{\min}	minimum wavelength (microns)
λ_{\max}	maximum wavelength (microns)
ν_{\min}	minimum frequency (1/cm)
ν_{\max}	maximum frequency (1/cm)
$d\nu$	frequency increment (1/cm)
n	number of spectral points
θ_{\min}	minimum zenith angle (degrees)
θ_{\max}	maximum zenith angle (degrees)
$d\theta$	zenith increment (degrees)
$\theta_{\text{meaningful}}$	maximum meaningful zenith angle (degrees)
m	number of zenith angles

λ_1	ν_1	$E_s(\lambda_1)$	$\tau_1(\lambda_1)$	solar radiance ($\text{W}/\text{cm}^2 \text{ sr}$)
λ_2	ν_2	$E_s(\lambda_2)$	$\tau_1(\lambda_2)$	
λ_3	ν_3	$E_s(\lambda_3)$	$\tau_1(\lambda_3)$	
...				
λ_n	ν_n	$E_s(\lambda_n)$	$\tau_1(\lambda_n)$	

θ_1	p_1			path radiance and transmission ($\text{W}/\text{cm}^2 \text{ sr}$)
$\tau_2(\lambda_1, \theta_1, p_1)$		$L_{uE}(\lambda_1, \theta_1, p_1)$	$L_{uS}(\lambda_1, \theta_1, p_1)$	
$\tau_2(\lambda_2, \theta_1, p_1)$		$L_{uE}(\lambda_2, \theta_1, p_1)$	$L_{uS}(\lambda_2, \theta_1, p_1)$	
$\tau_2(\lambda_3, \theta_1, p_1)$		$L_{uE}(\lambda_3, \theta_1, p_1)$	$L_{uS}(\lambda_3, \theta_1, p_1)$	
...				
$\tau_2(\lambda_n, \theta_1, p_1)$		$L_{uE}(\lambda_n, \theta_1, p_1)$	$L_{uS}(\lambda_n, \theta_1, p_1)$	
θ_2	p_2			
$\tau_2(\lambda_1, \theta_2, p_2)$		$L_{uE}(\lambda_1, \theta_2, p_2)$	$L_{uS}(\lambda_1, \theta_2, p_2)$	
$\tau_2(\lambda_2, \theta_2, p_2)$		$L_{uE}(\lambda_2, \theta_2, p_2)$	$L_{uS}(\lambda_2, \theta_2, p_2)$	
$\tau_2(\lambda_3, \theta_2, p_2)$		$L_{uE}(\lambda_3, \theta_2, p_2)$	$L_{uS}(\lambda_3, \theta_2, p_2)$	
...				
$\tau_2(\lambda_n, \theta_2, p_2)$		$L_{uE}(\lambda_n, \theta_2, p_2)$	$L_{uS}(\lambda_n, \theta_2, p_2)$	
.				
.				
.				
θ_m	p_m			
$\tau_2(\lambda_1, \theta_m, p_m)$		$L_{uE}(\lambda_1, \theta_m, p_m)$	$L_{uS}(\lambda_1, \theta_m, p_m)$	
$\tau_2(\lambda_2, \theta_m, p_m)$		$L_{uE}(\lambda_2, \theta_m, p_m)$	$L_{uS}(\lambda_2, \theta_m, p_m)$	
$\tau_2(\lambda_3, \theta_m, p_m)$		$L_{uE}(\lambda_3, \theta_m, p_m)$	$L_{uS}(\lambda_3, \theta_m, p_m)$	
...				
$\tau_2(\lambda_n, \theta_m, p_m)$		$L_{uE}(\lambda_n, \theta_m, p_m)$	$L_{uS}(\lambda_n, \theta_m, p_m)$	

$L_{DE}(\lambda_1)$	$L_{DS}(\lambda_1)$	integrated hemispheric sky radiance ($\text{W}/\text{cm}^2 \text{ sr}$)
$L_{DE}(\lambda_2)$	$L_{DS}(\lambda_2)$	
$L_{DE}(\lambda_3)$	$L_{DS}(\lambda_3)$	
...		
$L_{DE}(\lambda_n)$	$L_{DS}(\lambda_n)$	

θ_{SK1}	ϕ_{SK1}	directional sky radiance ($W/cm^2 \text{ sr}$) ($\theta_{SK} \rightarrow 0^\circ$ to 90° by 15°) ($\phi_{SK} \rightarrow 0^\circ$ to 360° by 30°)
$LDE(\lambda_1, \theta_{SK1}, \phi_{SK1})$	$LDS(\lambda_1, \theta_{SK1}, \phi_{SK1})$	
$LDE(\lambda_2, \theta_{SK1}, \phi_{SK1})$	$LDS(\lambda_2, \theta_{SK1}, \phi_{SK1})$	
$LDE(\lambda_3, \theta_{SK1}, \phi_{SK1})$	$LDS(\lambda_3, \theta_{SK1}, \phi_{SK1})$	
...		
$LDE(\lambda_n, \theta_{SK1}, \phi_{SK1})$	$LDS(\lambda_n, \theta_{SK1}, \phi_{SK1})$	
θ_{SK1}	ϕ_{SK2}	
$LDE(\lambda_1, \theta_{SK1}, \phi_{SK2})$	$LDS(\lambda_1, \theta_{SK1}, \phi_{SK2})$	
$LDE(\lambda_2, \theta_{SK1}, \phi_{SK2})$	$LDS(\lambda_2, \theta_{SK1}, \phi_{SK2})$	
$LDE(\lambda_3, \theta_{SK1}, \phi_{SK2})$	$LDS(\lambda_3, \theta_{SK1}, \phi_{SK2})$	
...		
$LDE(\lambda_n, \theta_{SK1}, \phi_{SK2})$	$LDS(\lambda_n, \theta_{SK1}, \phi_{SK2})$	
.		
.		
.		
θ_{SK1}	ϕ_{SKS}	
$LDE(\lambda_1, \theta_{SK1}, \phi_{SKS})$	$LDS(\lambda_1, \theta_{SK1}, \phi_{SKS})$	
$LDE(\lambda_2, \theta_{SK1}, \phi_{SKS})$	$LDS(\lambda_2, \theta_{SK1}, \phi_{SKS})$	
$LDE(\lambda_3, \theta_{SK1}, \phi_{SKS})$	$LDS(\lambda_3, \theta_{SK1}, \phi_{SKS})$	
...		
$LDE(\lambda_n, \theta_{SK1}, \phi_{SKS})$	$LDS(\lambda_n, \theta_{SK1}, \phi_{SKS})$	
.		
.		
.		
.		
θ_{SKR}	ϕ_{SK1}	
$LDE(\lambda_1, \theta_{SKR}, \phi_{SK1})$	$LDS(\lambda_1, \theta_{SKR}, \phi_{SK1})$	
$LDE(\lambda_2, \theta_{SKR}, \phi_{SK1})$	$LDS(\lambda_2, \theta_{SKR}, \phi_{SK1})$	
$LDE(\lambda_3, \theta_{SKR}, \phi_{SK1})$	$LDS(\lambda_3, \theta_{SKR}, \phi_{SK1})$	
...		
$LDE(\lambda_n, \theta_{SKR}, \phi_{SK1})$	$LDS(\lambda_n, \theta_{SKR}, \phi_{SK1})$	
θ_{SKR}	ϕ_{SK2}	
$LDE(\lambda_1, \theta_{SKR}, \phi_{SK2})$	$LDS(\lambda_1, \theta_{SKR}, \phi_{SK2})$	
$LDE(\lambda_2, \theta_{SKR}, \phi_{SK2})$	$LDS(\lambda_2, \theta_{SKR}, \phi_{SK2})$	
$LDE(\lambda_3, \theta_{SKR}, \phi_{SK2})$	$LDS(\lambda_3, \theta_{SKR}, \phi_{SK2})$	
...		
$LDE(\lambda_n, \theta_{SKR}, \phi_{SK2})$	$LDS(\lambda_n, \theta_{SKR}, \phi_{SK2})$	
.		
.		
.		
θ_{SKR}	ϕ_{SKS}	
$LDE(\lambda_1, \theta_{SKR}, \phi_{SKS})$	$LDS(\lambda_1, \theta_{SKR}, \phi_{SKS})$	
$LDE(\lambda_2, \theta_{SKR}, \phi_{SKS})$	$LDS(\lambda_2, \theta_{SKR}, \phi_{SKS})$	
$LDE(\lambda_3, \theta_{SKR}, \phi_{SKS})$	$LDS(\lambda_3, \theta_{SKR}, \phi_{SKS})$	
...		
$LDE(\lambda_n, \theta_{SKR}, \phi_{SKS})$	$LDS(\lambda_n, \theta_{SKR}, \phi_{SKS})$	

Figure 2.4-3

Radiance database structure used for computation of the radiance field reaching the sensor.

Table 2.4-1 Origin of individual parameters used in the radiometric equations.

Radiometric Parameter	Parameter Origin
$L(\theta, \phi, \lambda)$	desired radiance vector
$L_T(\lambda)$	temperature from THERM, radiance from Planck's equation
$L_{TB}(\lambda)$	temperature from THERM, radiance from Planck's equation
$L_{T(TBE)}(\lambda)$	temperature from THERM or atmospheric profile, radiance from Planck's equation
$L_{T(STE)}(\lambda)$	temperature from THERM or atmospheric profile, radiance from Planck's equation
$E_S(\lambda)$	LOWTRAN 7 (table look-up)
$L_{DE}(\lambda)$	SVGM (table look-up)
$L_{DS}(\lambda)$	SVGM (table look-up)
$L_{DE}(\theta_{SK}, \phi_{SK}, \lambda)$	SVGM (interpolated on θ_{SK})
$L_{DS}(\theta_{SK}, \phi_{SK}, \lambda)$	SVGM (interpolated on θ_{SK})
$L_{uE}(\theta_E, \lambda)$	LOWTRAN 7 (interpolated on θ_E)
$L_{uS}(\theta_E, \lambda)$	LOWTRAN 7 (interpolated on θ_E)
$\tau_1(\lambda)$	LOWTRAN 7 (table look-up)
$\tau_2(\theta_E, \lambda)$	LOWTRAN 7 (interpolated on θ_E)
$\tau_{1c}(\lambda)$	computed from spectral extinction coefficient and path length through object
$\tau_{TB}(\lambda)$	computed from spectral extinction coefficient and path length through object
$\tau_{SB}(\lambda)$	computed from spectral extinction coefficient and path length through object
$\tau_{2c}(\lambda)$	computed from spectral extinction coefficient and path length through object
$\varepsilon_T(\theta, \lambda)$	DIRS data base (table look-up to nearest degree)
$\varepsilon_B(\theta, \lambda)$	DIRS data base (table look-up to nearest degree)
$\theta, \theta_{BT}, \theta_S, \theta_B,$ $\theta_E, \theta_{SK}, \theta_{BT}, \phi$	ray tracer
F	ray tracer
ρ	ray tracer

In the computation of the target temperature using the THERM thermodynamic model, the radiometry model needs to determine the direct solar loading which is present on the target. This loading is part of the weather data used for the modeling scenario in the direct insolation term. This term is modified by a transmission determined in the following manner. Since THERM wants the direct solar insolation as a broad-band value (covering the entire electromagnetic spectrum), the radiometric model uses an extinction value for the bandpass from 0.4 to 2.5 μm to determine the transmission of any objects present in the sun-target path at the time of simulation. For opaque objects, the target is considered to have no direct solar loading while the solar loading is attenuated by the appropriate transmission for transmissive objects such as clouds. The transmission value, τ_{1c} , is computed simply as

$$t_{1c} = e^{-\beta z} \quad 2.4-4$$

where β is the broad-band (0.4 to 2.5 μm) extinction coefficient and z is the total path length through the attenuating object.

The temperature values returned from the THERM model are used to compute the terms L_T and L_{TB} in Equations 2.4-1 and 2.4-2 using the radiant energy from a blackbody radiator defined by

$$L_T(I) = \frac{2phc^2}{I^5 \left(e^{\frac{hc}{IkT}} - 1 \right)} \quad 2.4-5$$

where T is the absolute kinetic temperature ($^{\circ}\text{K}$) of the target (or background), c is the speed of light, $2.997924580 \times 10^{10}$ (cm sec^{-1}), h is Planck's constant, 6.626176×10^{-34} (J sec^{-1}), and k is the Boltzmann constant, 1.380662×10^{-23} ($\text{J } ^{\circ}\text{K}^{-1}$).

2.4.1 Downwelled sky radiance

The downwelling sky radiance is treated in a unique manner depending on the optical nature of the primary material encountered. For a specular target, directional downwelled radiance is determined for the particular portion of the sky which is in the reflected direction. For a diffuse target, an integrated hemispheric downwelled radiance value is computed. For either case, a database of sky radiance values is accessed which consists of spectral radiance as a function of

zenith and azimuth angle, $L(\theta, \phi, \lambda)$. The database is defined on 15° increments in zenith from 0° (straight above) to 90° (horizon) and on 30° increments in azimuth from 0° (north-facing) to 360° . This database is illustrated in Figure 2.4.1-1.

		Sky Zenith Angle						
λ_n		0	15	30	45	60	75	90
0								
30								
60								
λ_3		0	15	30	45	60	75	90
0								
30								
60								
λ_2		0	15	30	45	60	75	90
0								
30								
60								
λ_1		0	15	30	45	60	75	90
Sky Azimuth Angle	0	0.002723	0.002689	0.002701	0.002849	0.003268	0.004185	0.005305
	30	0.002723	0.003079	0.003435	0.003767	0.004212	0.005062	0.005883
	60	0.002723	0.003545	0.004829	0.006155	0.006926	0.007497	0.007384
	90	0.002723	0.003835	0.006239	0.014249	0.013605	0.011246	0.009157
	120	0.002723	0.003702	0.005494	0.008595	0.009219	0.009050	0.008192
	150	0.002723	0.003288	0.004028	0.004769	0.005344	0.006076	0.006510
	180	0.002723	0.002863	0.003028	0.003258	0.003689	0.004576	0.0055610
	210	0.002723	0.002558	0.002519	0.002663	0.003102	0.004046	0.005242
	240	0.002723	0.002377	0.002284	0.002437	0.002912	0.003908	0.005222
	270	0.002723	0.002296	0.002193	0.002362	0.002865	0.003894	0.005277
	300	0.002723	0.002296	0.002193	0.002361	0.002864	0.003893	0.005275
	330	0.002723	0.002377	0.002283	0.002435	0.002910	0.003906	0.005221
	360	0.002723	0.002558	0.002518	0.002662	0.003101	0.004047	0.005244

Figure 2.4.1-1

Downwelled sky radiance database formed from repeated runs of the MODTRAN atmospheric transmission and path radiance code. The model is run in the vertical or slant path to space mode.

The sky radiance simulated with the use of the SVGSM model is depicted in Figures 2.4.1-2 and 2.4.1-3 for the longwave infrared and visible portions of the spectrum. The completely isotropic nature of this downwelling radiance field in the longwave portion of the spectrum is dramatically contrasted against the highly varying field in the visible portion of the spectrum.

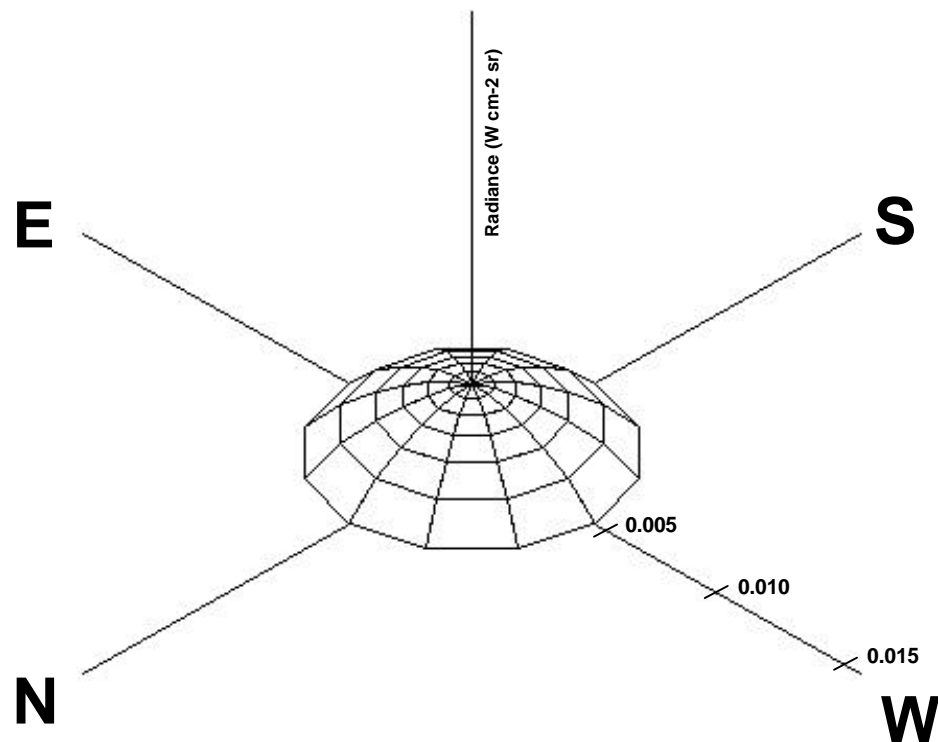


Figure 2.4.1-2

Spherical plot illustrating the downwelled sky radiance field in the 8 to 14 micron bandpass (longwave infrared portion of the spectrum, 750 to 1250 cm^{-1}). Simulated radiance produced for the following conditions: $39^{\circ}46'24''\text{N}$ latitude, $84^{\circ}06'32''\text{W}$ longitude, day number 172, 9:00AM local time (14:00 GMT).

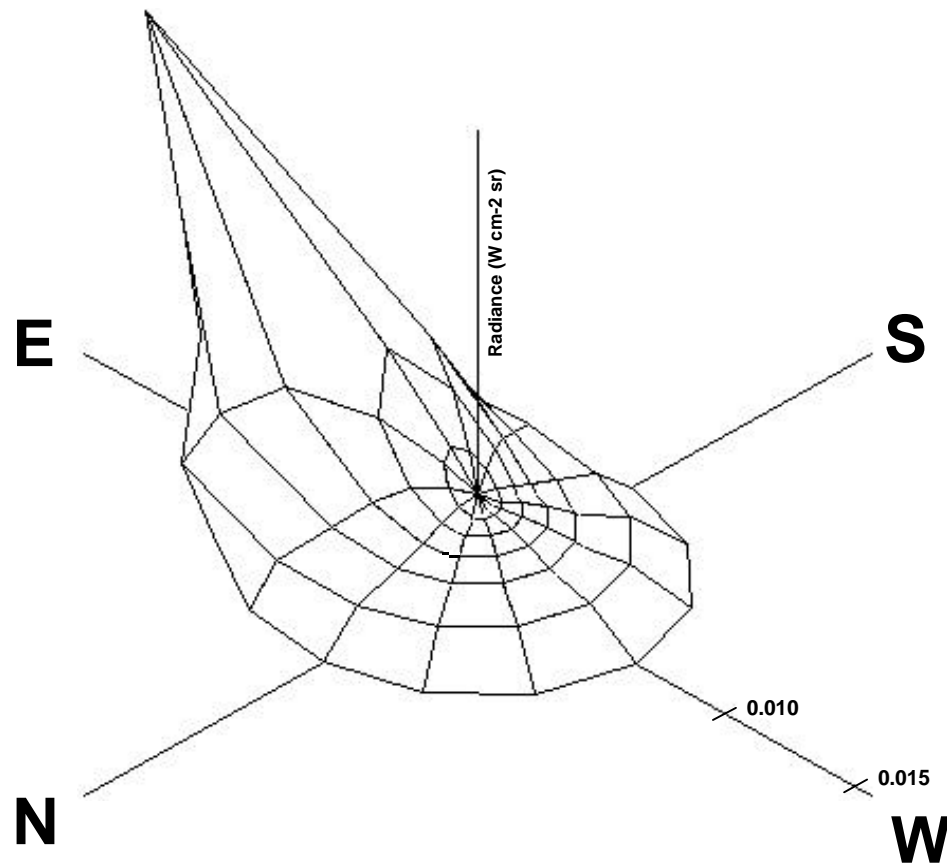


Figure 2.4.1-3

Spherical plot illustrating the downwelled sky radiance field in the 0.4 to 0.7 micron bandpass (visible portion of the spectrum, 14200 to 25000 cm^{-1}). Simulated radiance produced for the following conditions: 39°46'24"N latitude, 84°06'32"W longitude, day number 172, 9:00AM local time (14:00 GMT).

For specular targets, a simple bilinear interpolation method is used to determine the downwelled sky radiance at the particular azimuth (ϕ) and zenith (θ) angle. The interpolation is depicted in Figure 2.4.1-4 and described in Equations 2.4.1-1 through 2.4.1-3.

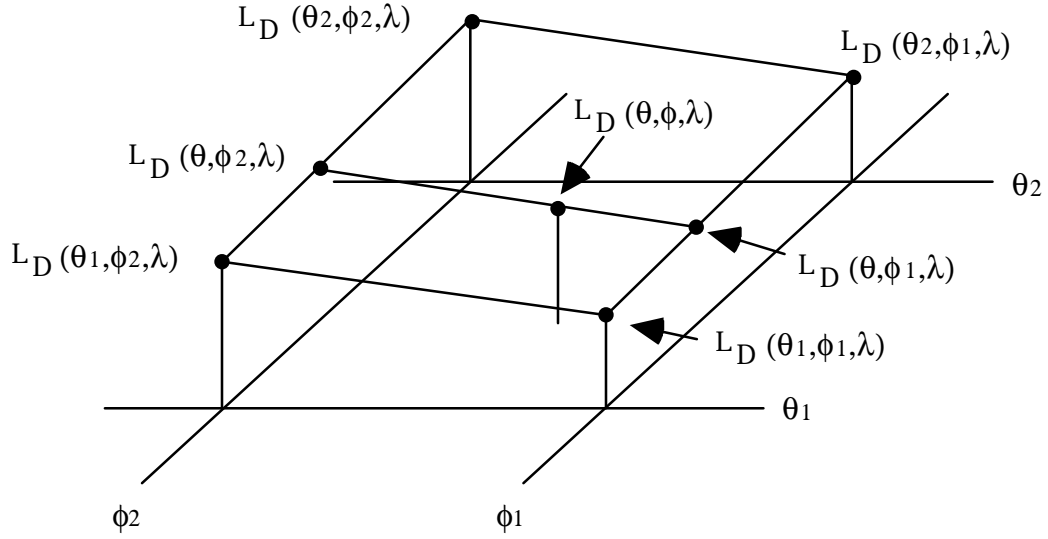


Figure 2.4.1-4 Illustration of the bilinear interpolation method for determining the downwelled sky radiance at a particular azimuth (ϕ) and zenith (θ) angle.

$$L_D(\mathbf{q}, \mathbf{f}, \mathbf{l}) = \frac{(\mathbf{f} - \mathbf{f}_2)(L_D(\mathbf{q}, \mathbf{f}_1, \mathbf{l}) - L_D(\mathbf{q}, \mathbf{f}_2, \mathbf{l}))}{\mathbf{f}_1 - \mathbf{f}_2} + L_D(\mathbf{q}, \mathbf{f}_2, \mathbf{l}) \quad 2.4.1-1$$

where

$$L_D(\mathbf{q}, \mathbf{f}_1, \mathbf{l}) = \frac{(\mathbf{q} - \mathbf{q}_1)(L_D(\mathbf{q}_2, \mathbf{f}_1, \mathbf{l}) - L_D(\mathbf{q}_1, \mathbf{f}_1, \mathbf{l}))}{\mathbf{q}_2 - \mathbf{q}_1} + L_D(\mathbf{q}_1, \mathbf{f}_1, \mathbf{l}) \quad 2.4.1-2$$

and

$$L_D(\mathbf{q}, \mathbf{f}_2, \mathbf{l}) = \frac{(\mathbf{q} - \mathbf{q}_1)(L_D(\mathbf{q}_2, \mathbf{f}_2, \mathbf{l}) - L_D(\mathbf{q}_1, \mathbf{f}_2, \mathbf{l}))}{\mathbf{q}_2 - \mathbf{q}_1} + L_D(\mathbf{q}_1, \mathbf{f}_2, \mathbf{l}) \quad 2.4.1-3$$

For a diffuse target, the directional downwelled radiance database described above is integrated over the hemisphere and spectral values are defined as

$$L_D(\mathbf{l}) = \int_{f=0}^{2P} \int_{q=0}^{\pi/2} L_D(\mathbf{q}, \mathbf{f}, \mathbf{l}) \cos(\mathbf{q}) \sin(\mathbf{q}) d\mathbf{q} d\mathbf{f} \quad 2.4.1-4$$

The downwelled radiance values described in Equations 2.4.1-1 and 2.4.1-4 are based on repeated runs of the SVGSM atmospheric transmission and path radiance code. Spectral values for the emitted and scattered solar downwelled radiance are extracted from the combined radiance field reported by the SVGSM and used to form two independent databases for each of these contributors. The quantities described in Equations 2.4.1-1 and 2.4.1-4 then correspond to those values used in Equations 2.4-1 and 2.4-2 describing the radiance field reaching the sensor for specular and diffuse targets. For example, $L_{DS}(\theta_{SK}, \phi_{SK}, \lambda)$, is the directional downwelled radiance due to solar scattering and is arrived at using Equation 2.4.1-3.

2.4.2 Sky obstruction factor (shape factor)

The amount of "sky light" or downwelled radiance which is impinging on a target is determined by several factors. The most prominent parameter in the reflective portions of the spectrum is the amount of scattering present in the atmosphere. The amount of scattering is determined by the atmospheric constituents, namely molecular scattering elements, aerosols, water vapor and particulate matter (such as volcanic effluents). The amount of "sky light" reaching the ground depends on the relative positions of the sun and the target. The distribution of the scattered radiance field is defined by the shape of the scattering phase function for a particular constituent. The LOWTRAN 7 code (on which the MODTRAN and SVGSM codes are built) considers the atmosphere to be made up of aerosol and molecular scattering elements. These elements are described by phase functions which indicate the probability density with which radiance is scattered into a given direction. The angular distribution from these two scattering sources are combined by weighting with the appropriate scattering coefficients.

LOWTRAN 7 phase functions are normalized such that the integral over all possible scattering directions is unity, namely

$$\iint_{4\pi} P(\mathbf{g}) d\Omega = 1 \quad 2.4.2-1$$

where $P(\gamma)d\Omega$ is the fraction of the scattered radiation that is scattered into a solid angle $d\Omega$ about an angle γ relative to the direction of the incident energy.

Aerosols scattering is handled using either the standard phase functions stored in the LOWTRAN 7 model, the Henyey-Greenstein type phase functions with a user-specified value for the asymmetry parameter, or a user defined phase function.

The standard phase functions are defined at 27 different wavelengths between 0.2 and 40 μm chosen to highlight significant features in refractive indices of aerosol particles. Each phase function is defined at 34 different angles. Mies scattering theory for spherical particles is used to define phase function which allows the modeled functions to all fall within 20 percent of the actual distributions. This spherical theory is valid only for liquid aerosols and not for dust-like or dry particles, for which no closed form expression is available.

The Henyey-Greenstein type phase functions allow for asymmetric scattering around the particles. The phase function is given by

$$P_{HG}(\mathbf{g}) = \frac{1}{4\pi} \frac{(1 - g^2)}{(1 - 2g \cos \mathbf{g} + g^2)^{3/2}} \quad 2.4.2-2$$

where γ is the scattering angle and g is the asymmetry parameter given by

$$g = \iint_{4\pi} \cos \mathbf{g} P(\mathbf{g}) d\Omega \quad 2.4.2-3$$

with $P(\gamma)$ normalized as shown in 2.4.2-1. The asymmetry parameter can vary between the value of +1 for complete forward scattering and -1 for complete backward scattering. An asymmetry factor of 0 indicates isotropic or symmetric scattering.

User defined scattering phase functions can be defined at up to 50 different angles for the four different altitude layers defined in LOWTRAN 7; the boundary layer, troposphere, stratosphere and upper stratosphere.

Molecular scattering is described according to Rayleigh scattering theory. The Rayleigh scattering phase function is given by

$$P(\mathbf{g}) = \frac{3}{16\pi} \frac{2}{2 + \delta} [(1 + \delta) + (1 - \delta) \cos^2 \mathbf{g}] \quad 2.4.2-4$$

where δ is the depolarization factor that corrects for depolarizing effects of scattering by anisotropic molecules. For symmetric molecules, there is no depolarization and δ goes to zero reducing Equation 2.6.2-4 to

$$P(\mathbf{g}) = \frac{3}{16\pi} [1 + \cos^2 \mathbf{g}] \quad 2.4.2-5$$

which is the more common representation for Rayleigh scattering phase functions.

In the emissive portions of the spectrum, scattering of sky radiance is no longer the prominent component of the downwelled radiance field, rather self-emission of the atmosphere takes over. The kinetic temperature of the atmosphere (including all the gases, aerosols, water vapor and particulates) results in a radiance source propagating energy down onto the target. The governing factors in the production of this radiance field is the concentration and molecular properties (such as emissivity) of these atmospheric constituents.

Once the scattering characteristics of the atmosphere are defined by one of the above methods, the amount of radiance which is downwelling from the sky is computed using Equation 2.4.1-3 or 2.4.1-4. This downwelling radiance field, from the hemisphere above the target can then be modified by adjacent background objects to the target. Every object within a scene which extends above the plane formed by the target, obscures a portion of the sky, therefore, reducing the amount of radiance falling onto the target. The fraction of the sky to which a target is exposed is referred to as the target's shape factor, F . Figure 2.4.2-1 illustrates this concept.

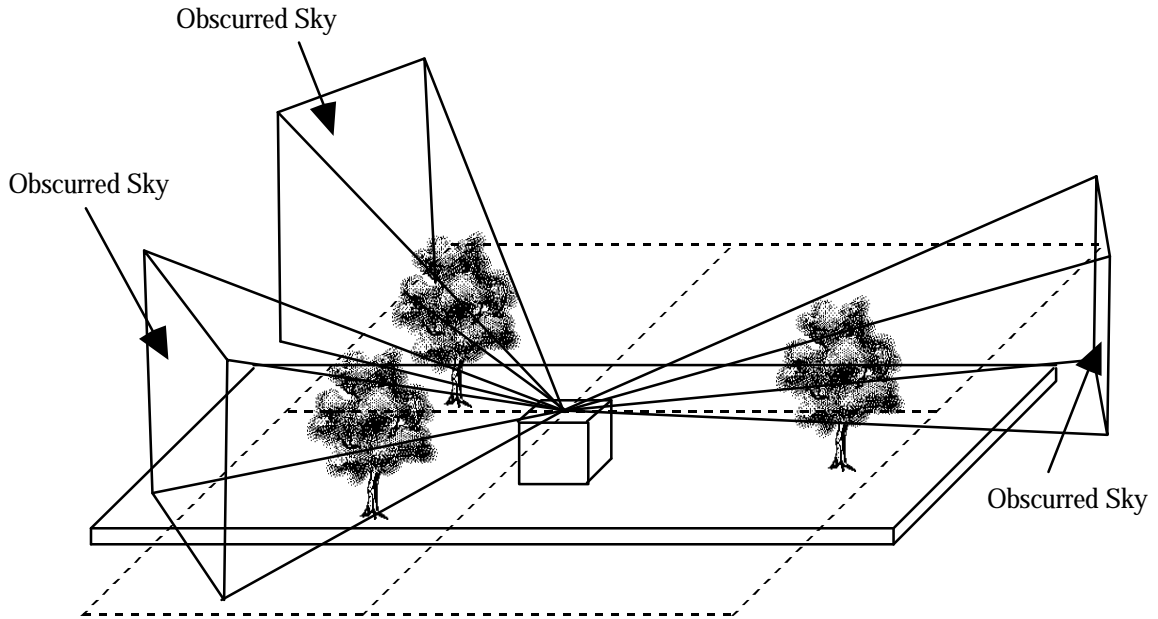


Figure 2.4.2-1 Background objects obscure a portion of the hemisphere above a target limiting the portion of the downwelled "sky radiance" field which can fall onto a target.

In order to determine the percent of non-obscured sky, or the shape factor F , again ray tracing techniques can be employed. Once a primary hit point on the target has been defined, rays are cast out in a regular interval in azimuth and zenith and the number of rays which result in "hits" are recorded. The fraction of rays which hit an object weighted by the solid angle covered by each ray ($1-F$) is used to compute the portion of non-obscured sky or the shape factor (F). The shape factor is computed as

$$F = 1 - \frac{\sum_{q=0}^{p/2} \sum_{f=0}^{2p} h \sin(q) \Delta q \Delta f}{2p} \quad 2.4.2-6$$

where θ and ϕ are the zenith and azimuth angle for each ray cast and h is a binary flag indicating whether or not the cast ray intersects a background object (1 if a hit occurs, 0 if the ray misses all background objects). The rays have their origin at the point where the current ray hits the target of interest and a direction vector defined by (i,j,k) where

$$i = \cos \mathbf{q} \cos \mathbf{f}$$

$$j = \cos \mathbf{q} \sin \mathbf{f}$$

$$k = \sin \mathbf{q}$$

2.4.2-7

The resolution with which the azimuth and zenith angle are varied will affect the quality of the determined fraction. For this study, azimuth is stepped in 30° increments while zenith is changed in 15° increments (finer angular increments would provide a better approximation but would cause significant increases in model execution time).

In addition to determining the percentage of the sky which is obscured from the target, the procedure just described also serves to define the radiance contributions from background objects. While blocking the downwelled sky radiance from the target, these obstructions also serve as sources of energy which falls on the target. In the emissive portion of the spectrum, the kinetic temperature of these background objects create a source of incoming radiance for the target. In the reflective portion of the spectrum, they serve to reflect solar energy onto the target. During the procedure to determine the shape factor, each time a background object is encountered, its material type and temperature are noted. When completed, the average temperature of all encountered background objects is computed and used for the term TB in Equation 2.4-2. The emissivity term, ϵ_B , in Equation 2.4-2 is defined as the emissivity of the most commonly occurring background encountered during the search. For example, if 5 rays hit trees and 8 rays hit concrete structures, the spectral emissivity for concrete is used for the term ϵ_B .

2.4.3 Radiometric interaction with clouds (transmissive objects)

The presence of transmissive objects in the simulated scene requires that many additional interaction be characterized. These object will attenuate radiation along the source-target, sensor-target, background-target and source-background paths and affect the predicted radiance field at the sensor. These objects will also act as sources contributing to the downwelled radiance field and the upwelled path radiance. Figure 2.4.3-1 illustrates these interactions. In order to properly simulate the effects produced by these targets, one needs to define the radiometric properties of the transmissive object. These properties include the thickness of the object along the path of propagation and the spectral extinction coefficients for the transmissive medium.

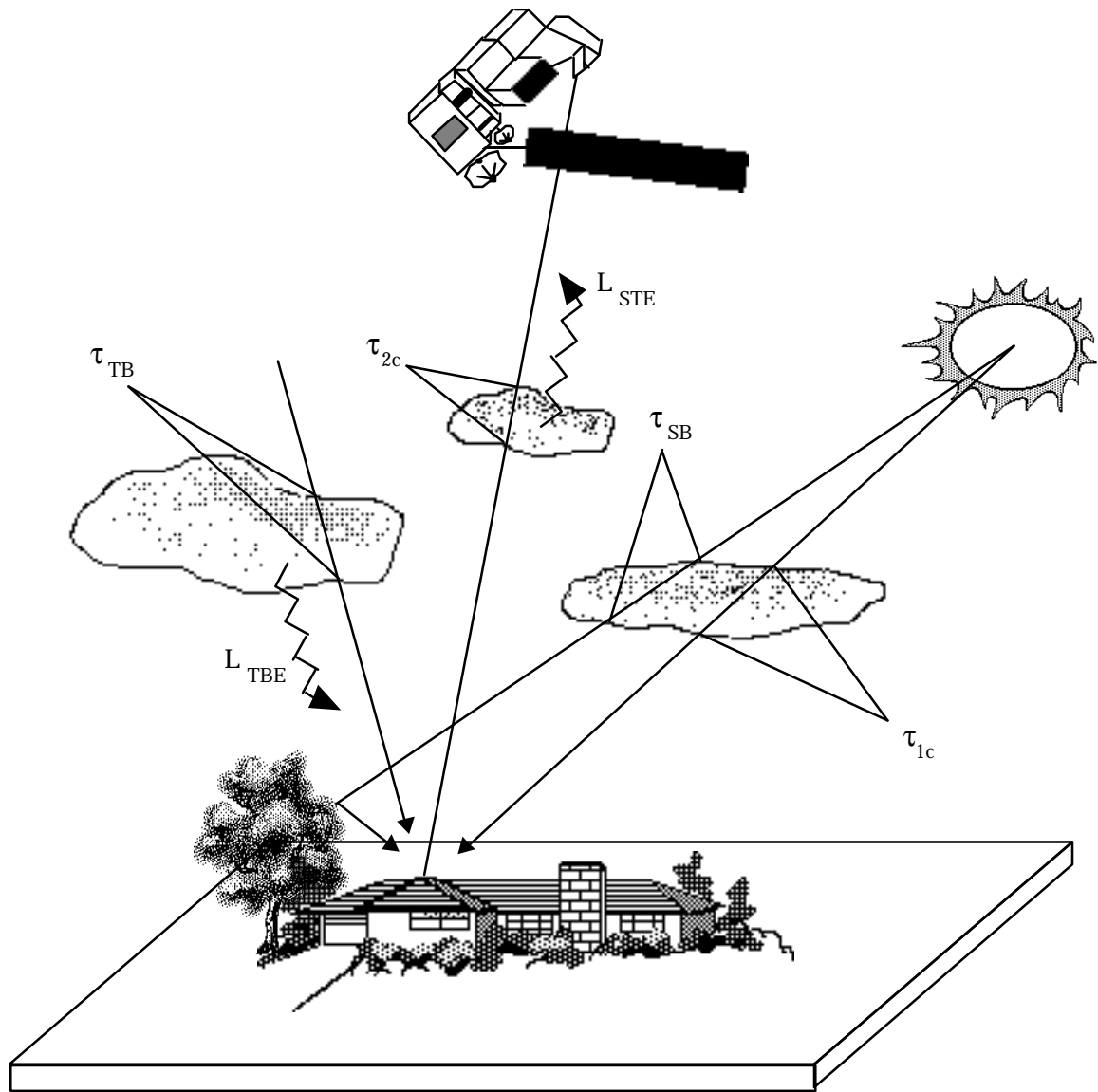


Figure 2.4.3-1 Simulated radiometric interactions caused by the presence of clouds in the scene.

Ray tracing techniques can be used to determine the thickness of an object. As rays are cast and encounter a transmissive object, the point of first contact is recorded. The surface normals are then reversed for that object and the ray cast again. With the normals reversed, the first surface of the object is passed through and the second (exiting) surface encountered. By recording the three-dimensional coordinate of this second intersection, a difference between this and the first surface will provide the object thickness along the path. This is illustrated in Figure 2.4.3-2.

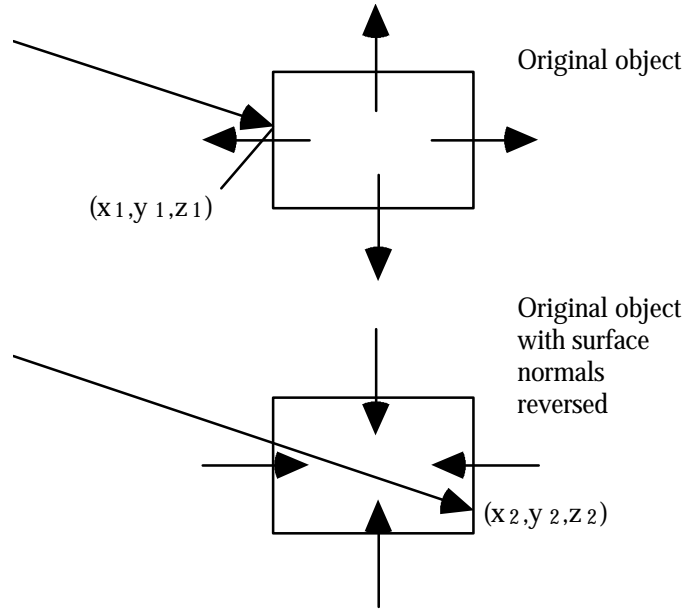


Figure 2.4.3-2 Determination of object thickness along the path of propagation.

The spectral extinction coefficients for translucent objects must be determined by measurements or theoretically derived for a particular material. For the simulation of clouds presented here, the extinction coefficients were determined using the LOWTRAN 7 code and the standard cloud models contained in it. LOWTRAN 7 contains models for cumulus, stratocumulus, stratus, nimbostratus and altostratus clouds. The model places these clouds in the atmospheric column as described in Table 2.4.3-1. In order to derive these spectral extinction coefficients, two runs of the LOWTRAN 7 code are required. First the model is run with no clouds in the atmosphere and the spectral transmission values recorded. The appropriate cloud model is then inserted and the code run again, recording the spectral transmission values for this second run. Since the spectral transmission through the cloud and the atmosphere, $\tau_{CA}(\lambda)$, determined by the latter LOWTRAN 7 run can be defined as

$$t_{CA}(I) = t_C(I) t_A(I) \quad 2.4.3-1$$

where $\tau_C(\lambda)$ is the transmission through the cloud itself and $\tau_A(\lambda)$ is the transmission through the atmosphere (without the cloud) determined by the first LOWTRAN 7 run, the transmission

through the cloud is obtained simply by

$$t_c(I) = \frac{t_{cA}(I)}{t_A(I)} \quad 2.4.3-2$$

This transmission value can also be defined as

$$t_c(I) = e^{-b_c(I)z} \quad 2.4.3-3$$

where $\beta_C(\lambda)$ is the spectral extinction coefficient for the cloud and z is the path length through the cloud. The spectral extinction value is then computed as

$$b_c(I) = \frac{-\ln t_c(I)}{z} \quad 2.4.3-4$$

This procedure can be carried out for each cloud model defined in the LOWTRAN 7 code. With these parameters, transmission values for clouds encountered in the simulated scene is easily computed using an equation of the form shown in the 2.4.3-3. Appendix B includes the plots of transmission as a function of wavelength both with and without clouds included in the modeled atmosphere. These data were used to determine the spectral extinction curves used in the DIRSIG model.

Table 2.4.3-1 Parameters defining the geometric parameters governing the cloud models used in the LOWTRAN 7 code.

Cloud Type	Base Altitude (km)	Top Altitude (km)
Cumulus	0.66	3.0
Altostratus	2.4	3.0
Stratus	0.33	1.0
Stratocumulus	0.66	2.0
Nimbostratus	0.16	0.66

While some interactions are unaccounted for in this work, those illustrated account for the major phenomena encountered in the longwave infrared portion of the spectrum (from 8 to 14 μm). Additional interactions need to be implemented to properly simulate all the phenomena that would occur in the reflected portions of the spectrum which include transmissive effects of cloud illumination. This occurs when a cloud is obscuring the target from the sensor but the portion of the cloud which is sensed is shadowed. The cloud will have transmitted energy present at this point from the sun in addition to downwelled sky radiance. This is also true for clouds present in the specular bounce direction from a target, whose bottom sides will have transmitted energy contributing to the radiance field they produce in the direction of the target.

2.4.4 Correction of atmospheric profiles for surface weather data

The current radiance database construction process allows for the complete control by the user of the atmospheric profiles in the SVGM. This allows the model to be used to simulate any particular day's acquisition provided an upper air weather observation record (radiosonde) is available. If such a record is unavailable, the model has several stored atmosphere types which can be used to approximate the conditions desired. Models such as a mid-latitude summer, maritime, sub-Arctic winter, 1976 US standard and others are available in the standard LOWTRAN 7 code. For the tropospheric, stratospheric and upper atmospheric layers, the use of a constant time-based atmospheric profile does an adequate job, however, it does not adequately describe phenomena in the earth's boundary layer since temperature, relative humidity and surface visibility obviously change as time of day progresses.

These surface weather observation data can be obtained from local airports on an hourly interval and can be used to correct the radiosonde data used. Modification of this sort can be made and have been implemented as part of this effort. Such modifications are implemented as shown in Figure 2.4.4-1. A linear interpolation is used from the inversion layer altitude since no other

information describing this shape is available.

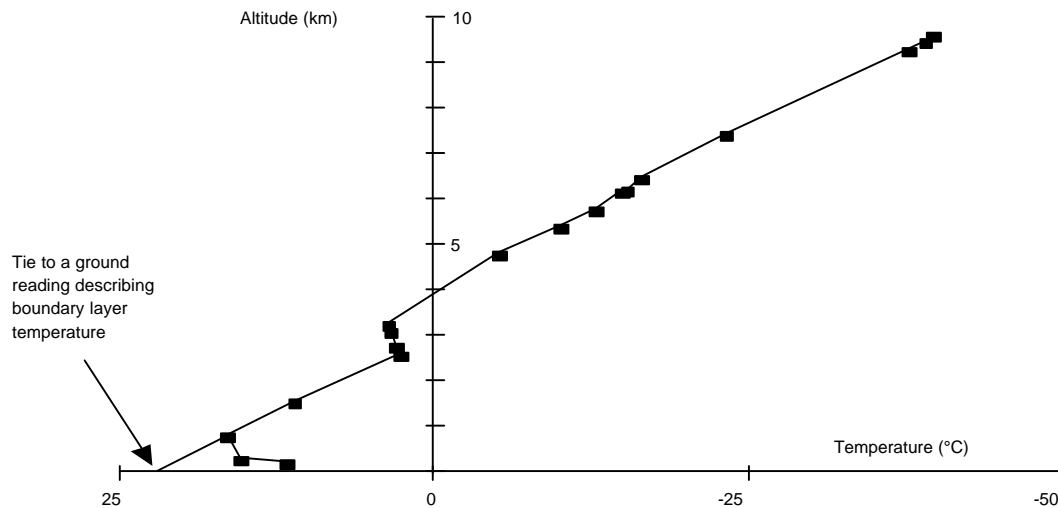


Figure 2.4.4-1 Illustration of possible modifications to descriptive atmospheric profiles of temperature.

2.4.5 Example propagation scenario

The radiometry submodel describes most of the major effects which influence the radiance field reaching the sensor. Cases are covered for completely diffuse targets, completely specular targets whose reflected ray goes to the sky, completely specular targets whose reflected ray encounters a non-sky background, and those cases where the sensor views the sky above the horizon. The MODTRAN atmospheric transmission/upwelled radiance model with the modifications to this code encompassed in the SVGM code provides access to such phenomena as: atmospheric variation due to meteorological conditions (modeled or described), differential path length effects on transmittance and path radiance within the sensor's field-of-view, complete spectral knowledge of all parameters until final sensor integration, variation with zenith angle (isotropic with azimuth) of the downwelling sky radiance, background radiation effects (both reflected solar and emitted), and complete angular broad-band emissivity/reflectivity are modeled. Figures 2.4.5-1 and 2.4.5-2 depict a series of spectral curves produced by the SVGM which define the complete radiance field reaching the sensor. These modeled phenomena enable a very realistic capability for predicting scene radiance. The radiometry submodel has

several residual limitations which have already been described, however, to first-order all of the major phenomena that one might expect to see in real imagery are present in this implementation.

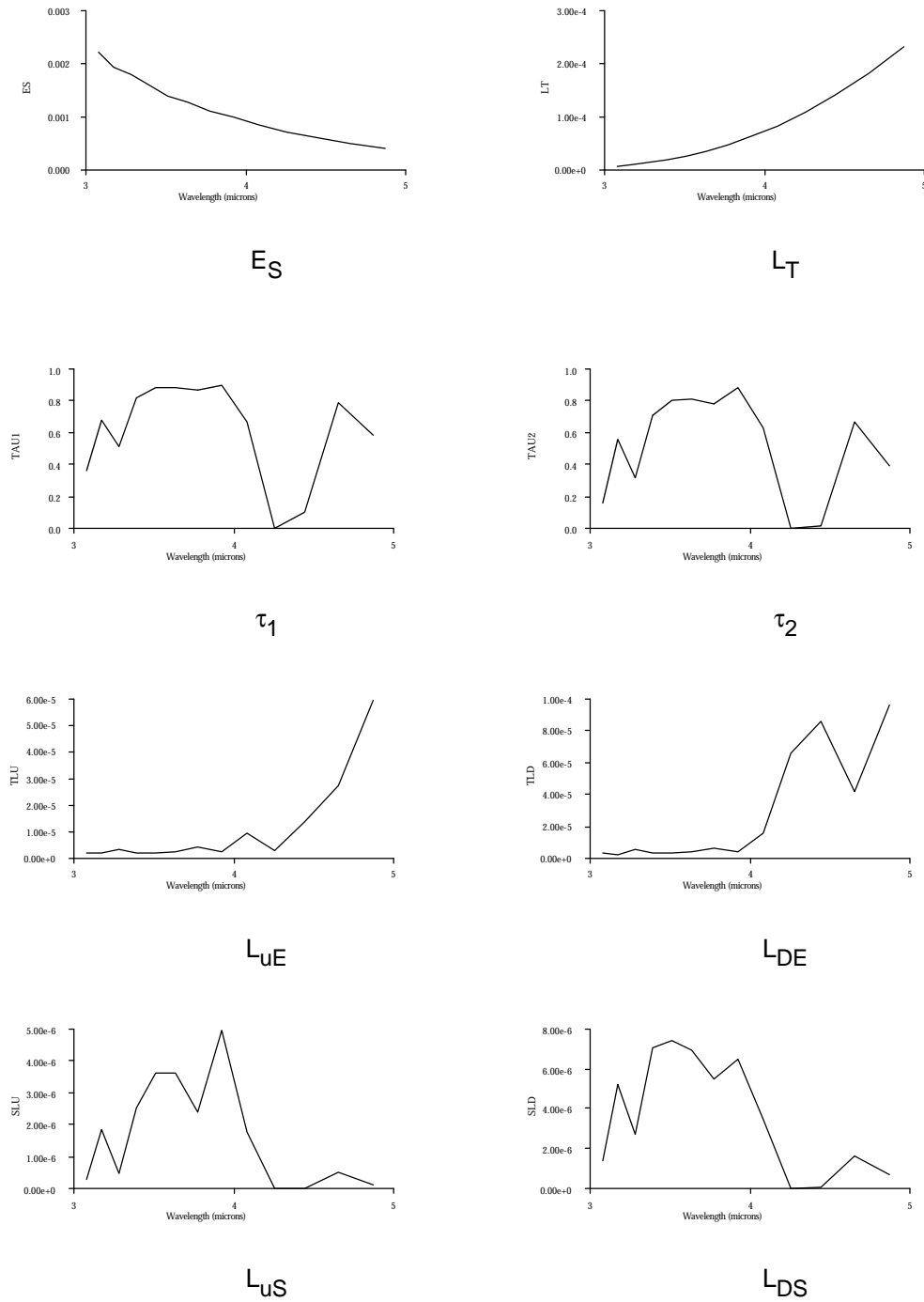


Figure 2.4.5-1 Illustration of the spectral vectors produced by the SVG.

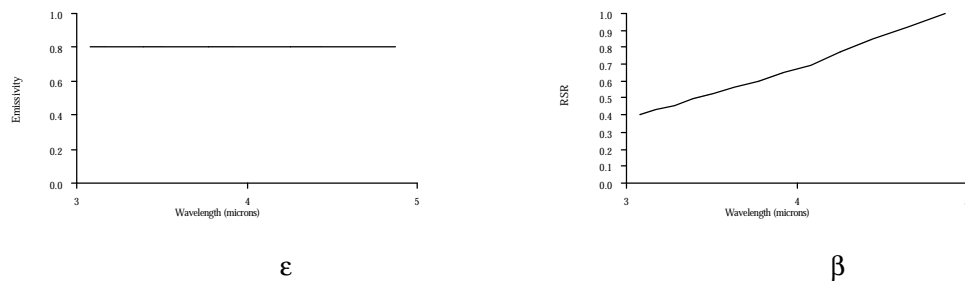


Figure 2.4.5-1 (continued)

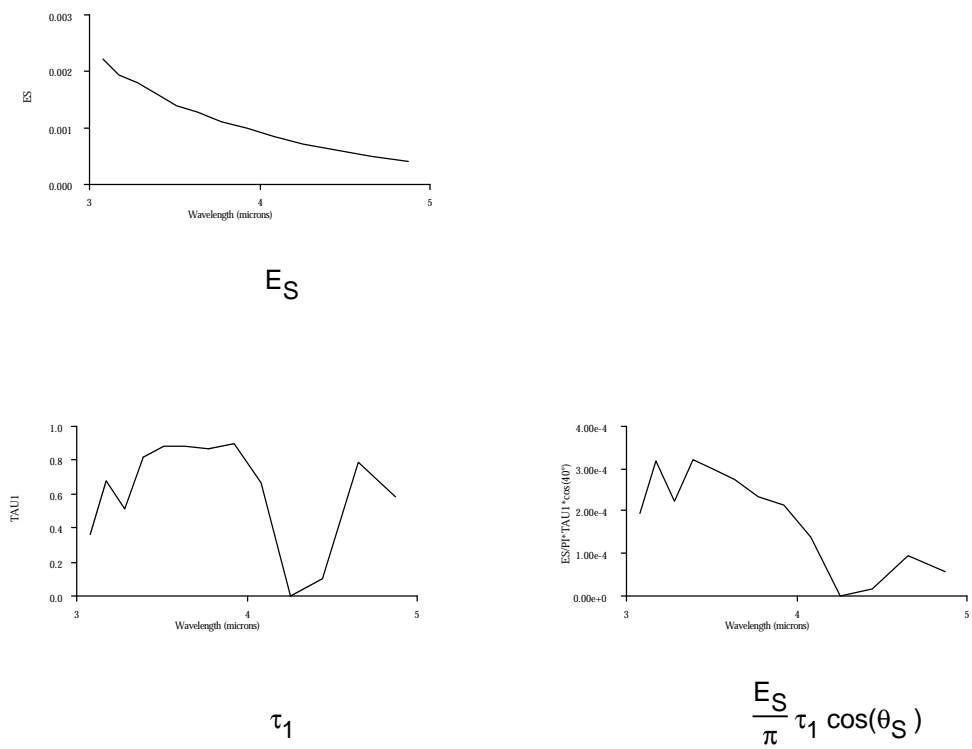


Figure 2.4.5-2 Interactions between those vectors shown in Figure 2.4.5-1 in the formation of the sensor reaching radiance field.

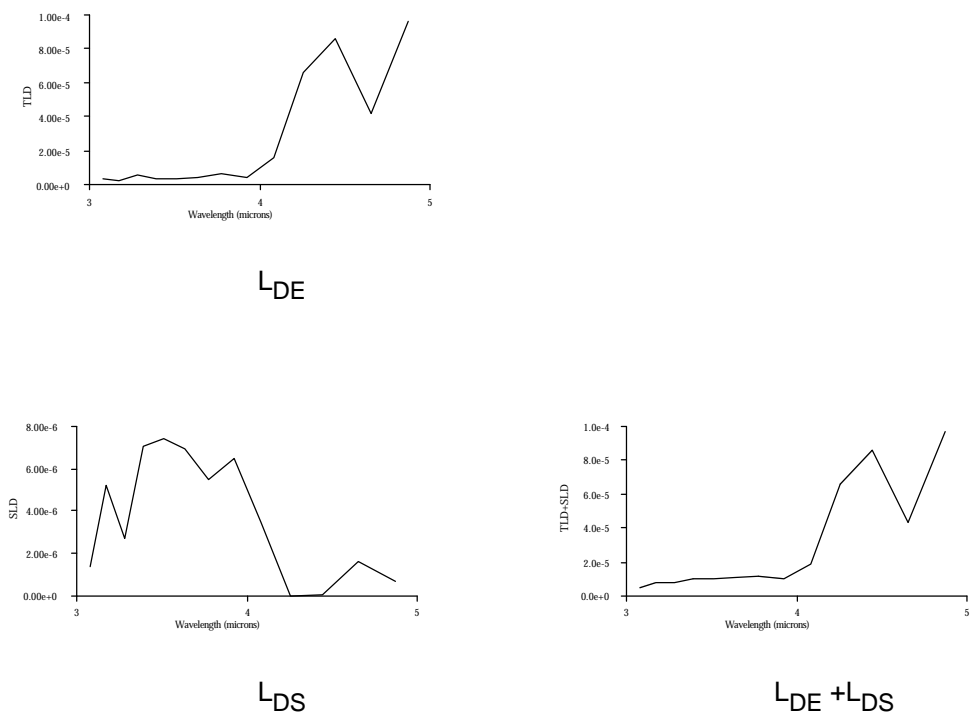
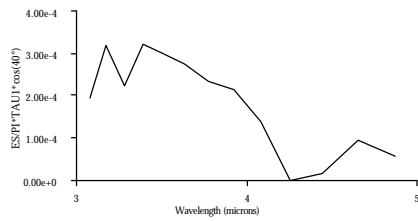
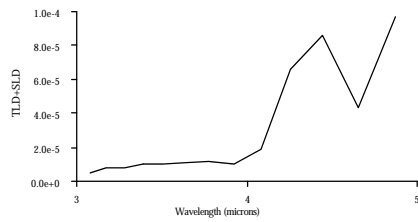


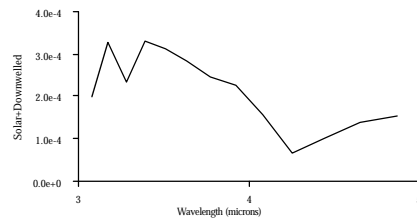
Figure 2.4.5-2 (continued)



$$\frac{E_S}{\pi} \tau_1 \cos(\theta_S)$$



$$L_{DE} + L_{DS}$$

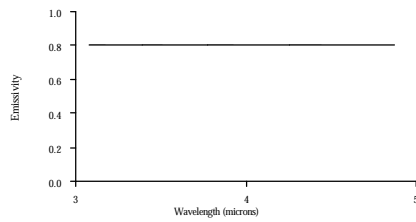


$$\frac{E_S}{\pi} \tau_1 \cos(\theta_S) + L_{DE} + L_{DS}$$

Figure 2.4.5-2 (continued)



$$\frac{E_S}{\pi} \tau_1 \cos(\theta_S) + L_{DE} + L_{DS}$$



$$\varepsilon$$



$$\left[\frac{E_S}{\pi} \tau_1 \cos(\theta_S) + L_{DE} + L_{DS} \right] (1-\varepsilon)$$

Figure 2.4.5-2 (continued)

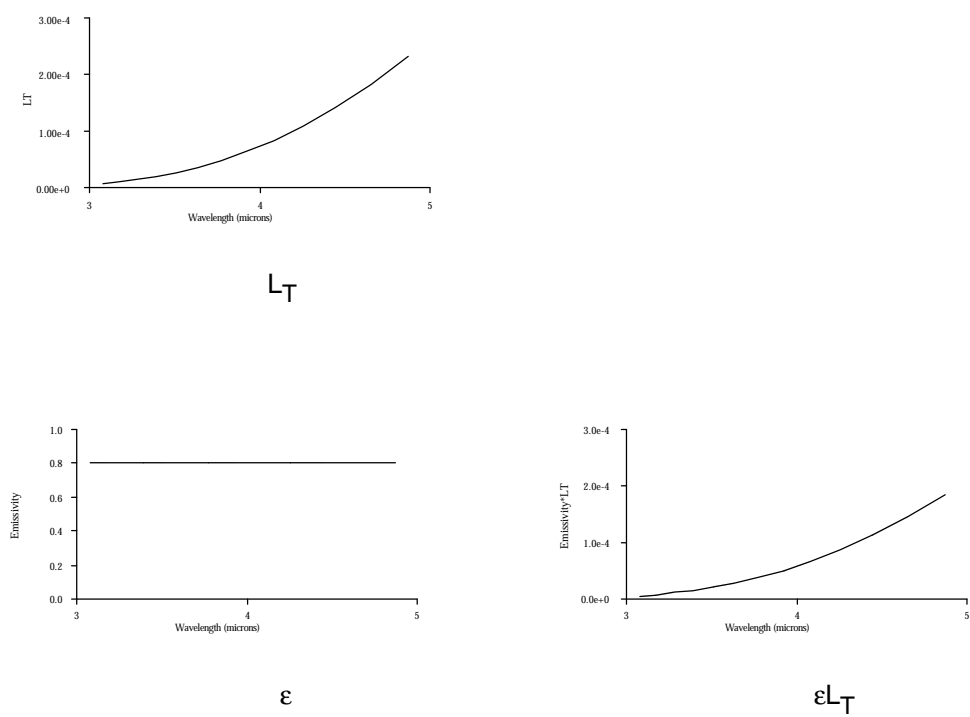
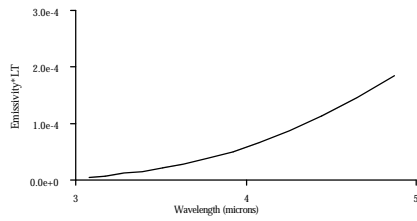


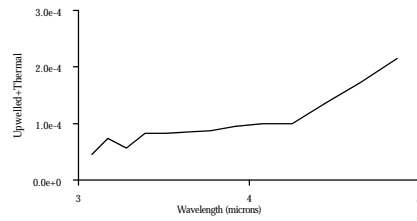
Figure 2.4.5-2 (continued)



$$\left[\frac{E_S}{\pi} \tau_1 \cos(\theta_S) + L_{DE} + L_{DS} \right] (1-\epsilon)$$

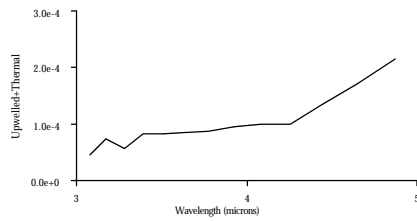


$$\epsilon L_T$$

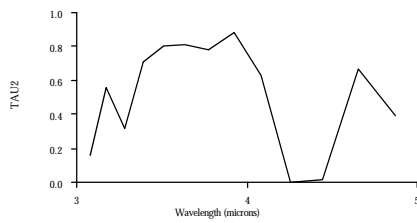


$$\epsilon L_T + \left[\frac{E_S}{\pi} \tau_1 \cos(\theta_S) + L_{DE} + L_{DS} \right] (1-\epsilon)$$

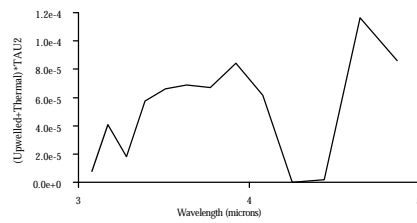
Figure 2.4.5-2 (continued)



$$\epsilon L_T + \left[\frac{E_S}{\pi} \tau_1 \cos(\theta_S) + L_{DE} + L_{DS} \right] (1-\epsilon)$$



τ_2



$$\left(\epsilon L_T + \left[\frac{E_S}{\pi} \tau_1 \cos(\theta_S) + L_{DE} + L_{DS} \right] (1-\epsilon) \right) \tau_2$$

Figure 2.4.5-2 (continued)

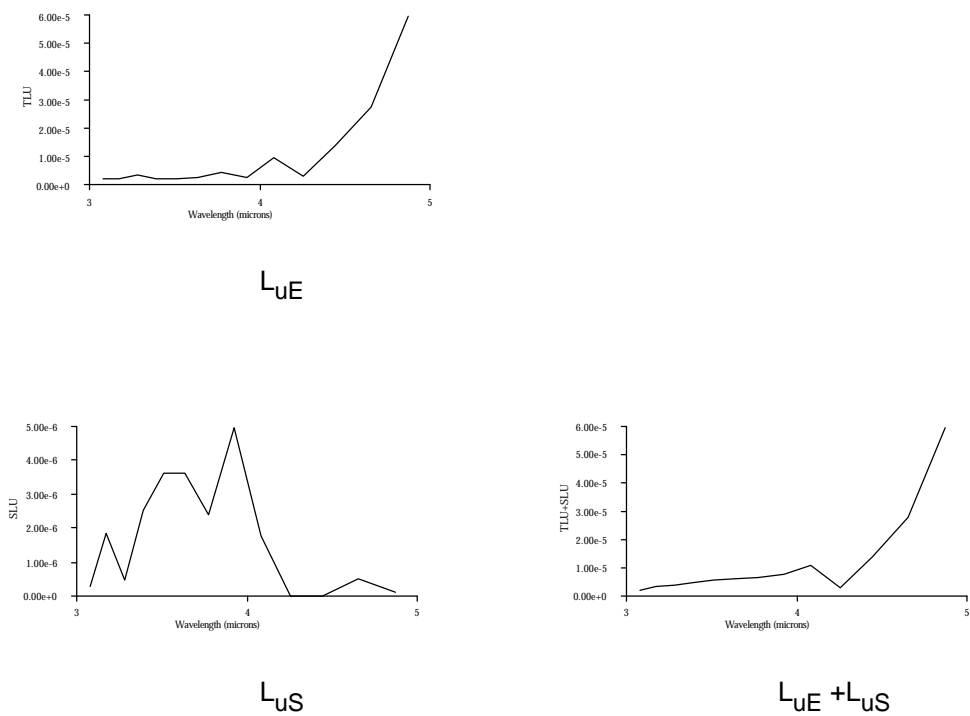
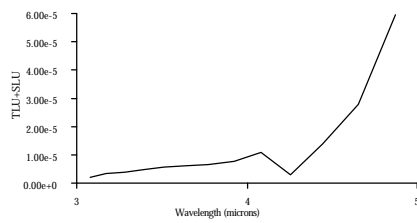


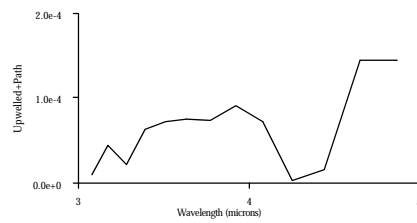
Figure 2.4.5-2 (continued)



$$\left(\epsilon L_T + \left[\frac{E_S}{\pi} \tau_1 \cos(\theta_S) + L_{DE} + L_{DS} \right] (1-\epsilon) \right) \tau_2$$

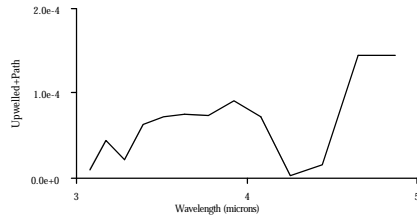


$$L_{uE} + L_{uS}$$

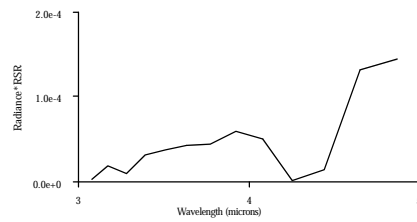
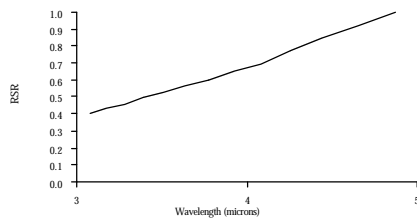


$$\left(\epsilon L_T + \left[\frac{E_S}{\pi} \tau_1 \cos(\theta_S) + L_{DE} + L_{DS} \right] (1-\epsilon) \right) \tau_2 + L_{uE} + L_{uS}$$

Figure 2.4.5-2 (continued)



$$\left(\epsilon L_T + \left[\frac{E_S}{\pi} \tau_1 \cos(\theta_S) + L_{DE} + L_{DS} \right] (1 - \epsilon) \right) \tau_2 + L_{uE} + L_{uS}$$



β

$$\left\{ \left(\epsilon L_T + \left[\frac{E_S}{\pi} \tau_1 \cos(\theta_S) + L_{DE} + L_{DS} \right] (1 - \epsilon) \right) \tau_2 + L_{uE} + L_{uS} \right\} \beta$$

Figure 2.4.5-2 (continued)

2.5 Integration of submodels

The previous sections have described the inner workings of different aspects of the component comprising the DIRSIG model. This section will describe the overall integration of these individual components into a cohesive scene generation code. The ray tracer submodel is the module that integrates the individual submodels to synthesize an overall synthetic scene generation system. The primary task of the ray tracer submodel is to simulate an image produced by a given sensor viewing the 3-D geometric scene. The ray tracer submodel assumes a pin-hole camera optical system. Computer graphics ray-tracing differs in that it extends these calculations beyond the modeled optical system to encompass the modeled scene being imaged. This ray tracing process determines the itinerary and scene interactions of each photon reaching the sensor. This information enables the proper radiance incident on each picture element to be calculated based on energy modified by losses to material absorption, atmospheric attenuation, and energy redistribution due to reflection and self-emission. This accounting process on the resultant energy reaching the sensor should emulate the image produced by a real sensor, given the proper spectral characteristics and accurate submodels.

The secondary task of the ray tracer is to coordinate the simulation process and supply or redirect data to each of the submodels mimicking the different physical phenomena. Figure 2.5.1-1, which is referred to throughout this section, illustrates the input databases, output results, and submodel interactions controlled by the ray tracer submodel. These interactions are described in greater detail in the discussion which follows. Data file formats for those files referred to in the following section are described in Appendix A.

2.5.1 Geometric data base (.gdb) and material data base (.mat)

The 3-D geometrical data base contains all the geometric data defining the facets and corresponding coordinate points, normals, and attributes. This data base information is

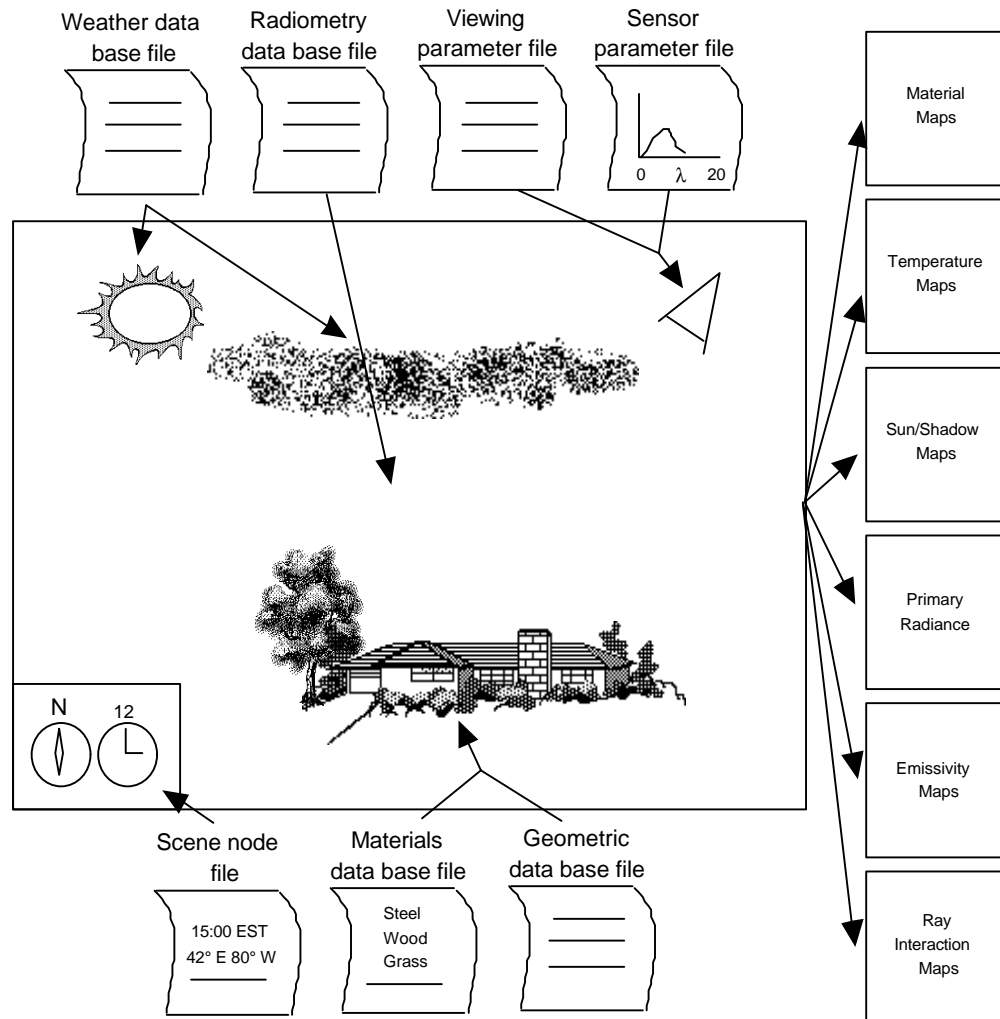


Figure 2.5.1-1 Overall description of the ray tracer submodel's interactions with the supporting data structures.

read and reassembled into the hierarchical tree structure consisting of objects, parts, and facets. For each component at these levels, a 3-D parallelepiped bounding volume defining the physical extents of the component is determined in order to facilitate and expedite ray-facet intersection tests.

The material type of each facet needs to be resolved and expanded. This is accomplished through the input of the material data base file where material-specific physical properties (such as heat capacity and density) and optical properties (such as specularity and angular emissivities) are linked to each facet. This link is accomplished through a unique material code

defined during scene assembly. The material properties contained in the data base were either measured in the laboratory using actual or similar samples, or drawn from published data.

2.5.2 Scene node parameters (.snd) and weather data base (.wth)

The scene inherent in the ray tracer submodel is a generic ideal scene without any interactions with environmental factors that will inevitably affect imaging conditions. The two databases that seed and supply this "real-world" information are the scene node parameter data base file and the weather data base file (*cf.* Figure 2.5.1-1). The scene node parameters define the time, date, and geographic location of the simulation for the scene contained in the ray tracer submodel. This essentially constrains the scene to be simulated to a known set of conditions such as the solar ephemeris and seasonal conditions. The weather database, expressed as a function of time, includes information such as ambient air temperature, barometric pressure, relative humidity, wind speed, etc. can be actual reported weather data or estimated data. As part of the meteorological data, sun position data as a function of time is also included as a modifier to the direct solar loading term. This information is useful in correctly modeling thermal effects of shadowed and non-shadowed areas in the scene as previously described in Section 2.2.1. At this stage of the ray tracer, the kinetic temperature of all the facets are predicted to give a first-order approximation of background temperatures.

2.5.3 Viewing (.adv) and sensor parameters (.sen)

The geometric scene model, influenced by the thermal submodel, represents a simulation domain that is independent of viewing and sensor parameters. By establishing the sensor and viewing parameters, the scene is realized into an image that a specific sensor would see. It should be noted that because the scene was created in the AutoCAD environment, a special effort has been made to utilize parameters from the AutoCAD `camera` viewing command. AutoCAD provides this previewing facility to simulate a 35 mm camera view of the wire-frame scene. This is extremely useful in interactively establishing and visually verifying a given set of viewing parameters prior to a full-scale ray-trace simulation run. The 35 mm format viewing is defined using several parameters. These parameters include the desired target point (in scene world coordinates) to which the camera's optical axis will be pointing, the location of the sensor in world scene coordinates, the azimuth angle of the sensor with respect to the x-axis of the

world coordinates, the elevation angle of the sensor from the xy-plane of the scene, the twist angle of the sensor about the optical axis, the 35mm format equivalent lens length defining the magnification and associated field-of-view of the sensor, and finally the number of pixels per row and the number of rows in the sensor focal plane. Although there are redundancies in the parameters in terms of establishing a unique view, they are included to provide an intuitive check of the attitude of the sensor. With all the previous spatial sensor viewing information, a matrix known as the viewing transformation matrix can be computed to be used as the transforming element that will establish the perspective of all points in the scene as it is viewed from the sensor. This matrix is defined as

$$\mathbf{T} = \begin{bmatrix} \cos f \cos k & \cos f \sin k & -\sin f & 0 \\ \sin w \sin f \cos k - \cos w \sin k & \sin w \sin f \sin k + \cos w \cos k & \sin w \cos f & 0 \\ \cos w \sin f \cos k + \sin w \sin k & \cos w \sin f \sin k - \sin w \cos k & \cos w \cos f & 0 \\ V_x & V_y & V_z & 1 \end{bmatrix}$$

where the angle ω , ϕ and κ define the elevation, azimuth and twist angles of the sensor's orientation with respect to the world coordinate system. The point (V_x, V_y, V_z) defines the view point where the sensor is physically located. A traced ray has the origin described by the view point, (V_x, V_y, V_z) , and a direction vector defined as,

$$\mathbf{D} = (D_x, D_y, D_z) \quad 2.5.3-1$$

where

$$\mathbf{D} = -i \begin{bmatrix} T_{1,1} \\ T_{1,2} \\ T_{1,3} \end{bmatrix} - j \frac{n_x \tan \frac{fov_y}{2}}{n_y \tan \frac{fov_x}{2}} \begin{bmatrix} T_{2,1} \\ T_{2,2} \\ T_{2,3} \end{bmatrix} - \frac{n_x}{2 \tan \frac{fov_x}{2}} \begin{bmatrix} T_{3,1} \\ T_{3,2} \\ T_{3,3} \end{bmatrix} + \begin{bmatrix} T_{4,1} \\ T_{4,2} \\ T_{4,3} \end{bmatrix} \quad 2.5.3-2$$

where (i,j) is the image plane coordinate through which the current ray is being traced (the coordinate $(0,0)$ is defined at the center of the focal plane), fov_x and fov_y are the angular fields-of-view for the optical system and n_x and n_y are the number of columns and rows in the image.

In addition to the spatial and physical parameters of the sensor to be simulated a spectral response file is included to selectively define the wavelength bandpass over which the sensor is sensitive. This is especially important in light of the ensuing radiometry calculations.

2.5.4 Radiometry data base (.rad) file

Having established the major geometric, meteorological, and thermal parameters of the scene and the location and sensor response of the imaging system, the final data base that needs to be defined is the radiometry data base file. This data base supplies the atmospheric transmission and radiance terms which affect the attenuation of the signal reaching the sensor and is expressed as a function of wavelength. At this stage, all components are in place to allow the ray tracer to commence a pixel-by-pixel calculation of the radiance reaching the sensor.

2.5.5 Ray tracer algorithm flow

Figure 2.5.5-1 shows the flow of the different levels of calculation for the radiance reaching the sensor for a single pixel. The calculations begin by retracing the path a photon would take to reach a particular pixel in the focal plane. This is known as casting a ray from the sensor pixel. This involves the definition of a vector starting from the focal point toward the scene. Having defined the starting location and direction of the vector, a test is then made to determine the location where this vector intersects the scene. The determination of this location involves several levels and types of intersection tests to search for the specific facet that contains the "hit" point. These tests were defined in Section 2.3.

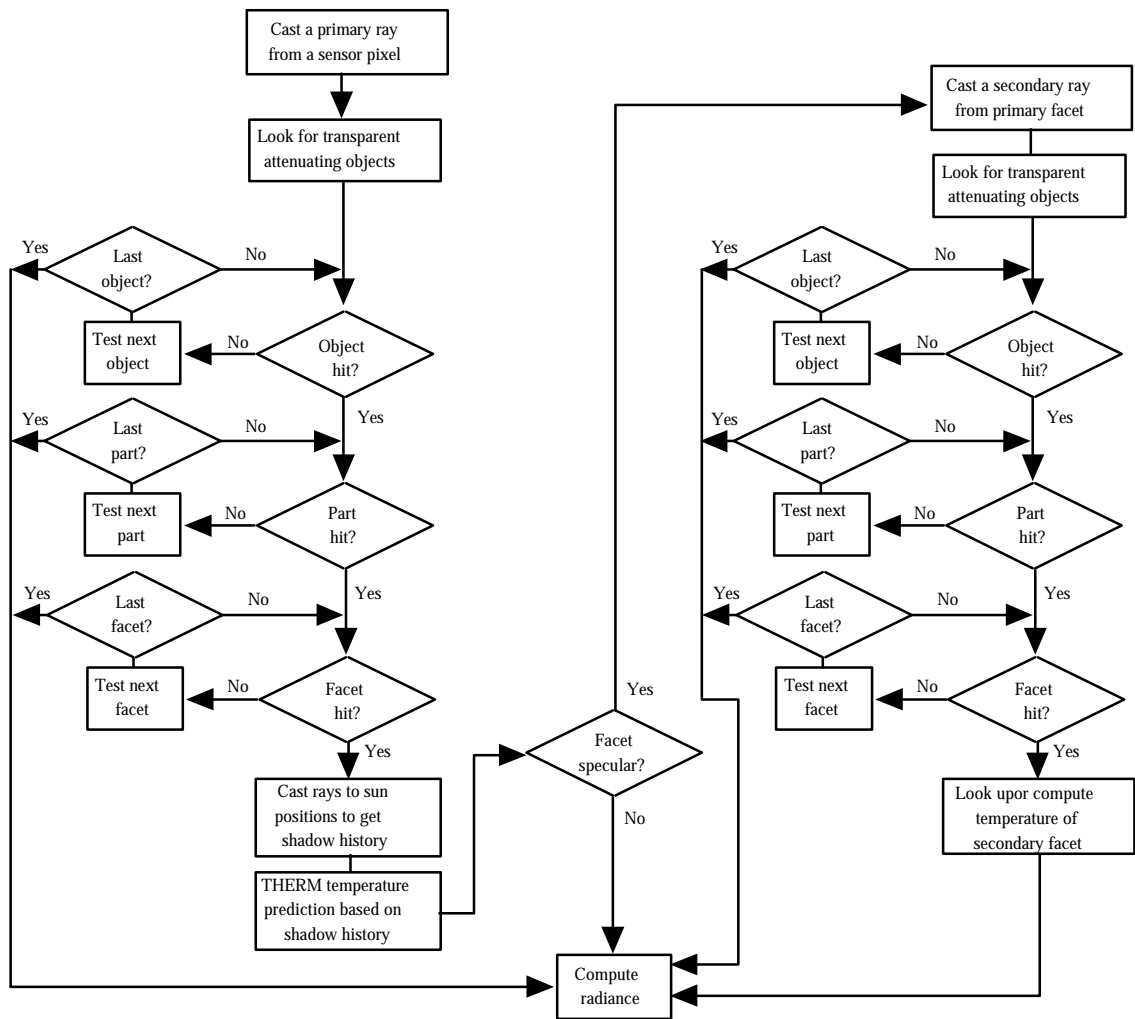


Figure 2.5.5-1 Illustration of the ray tracer algorithm flow for a single pixel.

2.5.6 Target specularity

The final step is to determine the specularity of the facet that has been intersected by the ray. At present, specularity is a binary property for each material where it is either perfectly diffuse or perfectly specular. If a facet is diffuse then the pixel radiance can be computed by the radiometry submodel after the primary ray-facet intersection test. In the case where the facet is specular, a secondary ray will be propagated from the primary intersection point and cast out into the scene in conformity with the laws of reflection. The secondary ray will undergo the same tests which were made with the primary ray to determine if a secondary ray-facet intersection exists with the scene. If a secondary hit does exist, then the temperature of this background

facet will be noted and factored into the radiometry calculation. In cases where no background facet is intersected, the sky is assumed to be the background and the radiance of the primary pixel is calculated accordingly based on the zenith angle of the ray cast to the sky. The number of ray "bounces" (also known as the depth of the ray tracer) necessary to determine the final radiance has been determined by Shor, 1990, to be two bounces for the longwave region. Additional computation of tertiary and quaternary ray-facet intersections results in insignificant contributions to the final radiance in the longwave regions. No determination has been made as to the necessary ray tracer depth for the midwave or reflective regions however the two-bounce assumption has been carried through to these bandpass regions.

In light of the complexity of the interactions governing the creation of the synthetic thermal image, provisions have been made to create intermediate result images or maps of the scene. They provide a helpful debugging tool as well as a method to verify and understand the phenomenology behind the resulting radiance image. These intermediate images include material type, temperature, sun/shadow condition, emissivity, ray-interaction type, and angle maps. Further treatment of these images will be made in the results section.

The ray tracer forwards information on ray interaction types, interaction angles, sun/shadow history, etc. to the thermal submodel and then to the radiometry submodel where final scene radiance values are computed.

The description of the DIRSIG code provided in this section is intended to supply the reader with a complete background and understanding of the principles utilized in the DIRSIG code. The major contribution to the synthetic image generation community is the treatment of the scene radiometry. The strict attention which is given to the physical phenomena which govern energy propagation is beyond that described in the literature for any other current models. This treatment makes the DIRSIG model an excellent tool in teaching about the effects that physical phenomena have on image formation. Analysts can use this tool to determine if hypotheses they form about the origin of particular effects in imagery are correct, systems designers can use this tool to determine whether their proposed sensor will image a scene the way they wish, and academics can use this tool to show students subtle effects present in imagery without costly and time-consuming collections.

3.0 RESULTS AND DISCUSSION

In order to fully understand the components and physical interaction that affect the radiometry behind the synthetic imagery created with the DIRSIG model, a complete end-to-end example will be presented illustrating these aspects. For a single scene, the steps from the original AutoCAD wire frame drawing to the final radiance image will be illustrated. These images do not provide a great deal of information for the operational use of the DIRSIG, but do serve as an excellent means of debugging code during development and modification as well as provide an excellent teaching tool for the description of the imaging chain which is utilized in scene formation.

A scene was constructed which included a number of Soviet Foxbat fighter jets in an airport setting, with background bunkers, vehicles, structures, and a helicopter. This scene was modeled after a scene produced in the ITEK Corporation's scene simulation facility, of which a pan visible scene is shown in Figure 3-1. The synthetic image used for this procedural description is a zoomed-in image of the Foxbat fighter exiting the aircraft hangar.



Figure 3-1

A pan visible (0.4 to 0.7 μm) image for the Foxbat fighter scene created at ITEK's image simulation facility.

Figure 3-2 shows the AutoCAD drawing which depicts this scene. This wire frame consists of 50 objects, 661 parts, and 54545 facets for a total file size of 18.2MB.

Figure 3-3 shows the attribute list defined for an individual facet in the AutoCAD 3-dimensional wire frame. An attribute list like the one shown is constructed for every facet in the scene to serve as input to the THERM thermodynamic model as well as the ray tracing algorithms.

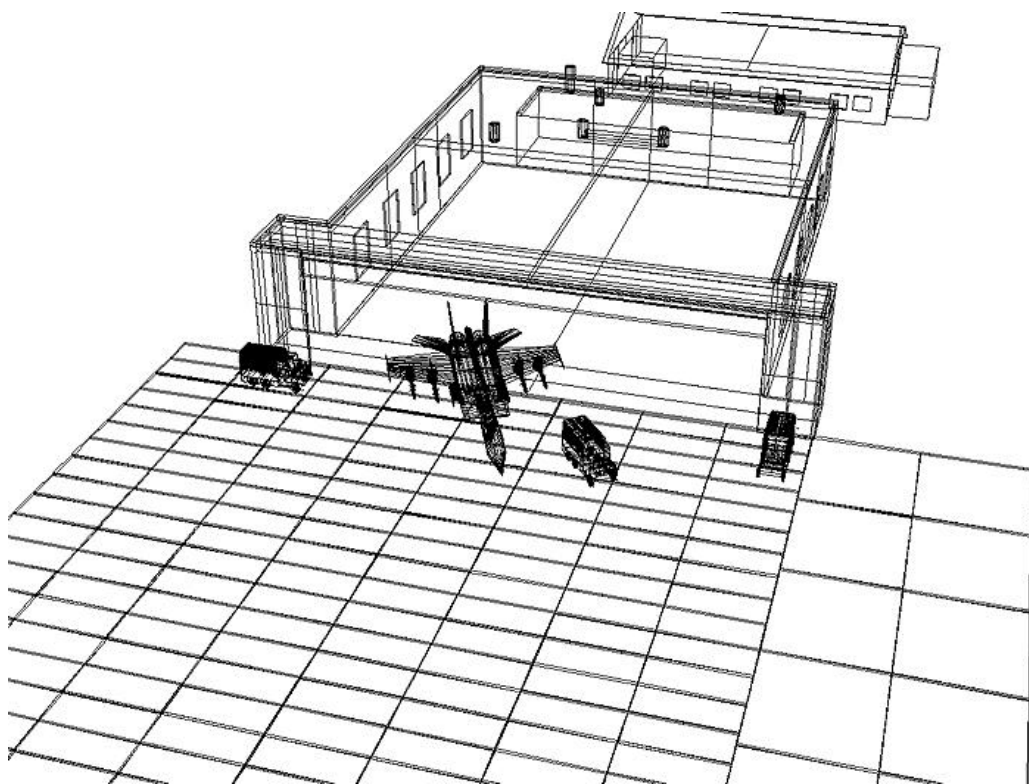


Figure 3-2 AutoCAD wire frame representation of the physical model created in the scene simulation facility.

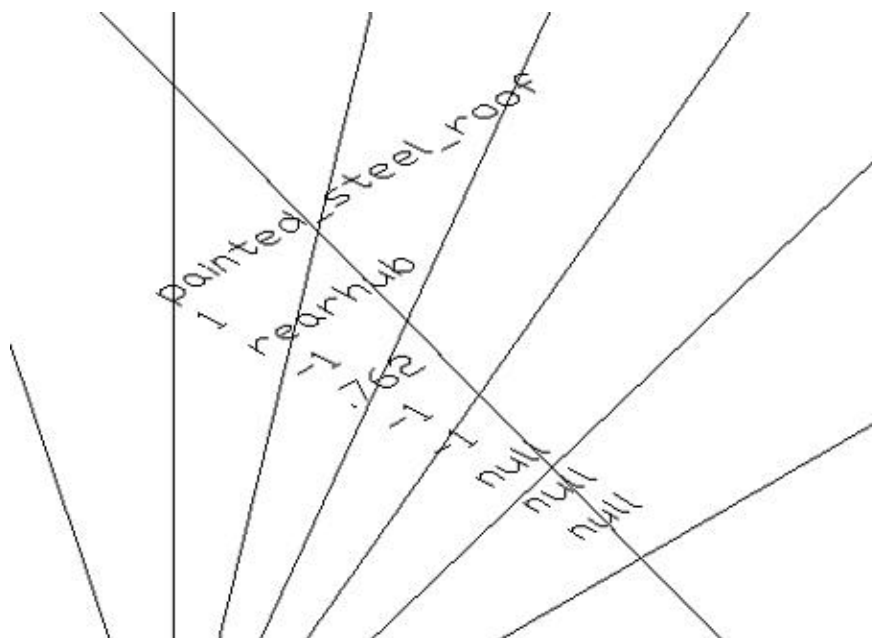


Figure 3-3

A close-up view of a single facet with its associated attribute list. Attributes shown are material name, material code, attribute name, default facet temperature, facet thickness, self-generated power, exposed area, and three blank fields for future use.

During the execution of the DIRSIG model, several images get created in addition to the final radiance scene. These images include a primary and secondary material map, a sun/shadow map for each pixel's primary target and secondary background, a temperature map for the primary target and secondary background, a ray interaction map, a primary target and secondary background emissivity map, a map illustrating the angle between the primary facet normal and the sensor path, and a map representing the shape factor for each pixel. Figures 3-4 through 3-14 illustrate these component/interaction images which are formed for the final radiance scene shown in Figure 3-15.

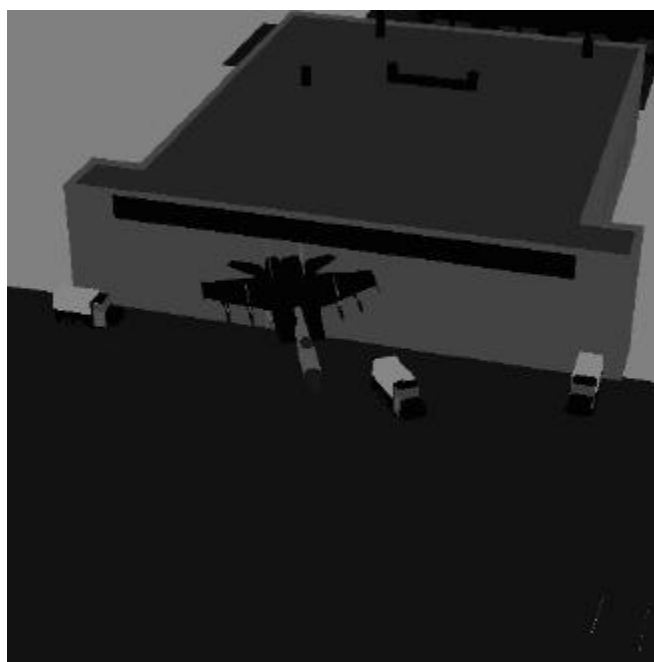


Figure 3-4 Primary target material map illustrating the material code of which each facet is represented in the geometry database.

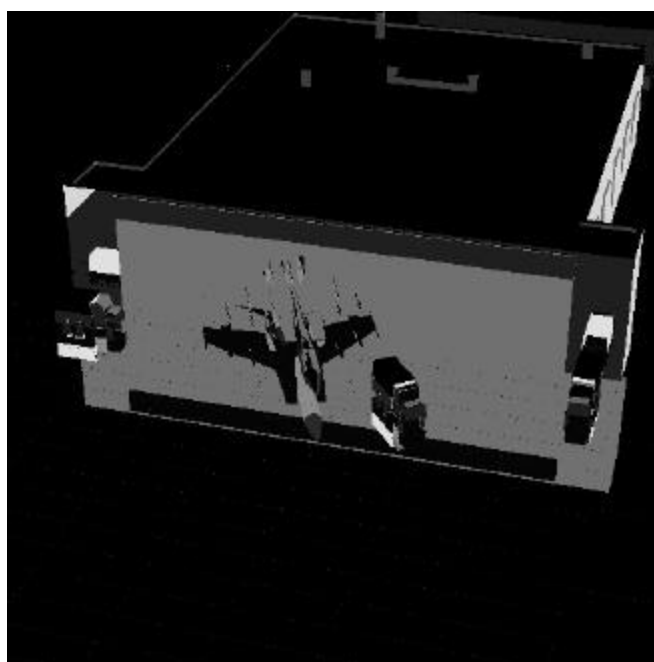


Figure 3-5 Secondary background material map illustrating the material code for the facet which makes up the background for a specular bounce from the current target facet (if one exists).

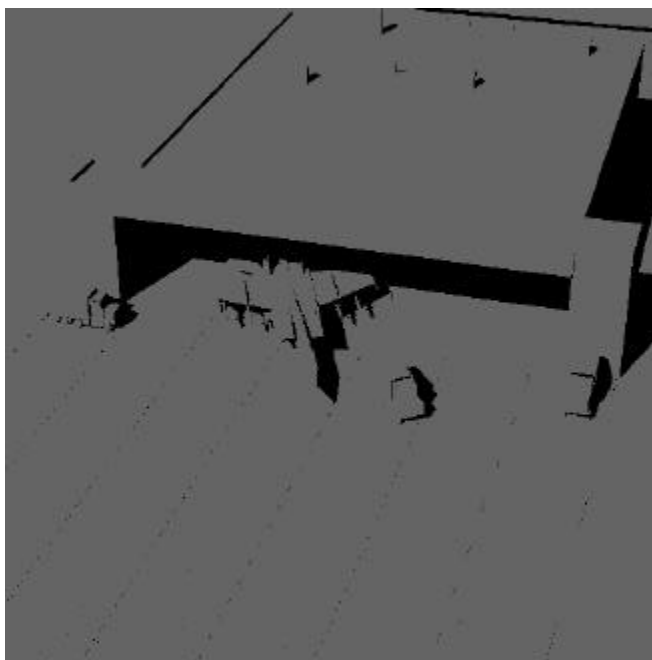


Figure 3-6 Sun/shadow maps depicting the illumination state for the current target pixel at the time of image simulation.

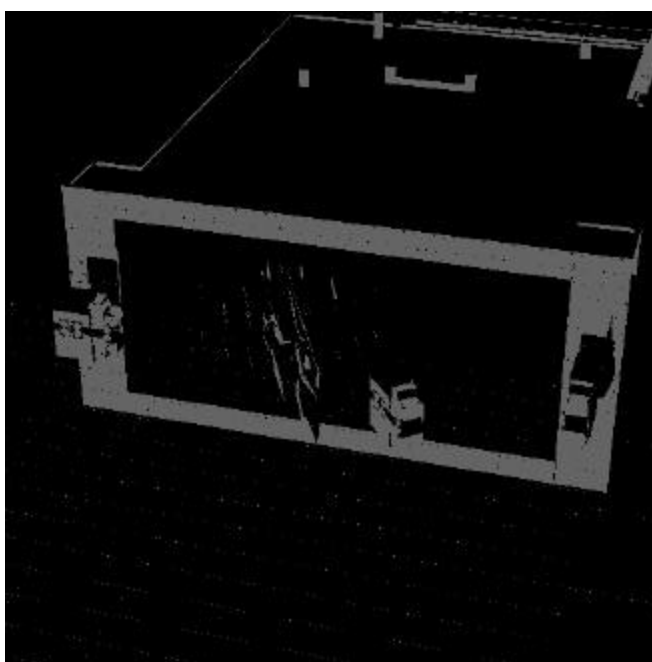


Figure 3-7 Sun/shadow maps depicting the illumination state for the current target's background facet (if there is one) at the time of image simulation.

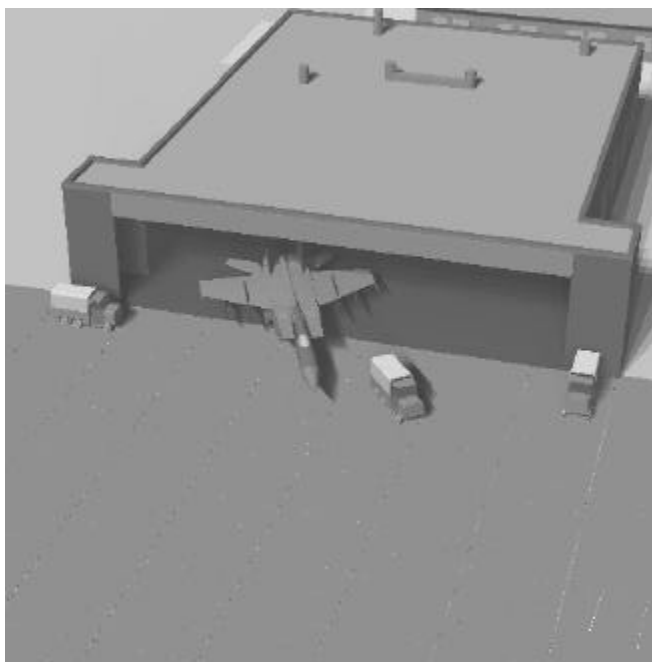


Figure 3-8

Temperature map for the target as computed by THERM using the specified weather history and sun/shadow history for the current pixel.

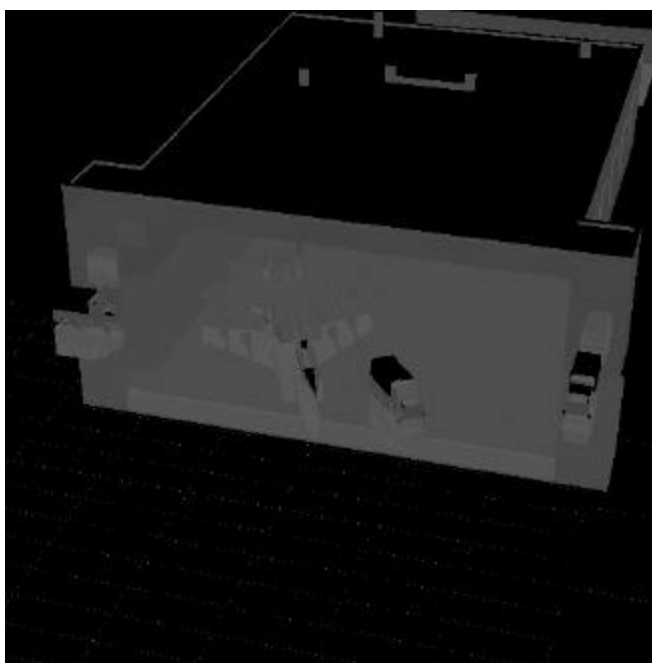


Figure 3-9

Temperature map for the target's background (if there is one) as defined by an initial run of THERM (with no regard for sun/shadow history, e.g. it is kept sunlit).

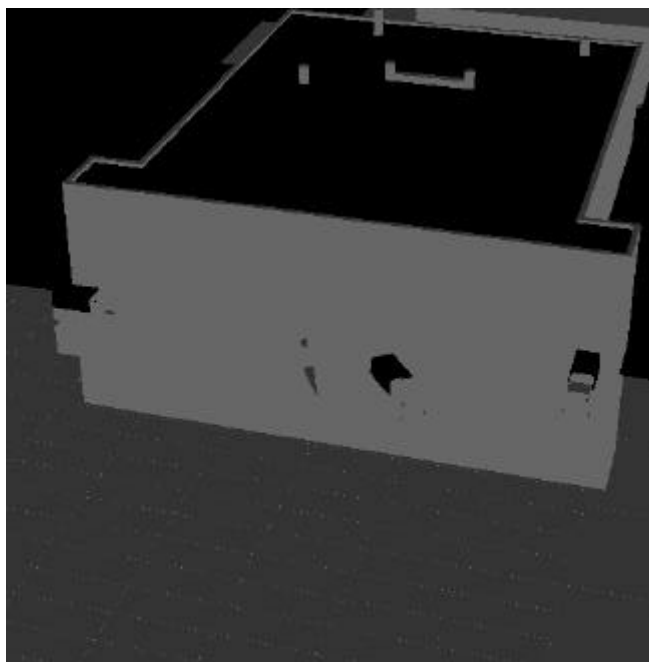


Figure 3-10 Ray interaction map illustrating the type of radiometry computation to be carried out for each pixel (either a diffuse hit, a specular bounce to the sky, a specular bounce to a background object, or a missed scene).



Figure 3-11 Integrated angular emissivity over the bandpass being simulated for the target pixel.

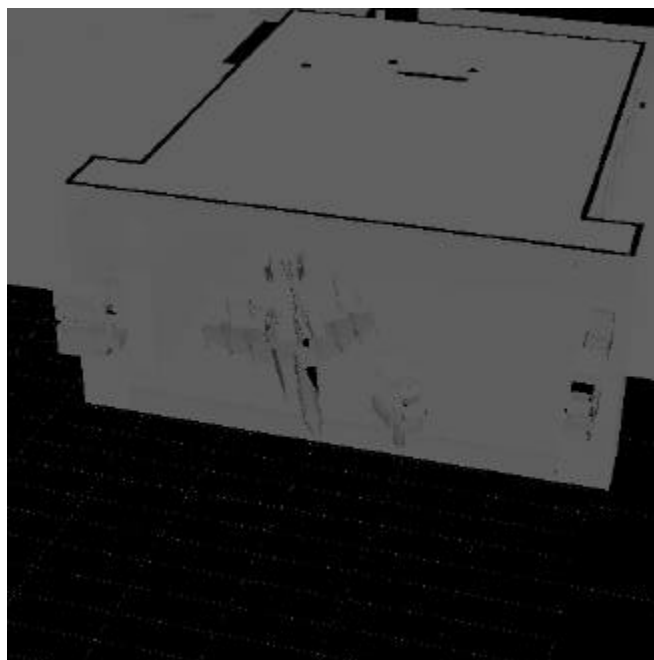


Figure 3-12 Integrated angular emissivity over the bandpass being simulated for the target's background facet (if there is one).

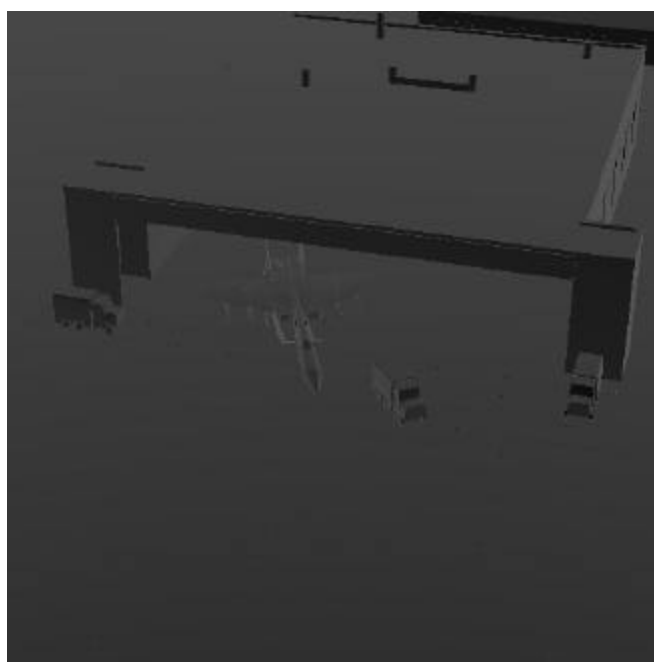


Figure 3-13 Angle between the primary facet normal and the ray cast from the sensor to the primary target hit point (θ in the radiometric computations).

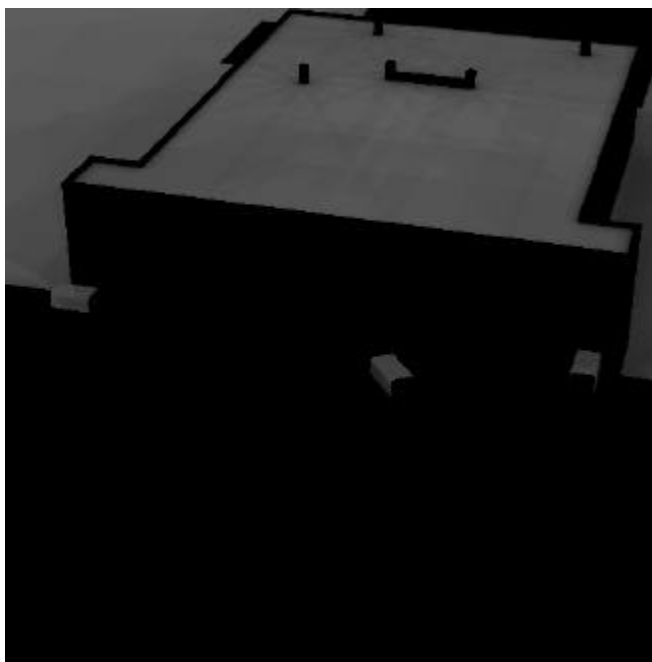


Figure 3-14

The sky obscuration factor for each pixel in the scene used to modify the downwelled sky radiance for diffuse pixels.

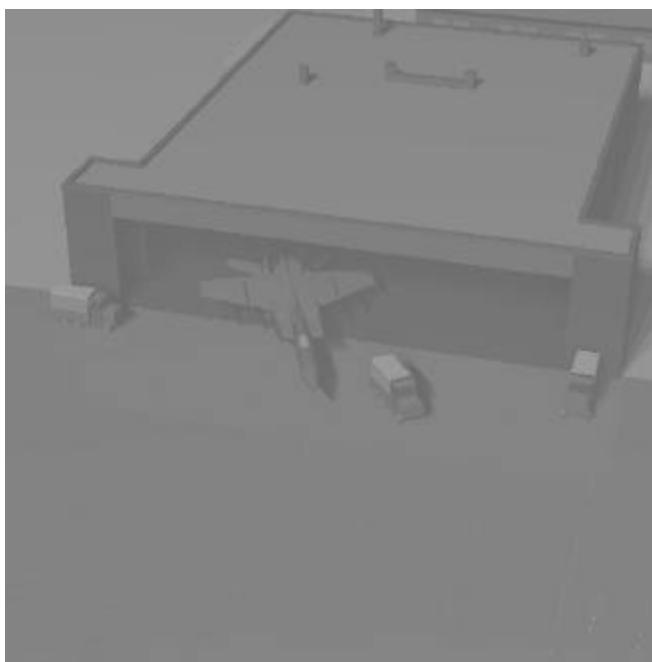


Figure 3-15

Simulated radiance field reaching the front end of the sensor from the Foxbat scene propagated through the atmosphere (the image simulates an acquisition with a sensor in the 8 to 13.3 micron bandpass region, at 10AM local time, on 6/24/87 at 39°46'24"N latitude and 84°06'32"W longitude).

If one examines Figure 3-15 closely, an interesting effect will be noticed. This effect is the presence of what seems to be noise in the tarmac. These single-pixel features are actually a feature of the scene. The tarmac is modeled as a series of concrete slabs, each slab separated by a small space filled with a tar-rubber-like material, just like that used to fill cracks on highways. The spots on the tarmac are remnants of these crack which were simply too small to be resolved in the modeled imaging scenario depicted here. The reason they appear brighter than the concrete slabs is that their thermal properties; specific heat, conductivity, thermal mass, etc., lead to a quicker "heat-up" time than the more thermal massive concrete slabs.

To illustrate some other capabilities of the model created as part of this effort, several other images will be presented. These images will be presented in less detail than was shown in Figures 3-2 through 3-15, only presenting the final radiance image. To illustrate two capabilities of the model simultaneously, a set of images will be presented which represent a true color sensor system with a very low view angle such that a substantial portion of the sky can be seen. This illustrates the capabilities of the DIRSIG model to perform in the visible wavelength portion of the spectrum as well as its ability to predict sky radiance. Figures 3-16 shows the image a west viewing sensor would see as the time of day progressed from sunrise to sunset.

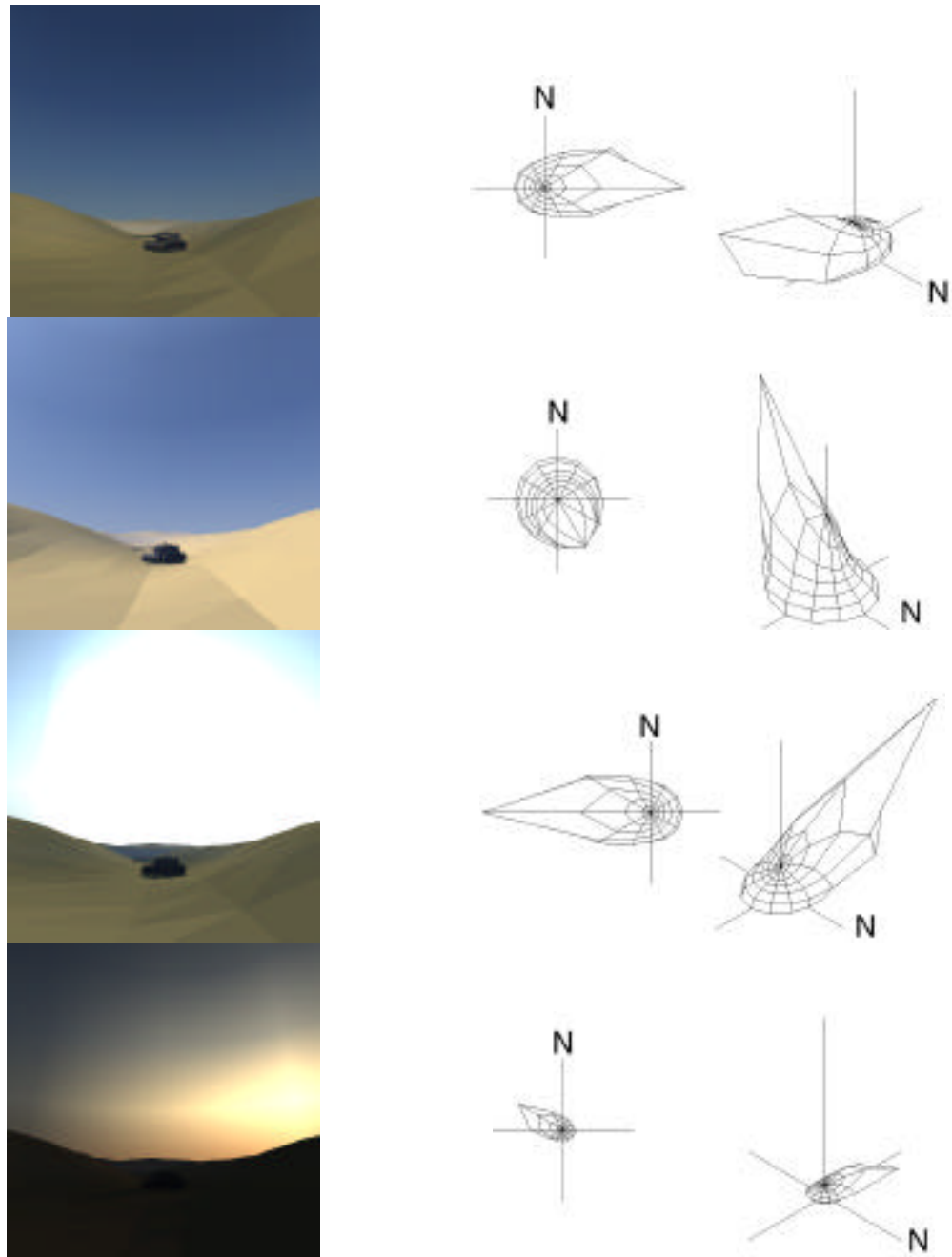


Figure 3-16

True-color images depicting the scenes a westward viewing sensor would see at (a) 08:00, (b) 12:00, (c) 17:00, and (d) 19:00 local time. The plots beside the images illustrate the magnitude of the downwelling sky radiance for these acquisition times (the images simulate acquisitions with a sensor in the 0.4 to 0.5 micron, 0.5 to 0.6 micron, and 0.6 to 0.7 micron bandpass regions, on 6/24/87 at 39°46'24"N latitude and 84°06'32"W longitude).

This previous series of images show that the phenomenology predicted for the sky radiance effects track well with what one would expect. The variation in the sky radiance field brightness tracks well with intuition as well as the radiance plots shown with each image. As the day progresses, the western sky is fairly uniform at sunrise, begins to brighten in the southwest region (upper-left corner) at noon, a saturated solar disk region appears in the due west around 5:00 PM and finally the sunset scene depicts the sun in the northwest (approximately 23° north of west corresponding with the tilt of the earth's axis on the simulated date) with a greatly diminished magnitude.

The following image is a simulation of a sensor acquiring data in the midwave infrared region of the spectrum, 3 to 5 μm , of a desert scene. In this scene are several tents, a roadway and a couple of military vehicles. This scene is of particular interest since it depicts an interesting effect only scene in this bandpass region. This effect is the presence of both shadows from direct solar radiation at the time of image acquisition as well as "thermal shadows" left behind where the background has been differentially heated due to target shadows cast onto it. This effect can be seen if one looks closely at the regions behind the tents in Figure 3-17. The differential heated portions of the background are a direct result of the modifications made to the time-based direct solar insolation vector supplied as input to the THERM model for each pixel in the scene. The amount of direct solar insolation determines the solar load for the current pixel and therefore greatly affects its predicted temperature.

In an experiment directed at the validation of the radiometric submodel contained in the DIRSIG code (Schott *et al.*, 1993), calibrated image data was collected on half-hour centers over a 48-hour period in the longwave and midwave spectral regions. In addition to the image data, meteorological conditions including air temperature, pressure, relative humidity, wind speed, cloud cover, cloud type, and direct and diffuse solar insolation data were collected on 15-minute centers. This data set was used to examine the absolute accuracy and phenomenological prediction capability of the model in these bandpass regions. Figures 3-18 and 3-19 depict a side-by-side comparison of an example data set from the validation experiment with that predicted from the DIRSIG model in the longwave and midwave regions.

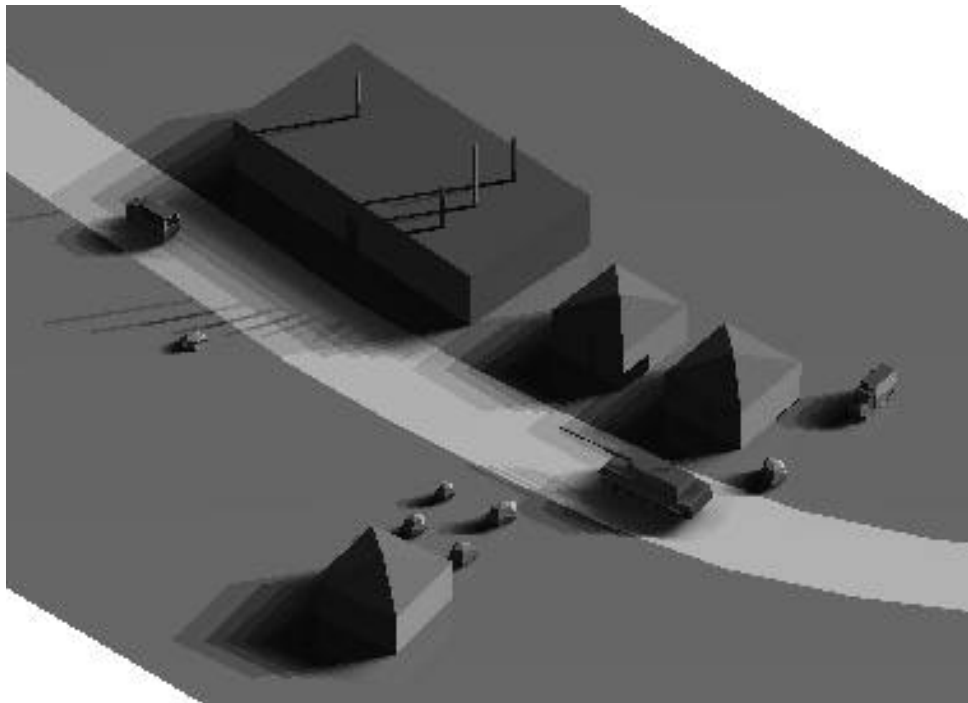


Figure 3-17

A midwave (3 to 5 micron) infrared image of a desert scene illustrating the presence of both directly illuminated solar shadows as well as differential background heating caused by previous sun/shadow history effects (the image simulates an acquisition at 18:00 local time, on 6/24/87 at 39°46'24"N latitude and 84°06'32"W longitude).

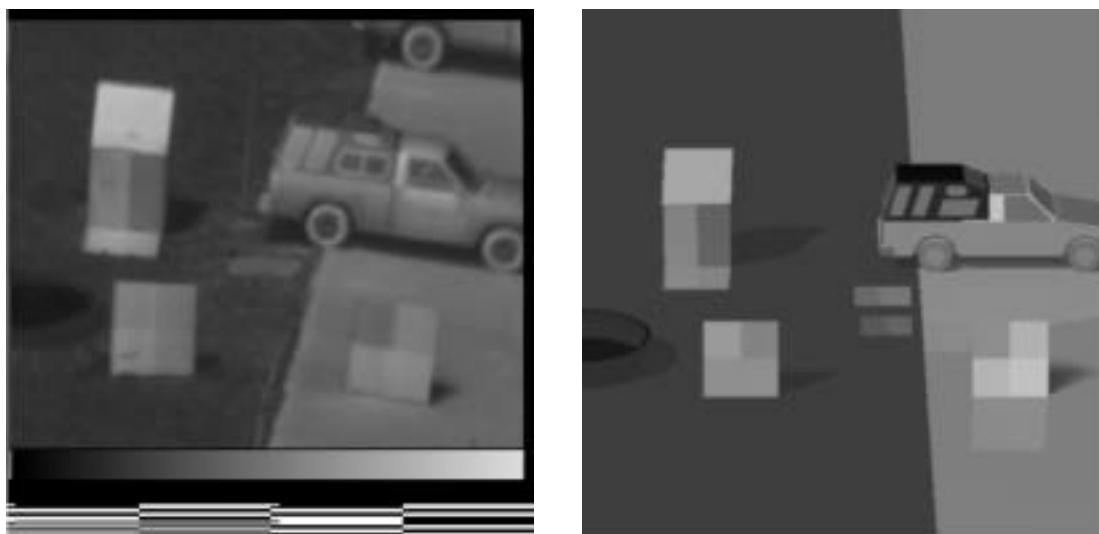


Figure 3-18

Side-by-side comparison of a longwave infrared image collected using an Inframetrics 600L with a predicted scene from the DIRSIG model (the image simulates an acquisition at 12 noon local time, on 6/23/92 at 43°05'00"N latitude and 77°40'00"W longitude).



Figure 3-19

Side-by-side comparison of a midwave infrared image collected using a Mitsubishi IR 5120A with a predicted scene from the DIRSIG model (the image simulates an acquisition at 8:00AM local time, on 6/23/92 at 43°05'00"N latitude and 77°40'00"W longitude).

Rankin, 1992, carried out a validation program to evaluate the performance of the THERM submodel as a stand-alone unit and the DIRSIG model as a whole. Also included in this evaluation was a sensitivity study which looked at the effects that individual components in the radiometry submodel had on the final predicted radiance. A brief description of the results from these studies are presented in the following sections. For further details, the reader is directed to the aforementioned document.

3.1 Validation of the THERM submodel

The main objectives of the THERM submodel validation were to determine the accuracy of THERM's prediction of object temperatures and to identify the input variables which have the largest impact on this prediction. In the validation procedure, THERM was run in a stand-alone mode outside of DIRSIG. Input to the model included temporal histories of air temperature, pressure, relative humidity, wind speed, direct and diffuse solar insolation, sky exposure, cloud type and precipitation information. Table 3.1-1 lists the input variables and the sources from which they are obtained. Model output consists of a time-based vector of temperatures for a particular object under study. These output temperatures were compared to a set of actual measurements collected from a fully instrumented experiment. All the meteorological and radiometric inputs were monitored for a 48-hour period, on 15-minute intervals, using a collection of thermistors, pyrometers, and other meteorological monitoring equipment. Longwave and midwave infrared imagery of the instrumented test scene was collected on half-hour intervals throughout this experiment to facilitate final scene validation studies (to be discussed later).

Eleven materials were used in the validation process, including: brick, soil, asphalt, gravel, water, glass, steel, plywood, hardwood, sand and grass. The physical and thermodynamic properties were either measured (when possible) or taken from the thermodynamic literature including the THERM documentation (DCS Corporation, 1990). Appendix D lists these parameters for the materials used in this study.

The results presented are taken from an experiment conducted on 22-23 June 1992. The test scene is depicted in Figure 3.1-1. Imagery was collected using an Inframetrics 600L

Table 3.1-1 List of THERM's input variables and their sources.

Meteorological Parameters	Source of Parameter	Thermodynamic Parameters	Source of Parameter
Air Temperature	Thermometer	Density	Available Literature
Air Pressure	Barometer	Specific Heat	Available Literature
Relative Humidity	Hygrometer	Thermal Conductivity	Available Literature
Dew Point	*	Exposed Area	Experimental Estimate
Wind Speed	Anemometer	Visible Emissivity	Available Literature
Direct Insolation	Pyronometer**	Thermal Emissivity	Measurement
Diffuse Insolation	Pyronometer**	Self-Generated Power	Available Literature
Sky Exposure	Experimental Estimate	Thickness	Measurement
Cloud Type	Experimental Estimate	Slope	Measurement
Rain Type	Experimental Estimate	Azimuth	Measurement
Rain Rate	Rain Gauge	Sun/Shadow History	Visible Imagery
Rain Temperature	Experimental Estimate		

* Thermal model computes dew point based on air temperature and relative humidity

** Eppley Precision Pyronometers

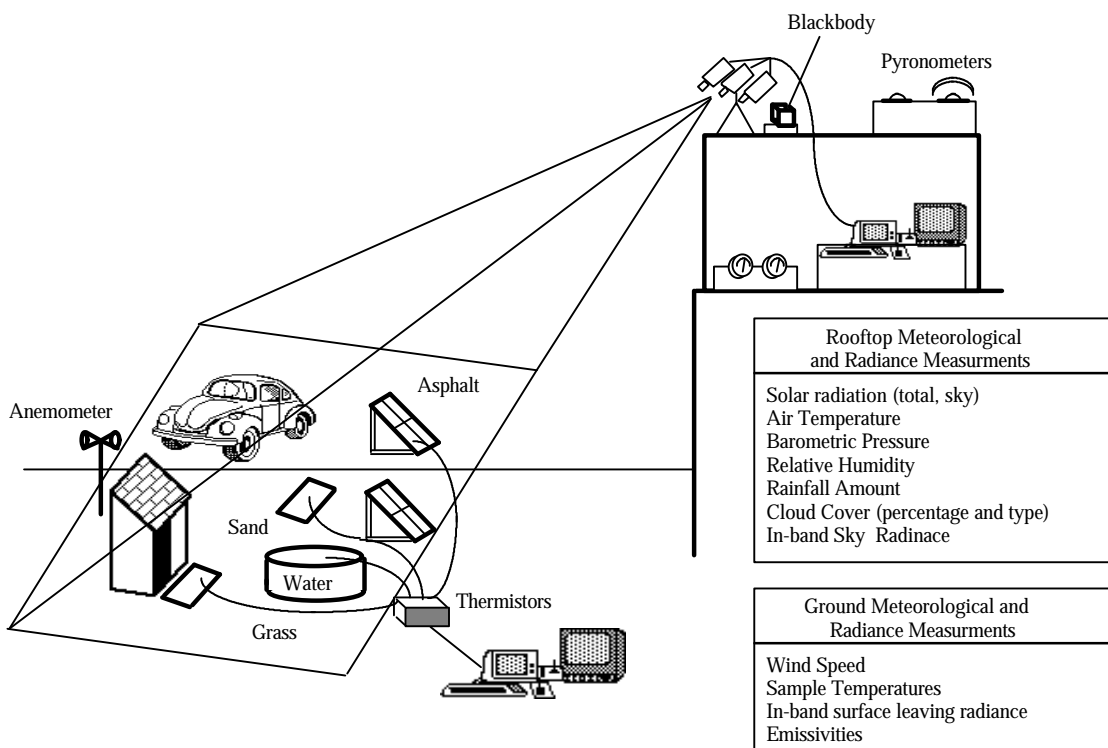


Figure 3.1-1

Rooftop collection experimental scene design carried out on 22-23 June 1992.

camera for the longwave infrared (10 to 12.5 μm) and a Mitsubishi IR 5120A camera for the midwave infrared data (3 to 5 μm) (Fujino *et al.*, 1989).

As mentioned previously, temperatures of the eleven scene elements used for this study were measured using a set of calibrated thermistors. In order to provide some credence to the temperature measurements taken, a simple comparison between the recorded temperatures and the apparent temperatures derived from the longwave infrared imagery were plotted. Figure 3.1-2 shows this comparison for asphalt. The close match between the curves provided us with the confidence to proceed with the validation procedure. The slight positive bias present in the apparent temperature data derived from the imagery was most likely due to the additive effects of path and reflected downwelled radiance.

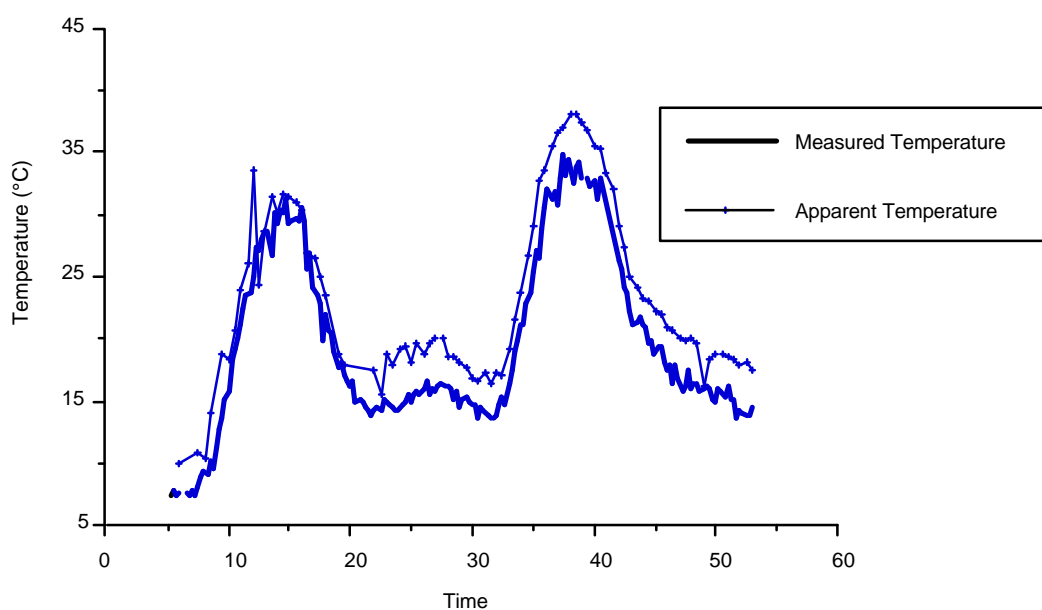


Figure 3.1-2 LWIR image derived temperatures vs. thermistor measurements for asphalt, 22-23 June 1992.

3.1.1 Weather parameters

The variability for each of the weather parameters listed in Table 3.1-1 was determined from the literature supplied by the manufacturer of the measurement equipment or estimated by the experimenter. In order to determine THERM's sensitivity to variability in meteorological data, a limited Monte Carlo experiment was carried out where the input variables were varied one at a time by adding a random fluctuation bounded by the error values for that variable to each of the time-based weather parameters. This modified weather history was then input to THERM and the resulting temperature prediction recorded. This was repeated 10 times for each of the weather parameters. A root-mean-squared (rms) error was then computed over time between the measured and predicted values resulting from the modification of the individual parameters. Table 3.1.1-1 lists the measurement errors and the resulting rms temperature values resulting from this study. The values listed in this table are averages over the 11 objects studied.

Table 3.1.1-1 Weather parameter errors and resulting temperature errors.

Meteorological Parameter	Measurement Error	RMSE Temperature (°C)
Air Temperature (°C)	0.2	0.1027
Air Pressure (mbar)	0.2	0.0017
Relative Humidity (%)	0.2	0.0069
Wind Speed (m/sec)	1.111	0.2978
Direct Insolation (L/hr)	0.043	0.0061
Diffuse Insolation (L/hr)	0.043	0.0046
Sky Exposure	0.05	0.0728
Cloud Type (#)	CT=0,1,7,8	0.0518
RSS Error	-	0.3276

Clearly the most influential meteorological parameters are air temperature and wind speed. Slight modifications in air temperature will modify the temperature of objects in the scene such that they approach this ambient surrounding value. Therefore accurate measurement and specification of air temperature is required for accurate object temperature prediction. Wind speed also proved to be a significant factor. The motion of air over the surface of an object enhances heat transfer rates between the air and the object. This rate is a function of the wind speed. It is therefore critical to predict as closely as possible the prevailing wind conditions. This is not always easy to accomplish since wind speed has such a short time constant. If one uses point readings from an anemometer (as was done in this study) very large errors are likely.

3.1.2 Object parameters

An identical approach was taken to assess the sensitivity of THERM's temperature prediction to the specified material thermodynamic properties. The objects listed in the previous section were chosen to represent materials with varying thermal inertia characteristics. The measurement errors for these parameters are not well documented in the literature (if at all) so a conservative estimate of 10% error was used for those parameters for which an actual value could not be obtained. Table 3.1.2-1 lists the measurement errors and the associated prediction errors for each parameter.

Table 3.1.2-1 Material parameter errors and resulting temperature errors.

Thermodynamic Parameter	Measurement Error	RMSE Temperature (°C)
Specific Heat (L/cm/°C)	10%	0.0718
Density (kg/m ³)	10%	0.0720
Thermal Conductivity (L-cm/hr/°C)	10%	0.0477
Thickness (cm)	0.1	0.0363
Visible Emissivity	10%	0.3934
Thermal Emissivity	0.025 (~5%)	0.0624
Self-Generated Power (L)	10%	0.0236
Exposed Area	10%	0.2809
Slope	3°	0.0456
Azimuth	3°	0.1012
RSS Error (Passive Object)	-	0.5137
RSS Error (Active Object)	-	0.5142

From Table 3.1.2-1 it can be seen that the visible emissivity, exposed area and azimuth are the most significant contributors to the error in temperature prediction. The overall error resulting from the incorrect specification of material parameters is potentially more critical than that resulting from incorrect meteorological parameter specification.

Visible emissivity (or absorption) determines what fraction of the incident direct and diffuse solar insolation are absorbed by the object. This parameter determines the amount of heat loading received by the material. Errors in this parameter are intuitively important since everyone knows that is more painful to walk across an asphalt driveway at 2:00PM on a sunny summer day than it is to walk across a concrete driveway under the same conditions. This is due primarily to the

visible emissivity (reflectance) differences between the materials.

Azimuth specifies the angular orientation of the object with respect to the sun. The amount of energy absorbed by a surface is proportional to the cosine of the angle between the surface normal and the direction of incoming radiation. Errors in this parameter will affect the solar load that is given to the material and impact the temperature prediction.

Exposed area, as defined in the documentation accompanying THERM, is best described as a “fudge factor”. This parameters attempts to define how much of the object's surface area is exposed to the surrounding environment. For instance a slab of concrete will have a value of 0.5 (the maximum value) while a grass field will have a value of 0.16. Since many surfaces of the individual grass blades see each other, rather than the surrounding environment, this value is lower. Hard to measure, this value is typically estimated by the user.

Between both the weather and material parameters sensitivity studies, THERM can be said to have a prediction error sensitivity to the supplied parameters of approximately 0.6°C. Since the goal of DIRSIG is to produce accurate absolute temperatures for objects within a scene, THERM prove to be a good choice.

Finally, Table 3.1.2-2 lists the temperature errors obtained between the thermistor measurements and the THERM predicted values for each of the 11 materials in the scene over the 24-hour period. The original meteorological and thermodynamic parameters were used to simulate these results.

Table 3.1.2-2 Root mean-square errors between actual thermistor measurements and THERM prediction of temperature for the 22-23 June 1992 data set.

Material	RMSE Temperature (°C)
Aluminum	1.23
Asphalt	2.31
Brick	1.78
Car Roof (white)	1.63
Car Side (white)	2.91
Car Window	2.49
Concrete Panel	1.04
Roof Gravel	1.36
Sand	1.14
Tire	3.36
Water	1.05
Windshield	2.27
Wood Panel	1.23
Average Error	1.83

A 1.83°C error in temperature prediction is expected in magnitude. Many limitations exist in the THERM model. Included are the sensitivity to the accurate specification of weather and material parameters which were illustrated above. The materials used in the actual experiment obviously will not have exactly the same value for material parameters that were obtained from the literature. Therefore, errors greater than those predicted from the sensitivity study are expected. THERM treats each object as isolated within the described environment. The influence of surrounding objects on the temperature of the object it is predicting is unaccounted for. In spite of these limitations, THERM performs well for the relatively fast execution time. More exotic models (e.g. finite element analysis models) may provide better results, however, the computational expense is intolerable for this application. Future generations of the DIRSIG code will want to examine alternative models which might provide more accurate results.

3.2 Validation of radiometric and thermal performance of DIRSIG

The radiometric equations given in 2.4-1 through 2.4-3 represent the method of radiance prediction in the DIRSIG code. Rankin, 1992, has performed a validation study on these propagation equations from which the results will be summarized. First, the relative sensitivity of the total radiance reaching the sensor with respect to each variable was determined in both the

midwave infrared (MWIR) and longwave infrared (LWIR) bandpasses, 3-5 μm and 8-14 μm , respectively. Second, the absolute radiometric error was determined by comparing final synthetic images produced by DIRSIG with truth images. Root mean-square radiance errors were computed for each object in the scene over a twenty-four hour period, and for each hour in the day for all the objects in the scene. The reader is again referred to the aforementioned document for greater detail concerning this study.

3.2.1 Radiometry sensitivity

In order to look at the sensitivity of the radiometric predictions of the DIRSIG code, a standard error propagation technique was employed for independent and correlated variables (Beers, 1957). The error in total radiance computed using two variables is given by

$$s_L = \sqrt{\left(\frac{dL}{dx}\right)^2 s_x^2 + \left(\frac{dL}{dy}\right)^2 s_y^2 + 2 r_{xy} \left(\frac{dL}{dx}\right) \left(\frac{dL}{dy}\right) s_x s_y} \quad 3.2.1-1$$

where $\delta L/\delta x$ is the partial derivative of the radiance, L , with respect to one of the variables in the radiometric equation, x , and σ_x is the error associated with that variable. For correlated variables the partial derivative with respect to the correlated variable, y , is also included with the error in that variable along with the correlation coefficient between the two dependent parameters, ρ_{xy} .

Table 3.2.1-1 summarizes the errors associated with the individual radiometric parameters in Equations 2.4-1 to 2.4-3. When the error is expressed as a percentage, this represents an error whose size is some percentage of the magnitude of the actual parameter. These errors are used to determine the relative contributions of each of these parameters to the overall error in radiance computed with Equation 3.2.1-1. These results are presented in Table 3.2.1-2 for the longwave infrared region and Table 3.2.1-3 for the midwave infrared region.

Table 3.2.1-1 Error associated with the individual parameters in the radiometric equations for the longwave and midwave infrared bandpass regions.

Radiometric Parameter	σ_{LWIR}	σ_{MWIR}
ϵ, ϵ_B	0.025	0.025
L_T, L_B, L_{TAB}	0.2%	0.5%
F	10%	10%
$E_S \tau_1 \cos(\theta)$	-	0.2%
L_D	2%	2%
L_u	2%	2%
τ_2	3.2%	8.5%
θ_S, θ_B	3°	3°

Table 3.2.1-2 Error contribution in $\text{W/m}^2\text{sr}$ to the total radiance for the longwave infrared of each of the parameters in the radiometric equation. The total error in radiance is also converted to apparent temperature.

Radiometric Parameter	Diffuse Hit	Specular hit (bounce to sky)	Specular hit (bounce to background)
ϵ	0.70	0.57	0.31
L_T	0.08	0.06	0.08
F	0.38	-	-
L_D	0.03	0.07	-
L_u	0.02	0.02	0.02
τ_2	1.00	0.75	1.22
ϵ_B	-	-	0.11
L_{TB}	-	-	0.01
L	1.28	0.95	1.26
L (in apparent temperature)	1.92°C	1.43°C	1.89°C

Table 3.2.1-3 Error contribution in W/m^2sr to the total radiance for the midwave infrared of each of the parameters in the radiometric equation. The total error in radiance is also converted to apparent temperature.

Radiometric Parameter	Diffuse Hit	Specular hit (bounce to sky)	Specular hit (bounce to background)
ε	0.013	0.017	0.057
L_T	0.008	0.005	0.025
F	0.001	-	-
L_D	0.000	0.007	-
L_u	0.011	0.010	0.010
τ_2	0.141	0.138	0.438
ε_B	0.000	-	0.001
L_{TB}	0.000	-	0.001
$E_S\tau_1/\pi$	0.000	0.000	0.000
θ_S	0.001	0.015	0.004
θ_B	-	-	0.000
L	0.132	0.126	0.433
L (in apparent temperature)	1.71°C	1.67°C	2.59°C

In both the longwave and midwave bandpass regions, the primary contributor to the error is the transmission between the target and the sensor, τ_2 . In the above analysis, τ_2 and L_u were the only parameters treated as correlated and any attempt to change one will affect the other's magnitude. These parameters are both a direct output from the MODTRAN code. The specification of the atmospheric profiles and the choice of aerosol scattering models will have a marked effect on the prediction of these parameters. This illustrates the necessity for a proper description of the air column composition above the scene.

Also significant are the emissivity for the target and the shape factor (in the diffuse case). Emissivity affects how much energy produced by a target is released toward the sensor as well as how much external incident energy is reflected up to the sensor from the target. The importance of proper specification of this parameter is evident and measurements of this value are easily made in the laboratory. The affect of shape factor, F , is also important in the diffuse case. When objects in a scene are near large vertical obstructions, the percentage of skylight falling on these objects (and subsequently reflected) is affected by the magnitude of the shape factor. This parameter also determines indirectly the amount of background energy from adjacent scene elements which falls onto the target. Although not separated out specifically, it is

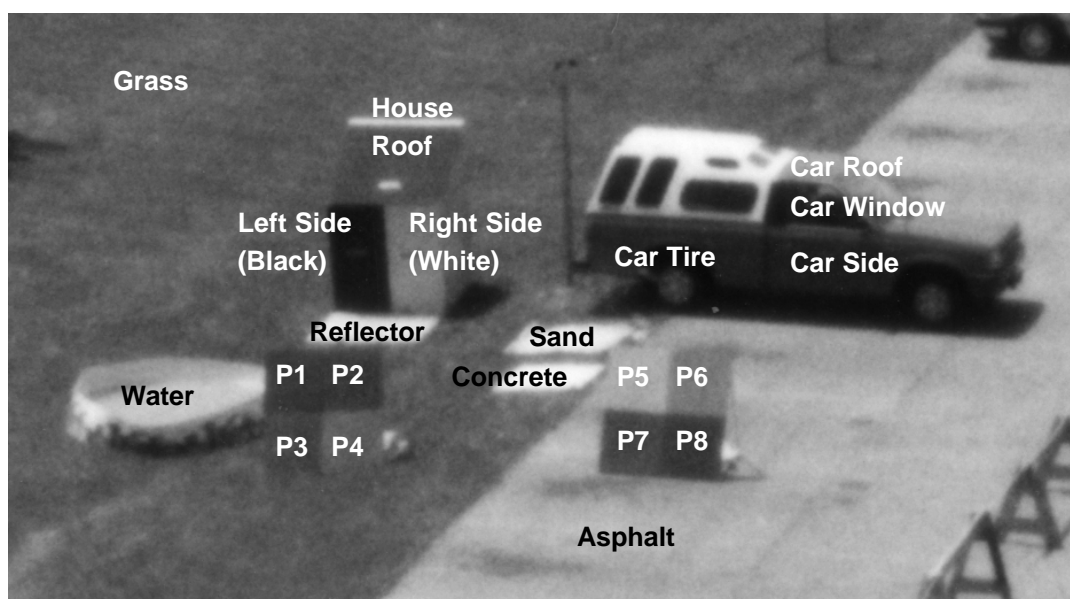
believed that the latter situation is of primary importance.

3.2.2 DIRSIG final scene validation

As a final stage of the validation study, Rankin, 1992, compared the images actually acquired during the experiment to DIRSIG generated images produced using all the recorded meteorological and material data. Radiance values were sampled from selected targets and compared to samples taken at the same locations on the DIRSIG generated images. This was done for 24 images collected over a 24-hour period with the longwave and midwave infrared cameras. A photograph of the validation scene is shown in Figure 3.2.2-1 with the sample areas labeled.

In order to facilitate the conversion from digital count to radiance, the sensors were calibrated using a blackbody. Calibration involved imaging a blackbody at two different temperatures which would span the range encountered in the actual scene (10°C and 40°C were chosen). These values were collected before and after every image acquisition so that each image could be calibrated individually without concern about sensor drift or gain fluctuations and to allow sensor setting to be modified to obtain suitable dynamic range for all images. Figure 3.2.2-2 and 3.2.2-3 illustrate the digital count values recorded using each sensor for the two blackbody setting.

Figure 3.2.2-4 compares DIRSIG predicted and measured radiance for three different materials over the 24-hour time period for longwave infrared sensor. In addition, an rms radiance error was determined for each object in the scene for the 24-hour period. In order to directly compare the midwave and longwave radiance errors, the error values were converted to percent rms radiance error by dividing the rms value by the average measured radiance over the 24-hour period. Figure 3.2.2-5 shows these errors for each of the samples in the scene. The rms error was also converted to an rms apparent temperature error using Planck's equation to gain a better physical intuition of DIRSIG's performance. Figure 3.2.2-6 shows these temperature errors. The average rms apparent temperature error is approximately 5°C in the longwave and 6°C in the midwave regions.



P1: Red

P2: Green

P3: Medium Gray

P4: Light Blue

P5: Very Light Gray

P6: Light Gray

P7: Dark Gray

P8: Very Dark Gray

Figure 3.2.2-1

Photograph of validation scene taken from rooftop of RIT's Center for Imaging Science and enlarged. Objects used for validation analysis are labeled.

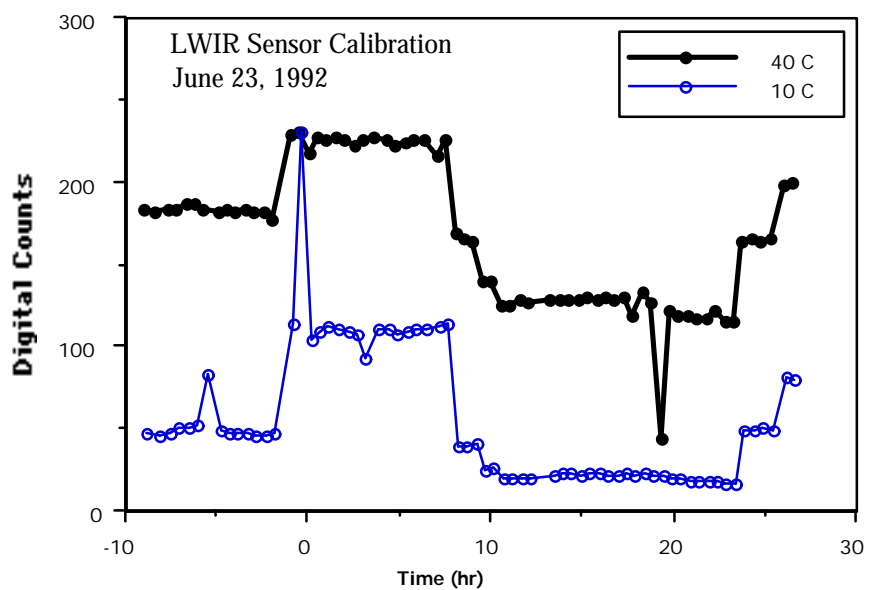


Figure 3.2.2-2 LWIR sensor blackbody calibration data.

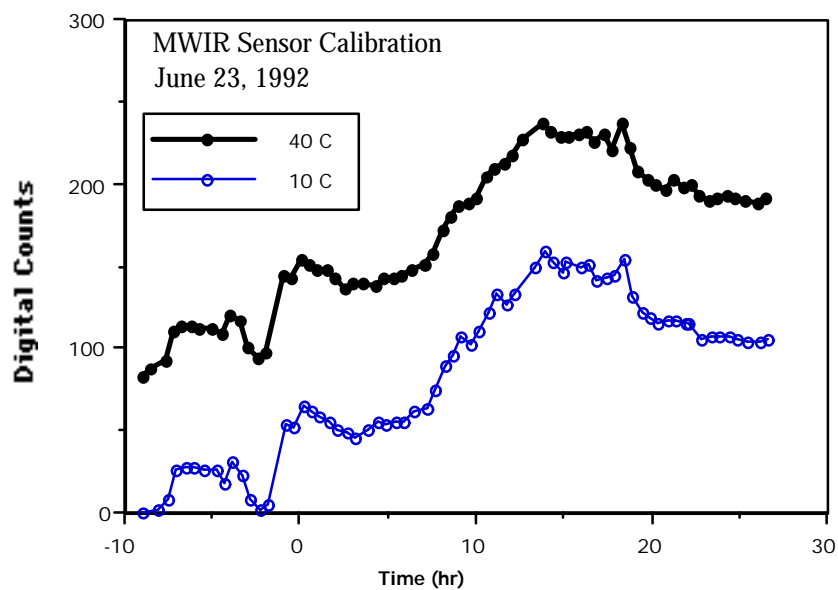


Figure 3.2.2-3 MWIR sensor blackbody calibration data.

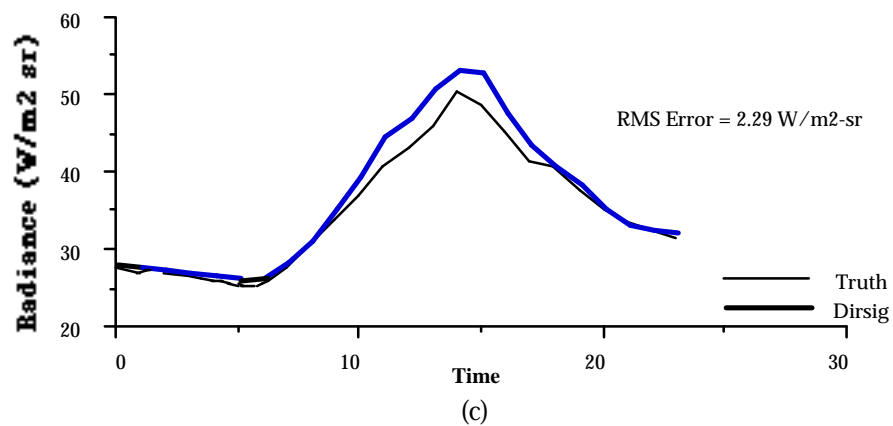
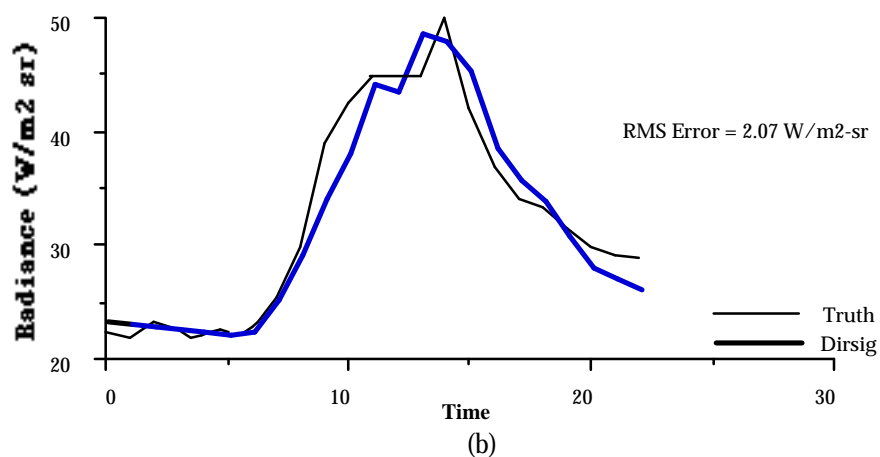
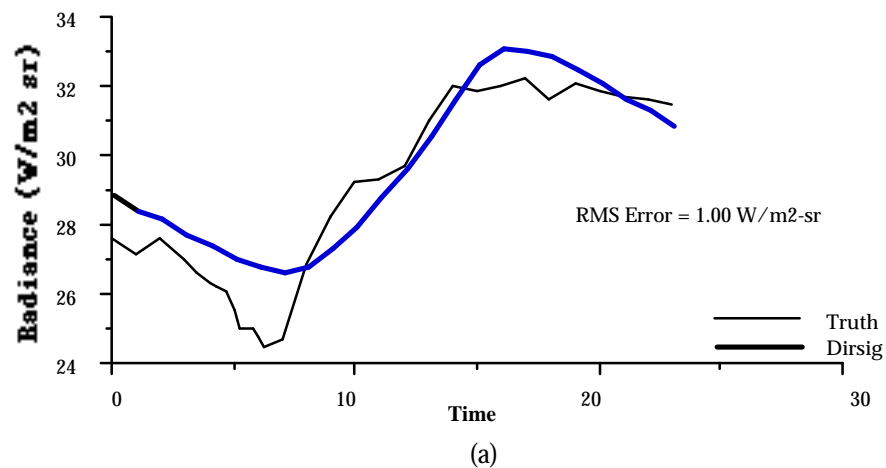


Figure 3.2.2-4 DIRSIG predicted versus measured LWIR radiance for (a) water, (b) the car roof, and (c) asphalt.

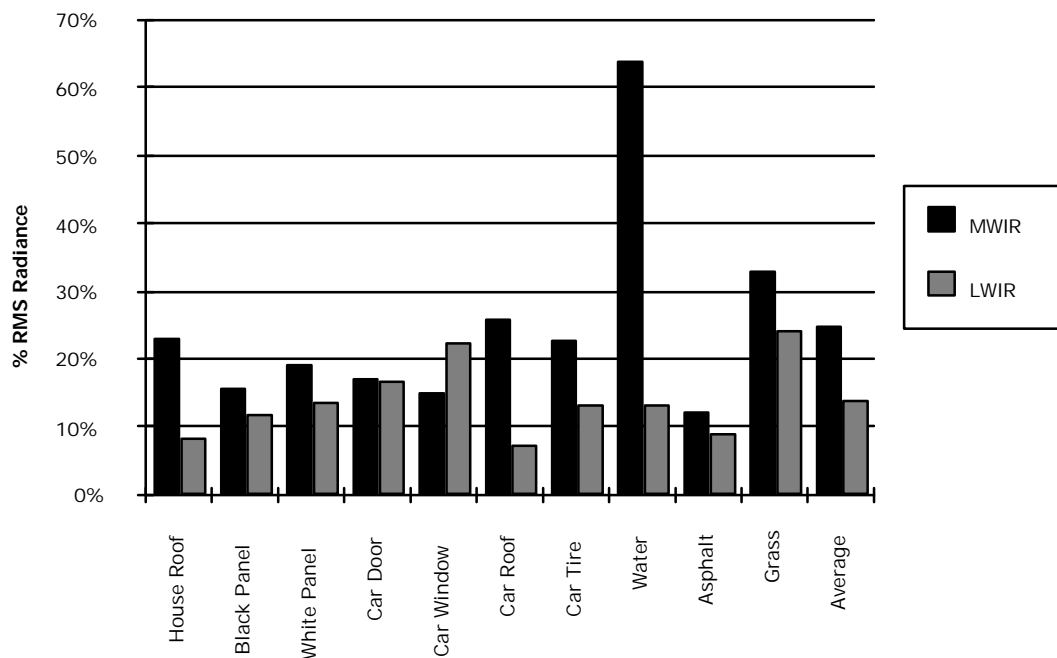


Figure 3.2.2-5 Root mean-square radiance error as a percent of average radiance over the 24-hour collection period.

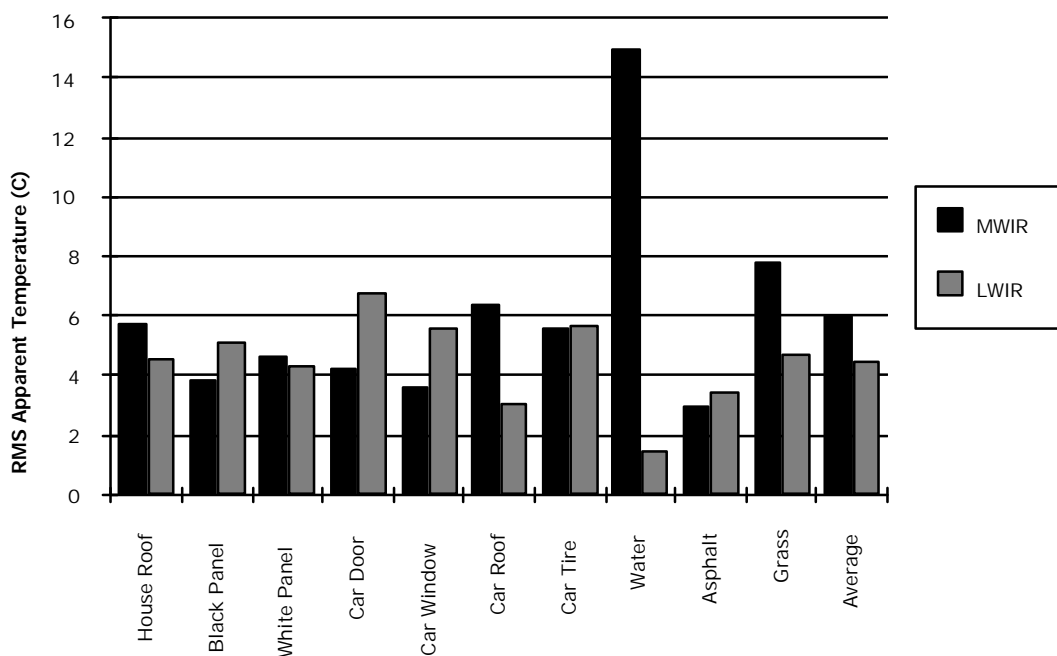


Figure 3.2.2-6 Root mean-square apparent temperature error over the 24-hour collection period.

One thing that stands out in Figure 3.2.2-6 is that while the rms apparent temperature error for the water target is lowest in the longwave bandpass, it is the highest in the midwave region. A plot of measured and DIRSIG predicted radiance for water in the midwave bandpass is shown in Figure 3.2.2-7. This figure shows that the major contribution of error in the DIRSIG predicted radiance occurs during the sunlit hours. This implies that the over prediction of radiance by the DIRSIG model may have its origin in two related phenomena both stemming from an error in emissivity. In the midwave region at the incident angle present in this scene, water has an emissivity of about 0.70 (see Appendix C). If this value is too low (and as a result the reflectivity is too high) there would be an over prediction of reflected sky radiance and an under prediction of emitted radiance. Since the error is a maximum in the daytime hours, this seems a viable explanation.

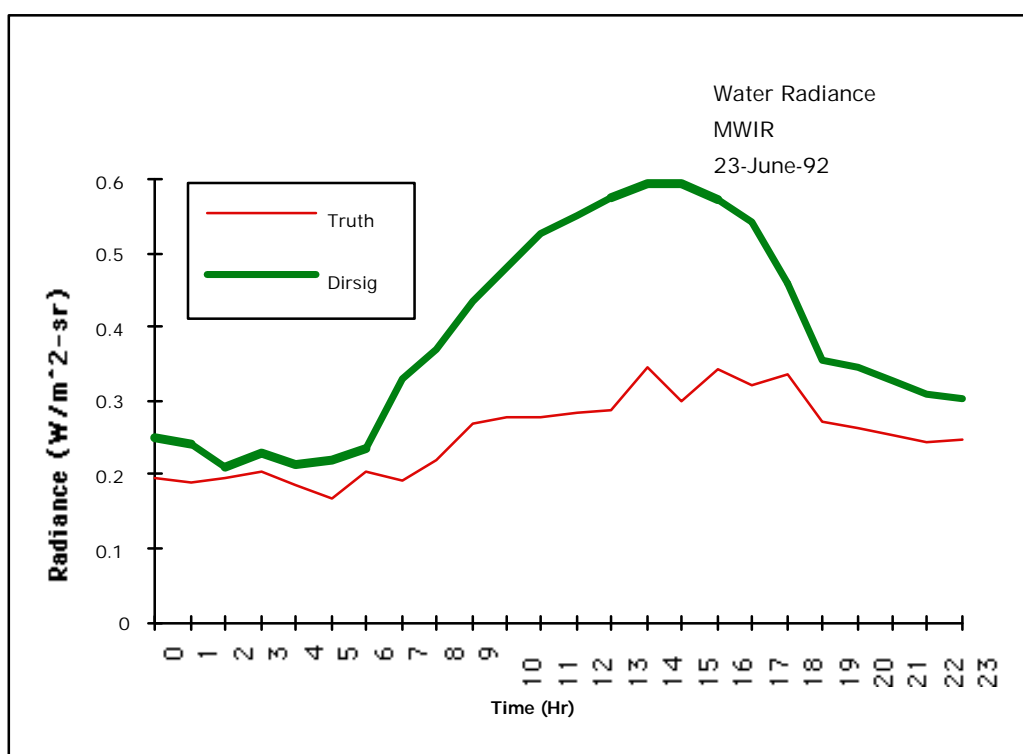


Figure 3.2.2-7 Truth vs. DIRSIG radiance values for water in the MWIR bandpass for June 23, 1992.

This validation study provided positive results. In addition to producing realistic looking scenes, these generated images exhibit radiometric accuracy in apparent temperature to within 5°C in the longwave and 6°C in the midwave regions. More importantly, however, the validation has

shown what areas of DIRSIG are weak and warrant further development. Future plans exist to put clouds directly into DIRSIG scenes so that more accurate thermal and radiance computations could be carried out spatially in the model as opposed to MODTRAN's and THERM's blanket treatment of clouds. A more rigorous study of object emissivity including the treatment of bi-directional reflectance distributions (BDRF) could lead to better reflectance treatment in the scene. Improvements to the existing thermal model are warranted which could include the effects of neighboring facets on the current facets temperature.

4.0 CONCLUSIONS AND RECOMMENDATIONS

The DIRSIG model developed for this dissertation is a rigorous simulation of the physics governing the image formation process. Based on the first-principles concepts which dictate the interactions between the target materials, incident and emitted radiation, atmospheric attenuation and additive effects, this model produces a realistic radiance field which would be expected at the front end of an airborne or space-based system. Unlike many other models, DIRSIG has been thoroughly tested against a validation study in the thermal and midwave infrared portions of the spectra. Qualitative results have also been presented in the visible wavelength regions. This section will summarize the quantitative validation results as well as list the suggested future enhancements needed to better model the imaging chain.

This effort has shown that the DIRSIG model yields a realistic radiance scene at the front end of the sensor. The validation effort demonstrated good initial correlation between predicted and observed image radiance values. Against the validation scene used in this research, an error in apparent temperature of 5°C was obtained in the longwave and 6°C in the midwave infrared portions of the spectrum was attained. In light of the amount of information necessary to describe the materials in the scene, the prevailing meteorological conditions, and composition of the atmosphere, these results appear quite good. In addition, the sensitivity analysis portion of the validation effort provided much needed insights into what aspects of the end-to-end modeling process were weakest and where future efforts would have the highest payoff. Regrettably, there is no other end-to-end validation data on any of the competing SIG models so it is difficult to place these results in perspective. On an absolute scale the observed errors are acceptable for most training and many exploitation and automated target recognition (ATR) applications. However, for detailed reverse engineering studies, where absolute radiometric answers would be required, the errors would need to be reduced by 25 to 50%. This seems like a reasonable near-term goal based on the sensitivity analysis performed on this effort.

The best part about developing a model such as this and performing periodic validations and sensitivity studies, is the ever growing list of enhancements/fixes that become evident. At the time of this writing, the following topics are suggested as future areas in which improvements to the model need to occur:

- 1) Attention should be given to the addition of texture to the imagery. The current approach provides a uniform ground leaving radiance level across most of the facet's surface, modified only by shadowed areas or areas

differentially reflecting background radiance. Parametric approaches need to be determined to add correlated pixel-to-pixel texture.

- 2) Objects need to be treated in a manner more closely affiliated with full BRDF. Currently targets are either totally specular or diffuse which produces some unrealistic effects in the imagery, especially in the reflected wavelength region. A weighting of specularity/diffuseness may be an appropriate approximation and should be investigated.
- 3) In order to use the DIRSIG model to produce multispectral imagery that is appropriate for testing classification/segmentation algorithms, spectral correlation between bands for particular classes of materials needs to be imposed on the spectral signatures used for the current targets.
- 4) Enhancements which lead to a shorter run-time are always needed. Most of the time is currently consumed by the ray tracer where no attention has been paid to speed issues.
- 5) Enhancements need to be made to the thermal submodel to allow lateral conduction which would allow heat to be transferred across the surface of an object. The currently implemented version utilizes the model THERM which treats facets as thermally isolated and independent, which causes artifacts to exist in the final imagery in the form of very sharp delineations between temperatures. A new thermal submodel needs to be used or some sort of post-processing technique implemented.
- 6) A time-dependent self-generated power attribute should be attached to each facet so that these sources of power can be cycled on and off during the scene generation process.
- 7) The choice of AutoCAD as a scene construction tool was made based on availability and support across multiple platforms. A means of incorporating data from other CAD packages needs to be developed to take advantage of the large number of existing targets that have already been created. BRLCAD is an example that is used throughout the defense community.
- 8) Incorporate higher spectral resolution atmospheric propagation models for signature studies. LOWTRAN (20 cm^{-1}) and MODTRAN (2 cm^{-1}) offer good spectral resolution in the reflective portion of the spectrum, however, the resolution is rather coarse in the LWIR. A model with high resolution in the LWIR should be incorporated to allow analysis of longwave infrared signatures. A model of this sort is currently under development at NASA's Jet Propulsion Laboratory.
- 9) Incorporate a sensor model to propagate the radiance field reaching the sensor through the sensing system to produce a final image. This model should incorporate optical and electronic transfer functions as well as add the appropriate noise on top of the image signal.
- 10) Finally, it is believed that this effort has demonstrated that DIRSIG has matured to the point where future enhancements should include efforts to package the code for more general use. These enhancements will make what is currently engineering evaluation software much more useful in an operational environment.

5.0 REFERENCES

- Autodesk Inc., *AutoCAD Release 10 Reference Manual*, 1989.
- Beers, Y., *Introduction to the Theory of Errors*, Addison-Wesley Publishing Company, Inc., Reading, MA, 1957.
- Berk, A., L.S. Bernstein and D.C. Robertson, "MODTRAN: A moderate resolution model for LOWTRAN 7," GL-TR-89-0122, Spectral Sciences Inc., April, 1989.
- Biesel, H. and T. Rohlfing, "Real-time simulated forward looking infrared (FLIR) imagery for training," *Proceedings of the SPIE, Infrared Image Processing and Enhancement*, Vol. 781, 1987.
- Botkin, E., "Infrared modeling and analyses (IRMA)," AFATL-TR-81-65, Grumman Aerospace Corporation, Bethpage, NY, 1981.
- Byrnes, A.E. and J.R. Schott, "Correction of thermal imagery for atmospheric effects using aircraft measurements and atmospheric modeling techniques," *Applied Optics*, Vol. 25, No. 15, 1986.
- Cathcart, J.M. and A.D. Sheffer, "Target and background infrared signature modeling for complex synthetic scenes," *Proceedings of the SPIE, Infrared Systems and Components II*, Vol. 890, 1988.
- Clough, S.A., F.X. Kneizys, E.P. Shettle and G.P. Anderson, "Atmospheric radiance/transmission: FASCOD2," *Proceedings of the Sixth Annual Conference of Atmospheric Radiation*, Williamsburg, VA, 1986.
- DCS Corporation, "AIRSIM thermal signature and prediction analysis tool definition and analysis of object inputs," DCS Technical Note 9090-002-004, DCS Corporation, December, 1990.
- DCS Corporation and J.R. Schott, "Automatic Target recognition/counter-countermeasures technology development program model review," DCS Report No. 13430LT003Z, DCS Corporation, 1987.
- Dunn, A.R., G. Lindquist and J.R. Meyer, "High resolution of IR scene model," *Proceedings of the SPIE, Infrared Image Processing and Enhancement*, Vol. 781, 1987.
- Feng, X., "Comparison of methods for generation of absolute reflectance factor measurements for BRDF studies," M.S. Thesis, Rochester Institute of Technology, Center for Imaging Science, 1990.
- Fujino, S., T. Miyoshi, M. Yokoh and T. Kitahara, "Mitsubishi thermal imager using the 512x512 PtSi focal plane array," *Proceedings of the SPIE, Infrared Technology*, Vol. 1157, San Diego, CA, 1989.
- Gardner, G.Y., J. Mendelsohn, J. Kim and W. Reynolds, "A digital scene model for simulation of visual and infrared imagery," *Proceedings of the SPIE, Infrared Image Processing and Enhancement*, Vol. 781, 1987.
- Haines, E., "Introduction to ray tracing," *14th Annual Conference of Computer Graphics and Interactive Techniques*, SIGGRAPH '87, Anaheim, CA, 1987.

- Kneizys, F.X., E.P. Shettle, L.W. Abreu, J.H. Chetwynd, G.P. Anderson, W.O. Gallery, J.E.A. Selby and S.A. Clough, "Users Guide to LOWTRAN7," AFGL-TR-88-0177, Environmental Research Papers, No. 1010, Air Force Geophysics Laboratory, Optical/Infrared Technology Division, Hanscom AFB, MD, December, 1988.
- Kornfeld, G.H., "Digital simulation of precise sensor degradations including non-linearities and shift variance," *Proceedings of the SPIE, Infrared Image Processing and Enhancement*, Vol. 781, 1987.
- Lillesand, T.M. and R.W. Kiefer, *Remote Sensing and Image Interpretation*, 2nd edition, Wiley, 1987.
- Rankin, D.K., "Validation of DIRSIG, an infrared synthetic scene generation model," M.S. Thesis, Rochester Institute of Technology, Center for Imaging Science, 1992.
- Salvaggio, C., G.J. Braun and J.R. Schott, "SVGSM: A spectral vector generating model using LOWTRAN 7 and SCATRAN atmospheric propagation codes," RIT/DIRS 90/91-63-141, Rochester Institute of Technology, January, 1991.
- Schott, J.R., "Incorporation of angular emissivity effects in longwave infrared image models," *Proceedings of the SPIE Symposium, Infrared Technology XII*, Vol. 685, San Diego, CA, 1986.
- Schott, J.R., M. Fairchild, X. Feng, R. Raqueno, B. Brower and T. Gallagher, "Techniques for measurement of the optical properties of materials," RIT/DIRS 89/90-51-134, Rochester Institute of Technology, January, 1990.
- Schott, J.R. and C. Salvaggio, "Inclusion of sensor noise in radiometric models for generation of synthetic longwave infrared images," *Proceedings of the SPIE, Three-Dimensional Imaging and Remote Sensing*, San Diego, CA, 1987.
- Schott, J.R. and C. Salvaggio, "LWIR radiometric modeling for use with synthetic scene generation 1987/88 results," RIT/DIRS 87/88-51-122, Rochester Institute of Technology, January, 1989.
- Schott, J.R. and E.W. Schimminger, "Data use investigations for applications explorer mission A (Earth Capacity Mapping Mission)," Calspan Report No. 6175-M-1, NASA Accession #E81-10079, Calspan, January, 1981.
- Schott, J.R. and W.J. Volchok, "Thematic mapper thermal infrared calibration," *Photogrammetric Engineering and Remote Sensing*, Vol. 51, No. 9, 1985.
- Schwartz, I.B., K.A. Snail and J.R. Schott, "Infrared halo effects around ships," Memorandum 5529, Naval Research Laboratory, 1985.
- Sheffer, A.D. and J.M. Cathcart, "Computer generated IR imagery: a first principles modeling approach," *Proceedings of the SPIE*, Vol. 933, 1988.
- Shor, E.H., "3-D longwave infrared synthetic scene simulation," M.S. Thesis, Rochester Institute of Technology, Center for Imaging Science, 1990.
- Shor, E.H., C. Salvaggio and J.R. Schott, "Three-dimensional longwave infrared (LWIR) synthetic image generation incorporating angular emissivity effects using raytracing techniques," *SPIE 35th Annual International Symposium on Optical & Optoelectronic Applied Science and Engineering*, San Diego, CA, 1990.

- Spector, D.N., P.F. Lambeck, S.L. Sheller, S.C. Sawtell, D.K. Rankin and J.R. Schott, "Air Force infrared simulated image models," *Proceedings of the Infrared Information Symposia*, Vol. 35, 1991.
- Stets, J., J. Conant, J. Gruninger and B. Ryali, "Synthetic IR scene generation," *Proceeding of the SPIE, Infrared Systems and Components II*, Vol. 890, 1988.
- Warnick, J.S., E. Shor and J.R. Schott, "Thermal infrared scene simulation," RIT/DIRS 89/90-51-133, Rochester Institute of Technology, January, 1988.

APPENDIX A DIRSIG INPUT FILE FORMATS

There are many input files which must be configured in order to execute the DIRSIG code. The following pages contain examples of these files along with some description of their contents. These file must all be properly assembled in order to run the DIRSIG code properly and obtain physically meaningful simulation results.

These files consist of:

- 1) The *AutoCAD dview file* contains the viewing parameter information obtained from AutoCAD which describes the viewing geometry for the synthetic scene which is to be created. These parameters include the target point in a world coordinate system, the sensor position in a world coordinate system, the sensor orientation angles, the equivalent focal length for a 35mm camera, and the image pixel dimensions.
- 2) The *MODTRAN card deck file* contains the information specified in the MODTRAN users manual (Berk *et al.*, 1989) which describe the current applications atmospheric information.
- 3) The *geometric database file* which describe the 3-dimensional geometry which makes up the scene to be simulated. Described in terms of object, parts, and facets, each element of the scene (each facet) has attribute information describing the facet's material type, material code, default temperature, thickness, self-generated power, default shape factor, world coordinates for each facet vertex, facet normal vector, facet slope and azimuth with respect to the scene coordinate system.
- 4) The *radiance database file* is formed by the repeated runs of the MODTRAN atmospheric propagation model. This file contains scenario specific information such as the sensor altitude, minimum and maximum wavelength for the bandpass being simulated, the corresponding minimum and maximum frequency value and the frequency increment across the bandpass, the number of zenith angles at which actual data is computed with MODTRAN as well as the zenith angle increment used, the number of spectral points at which atmospheric parameters are defined across the bandpass, the exoatmospheric solar irradiance and the transmission from the source to the scene center for each sample center, the transmission, emitted and scattered path radiance from the scene center to the target as a function of zenith angle, integrated hemispheric sky radiance, sky radiance as a function of azimuth and zenith angle defined relative to the scene center, and a temperature profile of the atmosphere to space.
- 5) The *sensor response function file* defines the gain and offset to be applied to the radiance signal to convert it to digital count, and the relative sensor response function scaled between 1 and 0.
- 6) The *scene node file* which defines for the rest of the file scene specific parameters such as sensor altitude, minimum and maximum zenith angle over which atmospheric parameters are defined, minimum and maximum

frequency along with the frequency increment, month, day, year and time of the simulation, and the latitude and longitude of the scene center.

- 7) The *emissivity file* which defines a spectral emissivity curve from 39850 cm^{-1} to 350 cm^{-1} (approximately 0.25 to 20 μm) in 100 cm^{-1} increments, at each of 91 viewing angles (0 to 90°).
- 8) The *spectral extinction file* which defines the broad-band spectral extinction for 0.4 to 2.5 μm used to modify the solar insolation parameters in THERM and the spectral extinction coefficients for each frequency from 39850 cm^{-1} to 350 cm^{-1} in 100 cm^{-1} steps for all materials which exhibit transmissive properties (only clouds at the current time).
- 9) The *weather history file* which defines the following parameters as a function of time (down to 15 minute intervals) for the day being simulated; air temperature, air pressure, relative humidity, dew point, wind speed, direct insolation, diffuse insolation, sky exposure, cloud type, precipitation type, precipitation rate, and precipitation temperature.
- 10) The *materials database file* which defines for all possible materials of which facets can be made of in the scene the material name, material code, specific heat, thermal conductivity, density, specular flag, visible and thermal emissivity, exposed area and filenames for the materials emissivity and extinction coefficient data.

1) AutoCAD "dview" file (.adv)

User Specified

```

90.6849 119.9939 0.000
7162.3865 -6951.7077 10000.0
45.0 -45.0 0.0
3790.47023
512 512

```

2) MODTRAN card deck file (.cdk)

Program Output

```

F  2   3   2   1   0   0   0   0   0   0   0   0   1 300.000   1.00
   1   0   0   1   0   0   0.000   0.000   0.000   0.000   0.000
   0.000   0.000  90.000   0.000   0.000   0.000   0
   1   2  175   0
  39.773  84.109   0.000   0.000  17.000  360.000   0.000   0.000
  750    1250    100    2
   0

```

3) Geometric database file (.gdb)

Program Output

```

OBJECT
RUNWAY2_OBJ
1-0-0
PART
RUNWAY2_ATTS
1-1-0
FACE
RUNWAY2_RUNWAY_1
1-1-1
concrete/roadway
22
runway
-1
35.56
0
1.0
null
null
null
4
6.000000e+01 -3.000000e+01 -1.000000e+00
6.000000e+01 -6.000000e+01 -1.000000e+00
3.600000e+02 -6.000000e+01 -1.000000e+00
3.600000e+02 -3.000000e+01 -1.000000e+00
-0.00000000000000000000e+00 -0.00000000000000000000e+00 -8.999999999999999450000e+03
1.800000e+02
0.000000e+00
0.000000e+00
FACE
RUNWAY2_RUNWAY_2
1-1-2
concrete/roadway
22
runway
-1
35.56
0
1.0
null
null

```

```
null
4
6.000000e+01 -3.000000e+01 -5.000000e-01
6.000000e+01 -3.000000e+01 -1.000000e+00
3.600000e+02 -3.000000e+01 -1.000000e+00
3.600000e+02 -3.000000e+01 -5.000000e-01
-0.000000000000000000e+00 1.499999999999999940000e+02 -0.000000000000000000e+00
9.000000e+01
2.700000e+02
2.500000e-01
.
.
.
.
.
FACE
GRASS_4
24-1-4
summergrass
4
grass
-1
.91
-3.5
1.0
null
null
null
4
1.200000e+03 -8.500000e+02 -1.000000e+00
1.200000e+03 -8.500000e+02 -6.000000e+00
-1.300000e+03 -8.500000e+02 -6.000000e+00
-1.300000e+03 -8.500000e+02 -1.000000e+00
-0.000000000000000000e+00 -1.249999999999999960000e+04 -0.000000000000000000e+00
9.000000e+01
9.000000e+01
2.500000e-01
FACE
GRASS_5
24-1-5
summergrass
4
grass
-1
.91
-3.5
1.0
null
null
null
4
-1.300000e+03 -8.500000e+02 -1.000000e+00
-1.300000e+03 -8.500000e+02 -6.000000e+00
-1.300000e+03 2.150000e+03 -6.000000e+00
-1.300000e+03 2.150000e+03 -1.000000e+00
-1.499999999999999960000e+04 -0.000000000000000000e+00 -0.000000000000000000e+00
9.000000e+01
1.800000e+02
2.500000e-01
FACE
GRASS_6
24-1-6
summergrass
4
grass
-1
.91
-3.5
1.0
null
null
null
```

Program Output

112

```
4.244644e-04 1.888577e-08
6.339446e-04 1.547239e-09
0.000000 0.000000
5.640259e-04 3.054148e-08
2.682229e-04 1.725970e-07
3.587178e-04 5.711591e-08
2.350089e-04 8.457958e-08
3.196508e-04 3.774817e-08
5.941062e-04 3.755530e-09
0.000000 30.000000
5.640259e-04 3.054148e-08
2.682229e-04 1.725970e-07
3.587178e-04 5.711591e-08
2.350089e-04 8.457958e-08
3.196508e-04 3.774817e-08
5.941062e-04 3.755530e-09
0.000000 60.000000
5.640259e-04 3.054148e-08
2.682229e-04 1.725970e-07
3.587178e-04 5.711591e-08
2.350089e-04 8.457958e-08
3.196508e-04 3.774817e-08
5.941062e-04 3.755530e-09
.
.
.
90.000000 330.000000
7.817543e-04 9.089405e-09
8.279369e-04 2.169033e-07
8.600907e-04 7.488151e-08
8.496127e-04 1.125547e-07
8.146524e-04 3.458716e-08
7.261701e-04 2.290112e-09
90.000000 360.000000
7.817543e-04 9.447878e-09
8.279369e-04 2.216825e-07
8.600907e-04 7.631789e-08
8.496127e-04 1.144063e-07
8.146524e-04 3.539452e-08
7.261701e-04 2.378127e-09
33
0.000000 350.0
1.000000 350.0
2.000000 350.0
3.000000 350.0
4.000000 350.0
5.000000 350.0
6.000000 350.0
7.000000 350.0
8.000000 350.0
9.000000 350.0
10.000000 350.0
11.000000 350.0
12.000000 350.0
13.000000 350.0
14.000000 350.0
15.000000 350.0
16.000000 350.0
17.000000 350.0
18.000000 350.0
19.000000 350.0
20.000000 350.0
21.000000 350.0
22.000000 350.0
23.000000 350.0
24.000000 350.0
25.000000 350.0
30.000000 350.0
35.000000 350.0
40.000000 350.0
45.000000 350.0
50.000000 350.0
```

```
70.000000 350.0
100.000000 350.0
```

5) Sensor response function file (.sen)

User Specified

```
6
1.0
0.0
1.0000000
1.0000000
1.0000000
1.0000000
1.0000000
1.0000000
1.0000000
```

6) Scene node file (.snd)

User Specified

```
10.000
40.0000
52.0000
0.5000
750.0
1250.0
100.0
6
24
87
17.00
39.773333
84.108888
```

7) Emissivity file (.ems) (new asphalt)

Supplied Database

```
0
39850 1.000000
39750 1.000000
39650 1.000000
39550 1.000000
39450 1.000000
39350 1.000000
39250 1.000000
39150 1.000000
39050 1.000000
38950 1.000000
38850 1.000000
38750 1.000000
.
.
.
1450 1.000000
1350 1.000000
1250 0.961000
1150 0.961000
1050 0.961000
950 0.961000
```

```

850 0.961000
750 0.961000
650 1.000000
550 1.000000
450 1.000000
350 1.000000
1
39850 1.000000
39750 1.000000
39650 1.000000
39550 1.000000
39450 1.000000
39350 1.000000
39250 1.000000
.
.
.
550 1.000000
450 1.000000
350 1.000000
.
.
.
.
90
39850 1.000000
39750 1.000000
39650 1.000000
39550 1.000000
39450 1.000000
39350 1.000000
39250 1.000000
.
.
.
1050 0.000000
950 0.000000
850 0.000000
750 0.000000
650 1.000000
550 1.000000
450 1.000000
350 1.000000

```

8) Spectral extinction coefficient file (.ext) (cumulus cloud)

Supplied Database

```

25.8
39850 20.470046
39750 20.381773
39650 20.427239
39550 20.519245
39450 20.506844
39350 20.530237
39250 20.608827
39150 20.519522
39050 20.642167
38950 20.752690
38850 20.759873
38750 20.828176
38650 20.725438
.
.
.
1350 32.444673
1250 33.563504

```

```

1150 33.793211
1050 31.616106
950 25.977480
850 22.136326
750 24.989100
650 26.290338
550 30.210459
450 6.919597
350 0.000000

```

9) Weather history file (.wth) (23 June 1992)

User Specified

```

193      0.25
0.00    7.8    1.0156e+3    .930    -1    1      0    0      0.0    5    1    .025    7
0.25    7.8    1.0156e+3    .930    -1    1      0    0      0.0    5    1    .025    7
0.50    7.8    1.0157e+3    .930    -1    1      0    0      0.0    5    1    .025    7
0.75    7.8    1.0158e+3    .930    -1    1      0    0      0.0    5    1    .025    7
1.00    7.8    1.0158e+3    .930    -1    1      0    0      0.0    5    0    0      0
1.25    7.8    1.0159e+3    .930    -1    1      0    0      0.0    5    0    0      0
1.50    7.8    1.0159e+3    .930    -1    1      0    0      0.0    5    0    0      0
1.75    7.8    1.0160e+3    .930    -1    1      0    0      0.0    5    0    0      0
2.00    7.8    1.0160e+3    .930    -1    1      0    0      0.0    5    0    0      0
2.25    7.7    1.0160e+3    .930    -1    1      0    0      0.0    5    0    0      0
2.50    7.6    1.0160e+3    .930    -1    1      0    0      0.0    5    0    0      0
.
.
.
45.00   16.1    1.0111e+3    .512    -1    0.02    0    0      0.0    6    1    .0254   12
45.25   16.4    1.0111e+3    .559    -1    0.00    0    0      0.0    6    1    .0254   12
45.50   14.9    1.0110e+3    .675    -1    0.00    0    0      0.0    6    1    .0254   12
45.75   13.9    1.0110e+3    .760    -1    0.00    0    0      0.0    6    1    .0254   12
46.00   14.0    1.0110e+3    .810    -1    0.00    0    0      0.0    6    1    .0254   12
46.25   13.9    1.0110e+3    .822    -1    0.00    0    0      0.0    6    0    0      0
46.50   13.9    1.0107e+3    .840    -1    0.00    0    0      0.0    6    0    0      0
46.75   13.6    1.0105e+3    .810    -1    0.00    0    0      0.0    6    0    0      0
47.00   13.8    1.0101e+3    .763    -1    0.01    0    0      0.0    6    0    0      0
47.25   13.9    1.0100e+3    .787    -1    0.00    0    0      0.0    6    0    0      0
47.50   13.5    1.0098e+3    .770    -1    0.01    0    0      0.0    6    0    0      0
47.75   13.7    1.0098e+3    .710    -1    0.02    0    0      0.0    6    0    0      0
48.00   13.9    1.0098e+3    .687    -1    0.00    0    0      0.0    6    0    0      0

```

10) Materials database file (.mat)

Supplied Database

```

48
cloud
0
1.0
5.0
1.0
0.0
0.5
0.96
-0.5
cumulus_cloud.ems
cumulus_cloud.ext
painted_steel_roof
1
.1111
464.4
7.833
1.0

```



```
0.60
0.90
0.50
radome_paint6.ems
radome_paint6.ext
water
2
1.0
5.13
1.0
1.0
0.50
0.96
-0.40
water.ems
water.ext
painted_wood
.
.
.
pine_tree
45
1.0
0.0
1.0
0.0
0.9
0.96
0.17
pine_tree.ems
pine_tree.ext
corn_field
46
1.0
0.0
1.0
0.0
0.9
0.96
0.17
corn_field.ems
corn_field.ext
scrub_oak
47
1.0
0.0
1.0
0.0
0.9
0.96
0.17
scrub_oak.ems
scrub_oak.ext
```

APPENDIX B SPECTRAL EXTINCTION FOR CLOUDS

The spectral extinction coefficients for the different cloud types model in the LOWTRAN7 code were determined using the following procedure:

- 1) Run LOWTRAN7 to compute the transmission through the atmosphere with a clear sky,
- 2) Run LOWTRAN7 to compute transmission through the atmosphere and a cloud layer of type i with a thickness z_i , and
- 3) Derive the spectral extinction coefficient, $\beta_i(\nu)$, as

$$b_{ICLD}(\nu) = -\frac{\ln\left(\frac{t_{ICLD}}{t_{NC}}\right)}{z_{ICLD}}, \quad \text{B-1}$$

where t_{NC} is the transmission through atmosphere with no clouds, t_{ICLD} is the transmission through atmosphere with a cloud of type ICLD present, and z_{ICLD} is the thickness of the cloud layer. The thickness value used in LOWTRAN7 and Equation B-1 are summarized in Table B-1.

Table B-1 Thickness of the default cloud layers used in the LOWTRAN 7 code.

Cloud Type	Thickness (km)
Cumulus	2.34
Altostratus	0.67
Stratus	0.60
Stratocumulus	1.34
Nimbostratus	0.50

This procedure was carried out by running LOWTRAN7 at different times of the day, days of the year, aerosol compositions, seasons and geographic locations. The extinction coefficients computed for these different scenarios were found to be within 2% of each other, showing consistency in the LOWTRAN7 cloud models under different scenarios.

Figures B-1 and B-2 show the extinction coefficients derived using a rural extinction, mid-latitude summer scenario in LOWTRAN7. Figure B-1 shows the extinction coefficients of each cloud

layer over the entire range of the spectrum covered by the DIRSIG model. Figure B-2 examines more closely those regions where the extinction coefficient values fall to zero. These regions correspond to those regions where transmittance through the atmosphere falls to zero (absorption lines). In these areas, Equation B-1 fails due to the extremely small magnitude of the transmission values leading to round-off error (32-bit floating point representation was used).

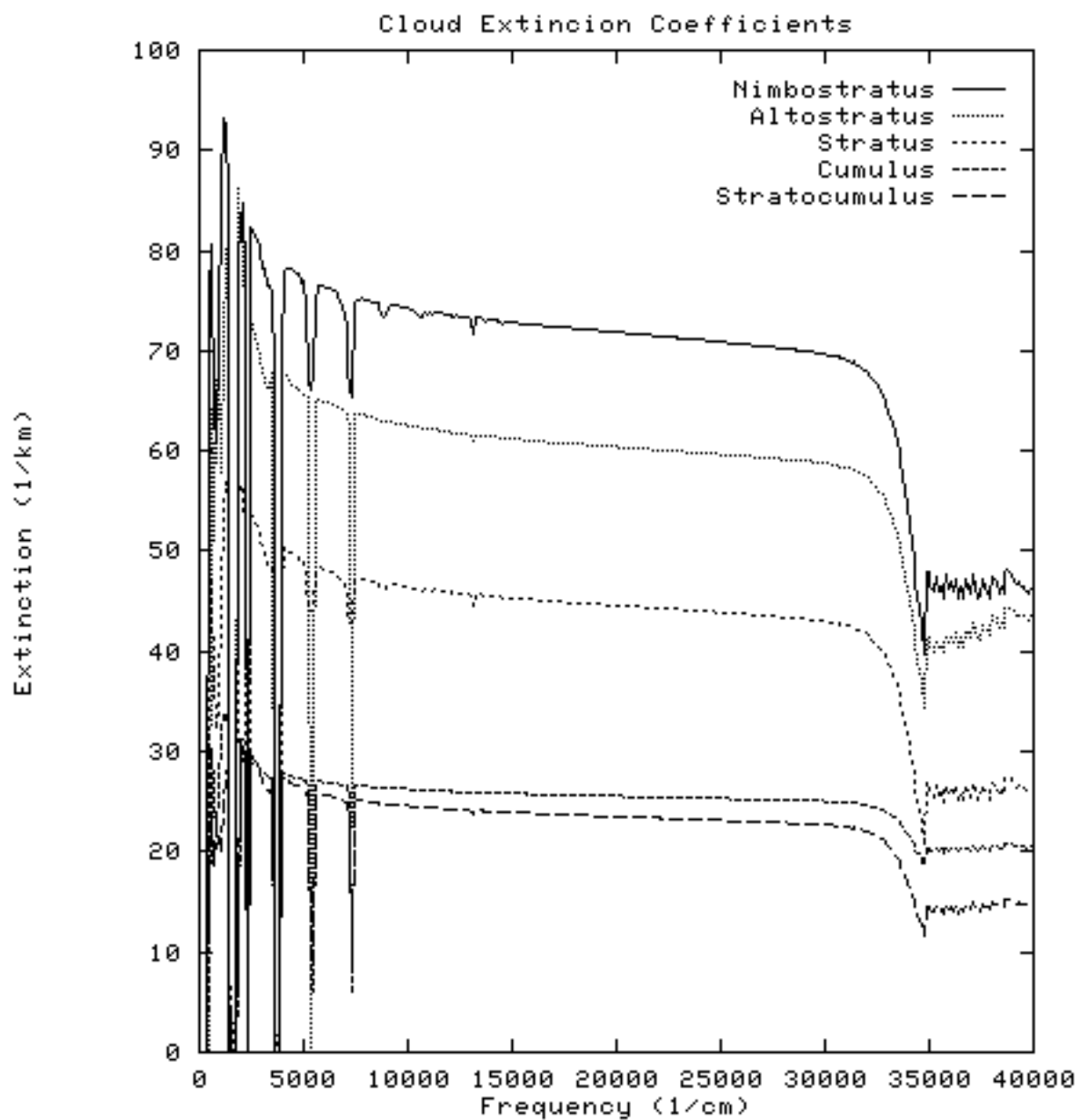


Figure B-1 Extinction coefficients derived for the different cloud types modeled in LOWTRAN7 code.

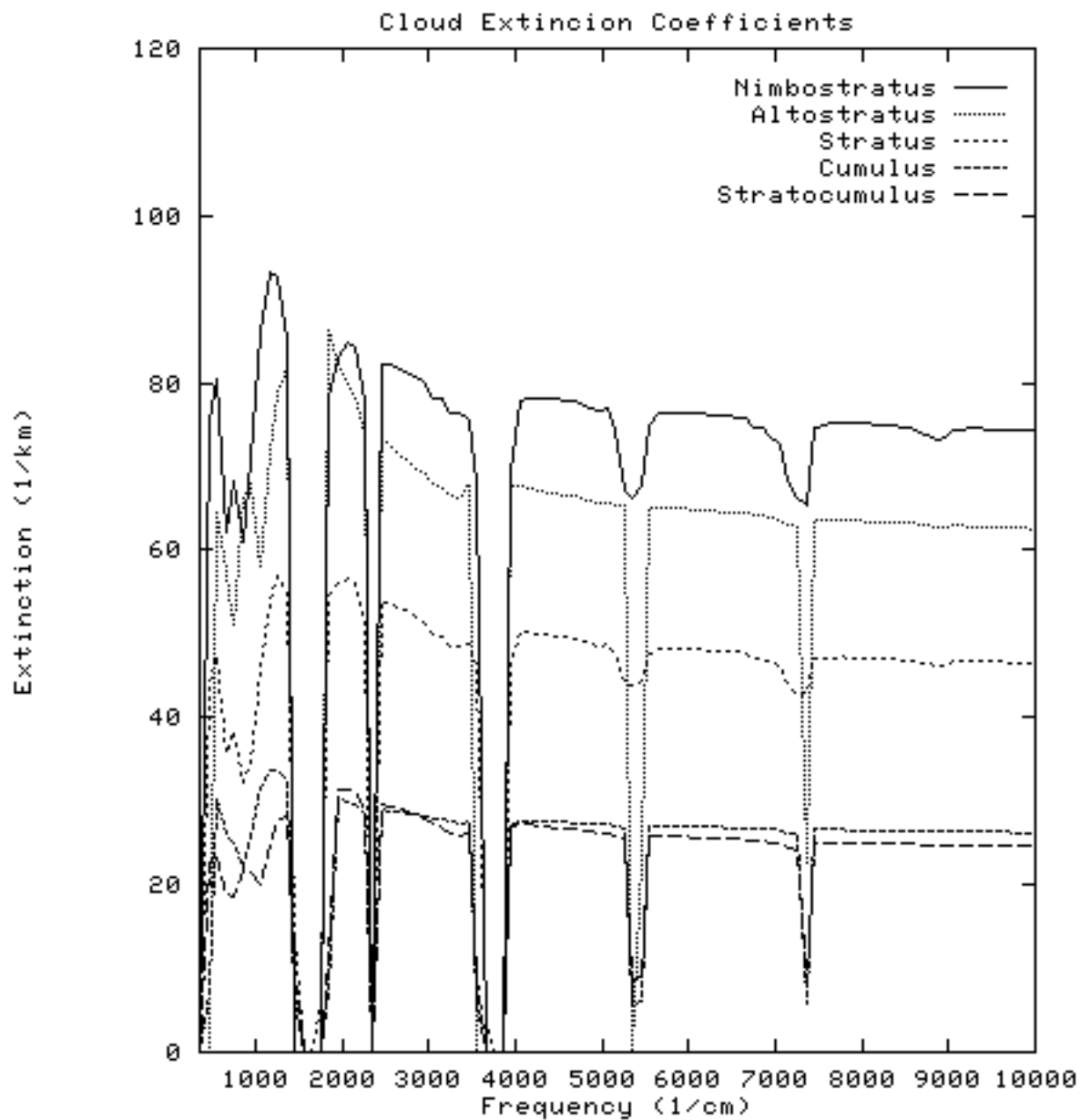


Figure B-2

Extinction coefficients derived for the different cloud types modeled in LOWTRAN7 code emphasizing absorption lines in the region between 350 to 10000 cm^{-1} .

APPENDIX C MATERIAL EMISSIVITY CURVES

This appendix presents angular emissivity values for certain material types measured using RIT's normal and angular emissometer. The values are plotted versus zenith angle in Figures B-1 through B-34.

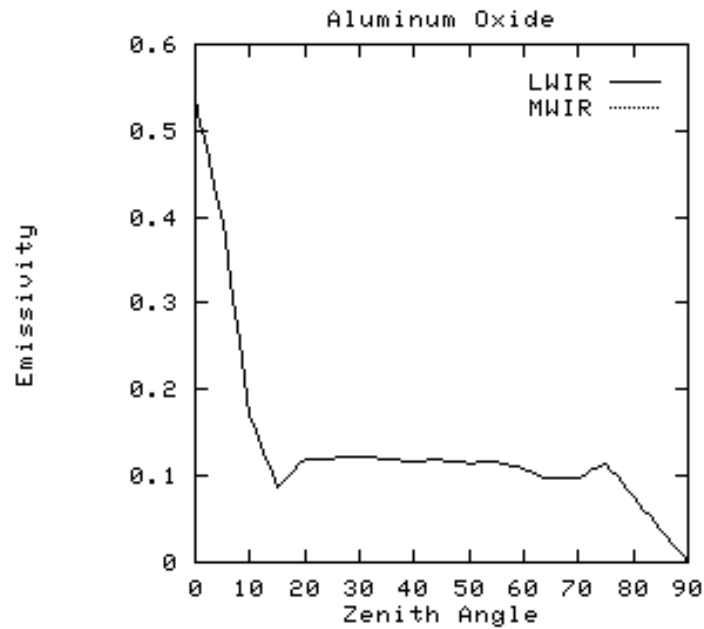


Figure C-1 Aluminum oxide angular emissivity.

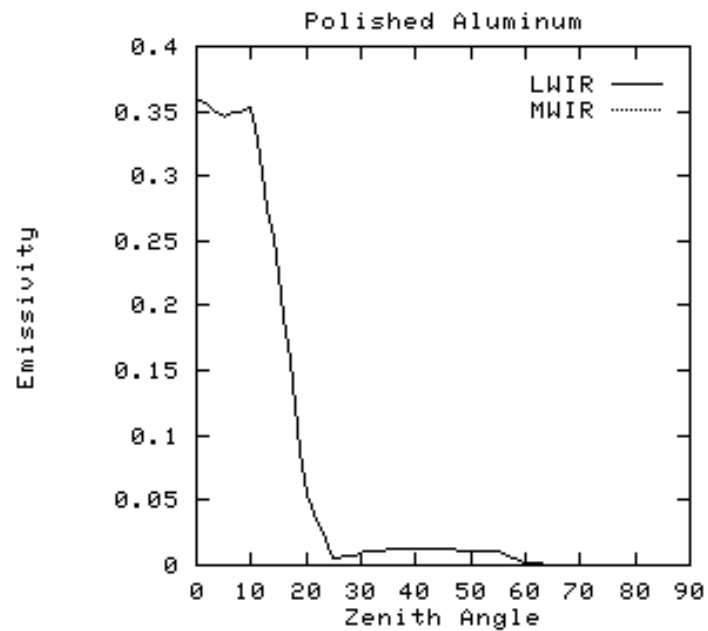


Figure C-2 Polished aluminum angular emissivity.

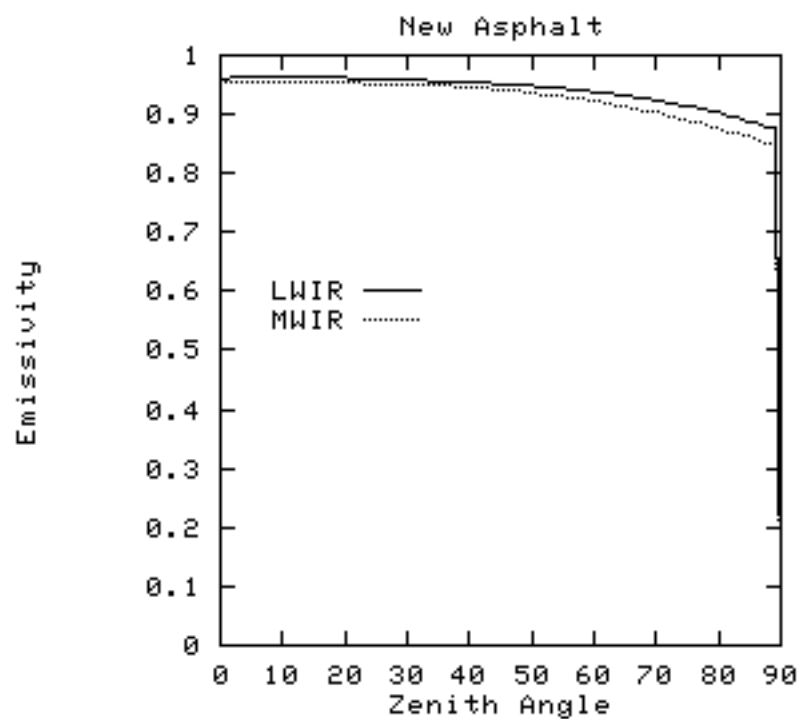


Figure C-3 New asphalt angular emissivity.

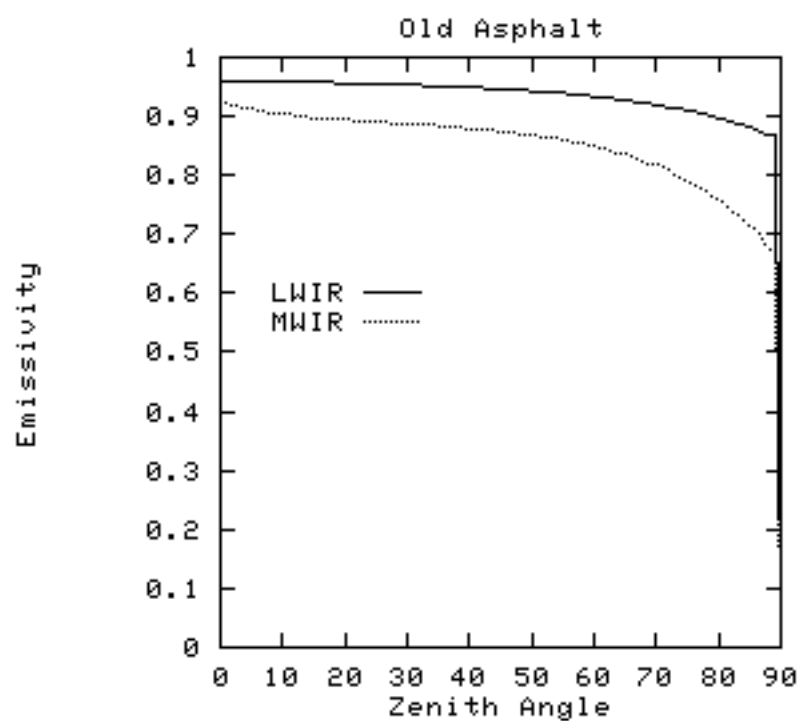


Figure C-4 Old asphalt angular emissivity.

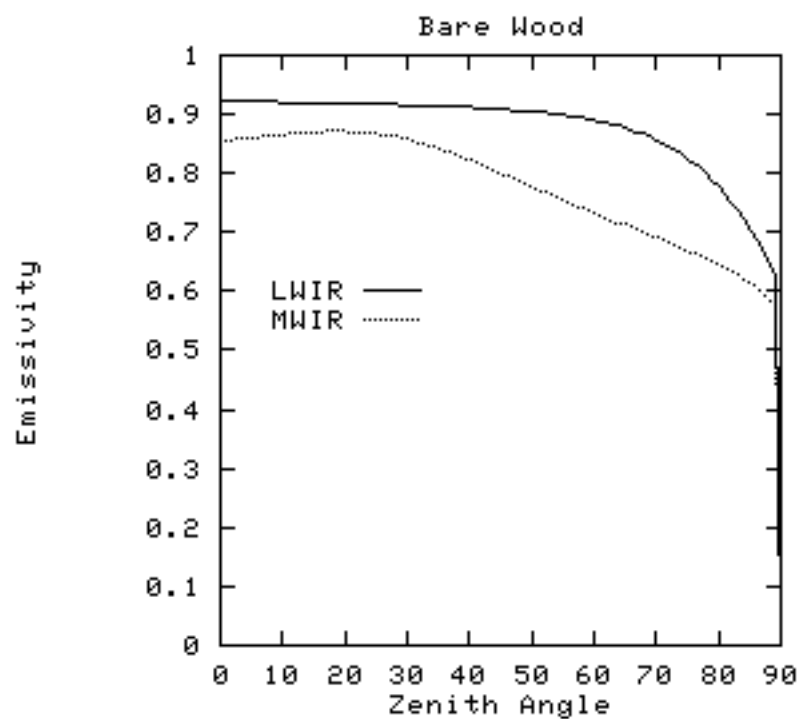


Figure C-5 Bare wood angular emissivity.

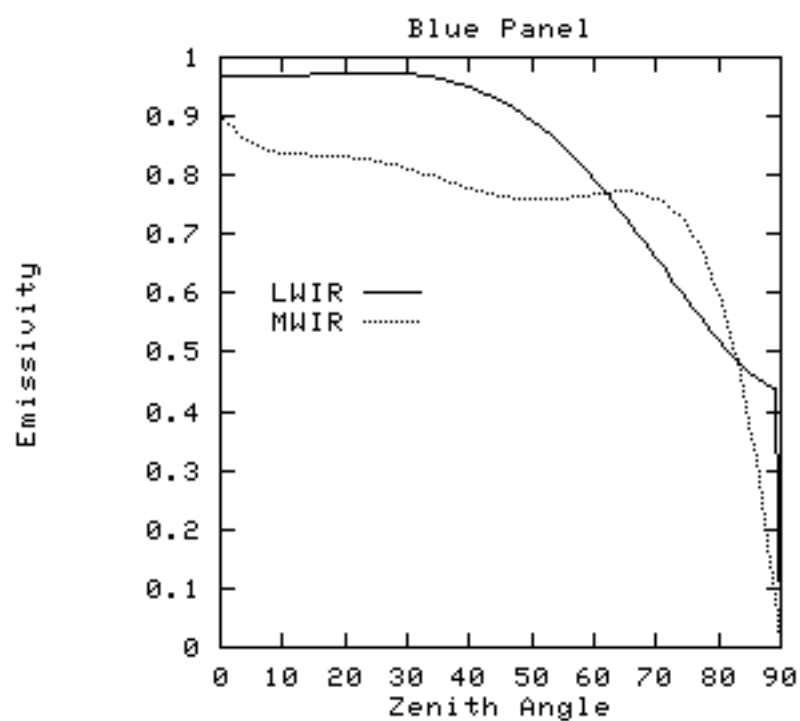


Figure C-6 Blue panel angular emissivity.

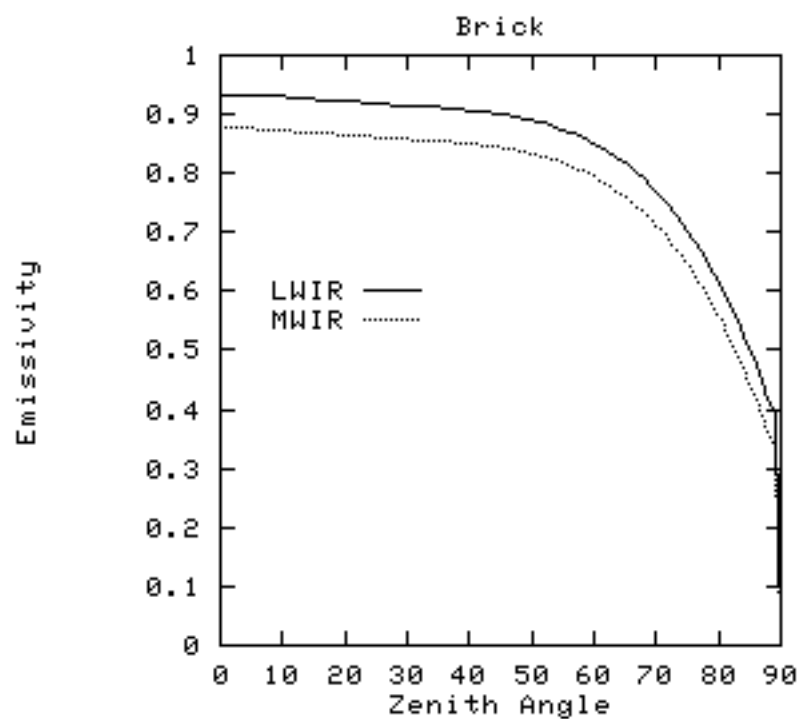


Figure C-7 Brick angular emissivity.

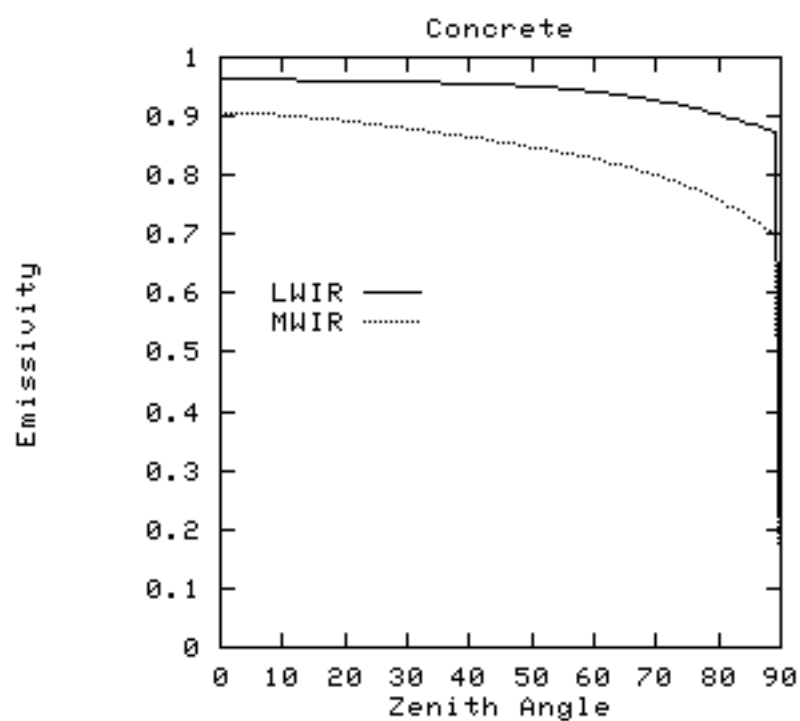


Figure C-8 Concrete angular emissivity.

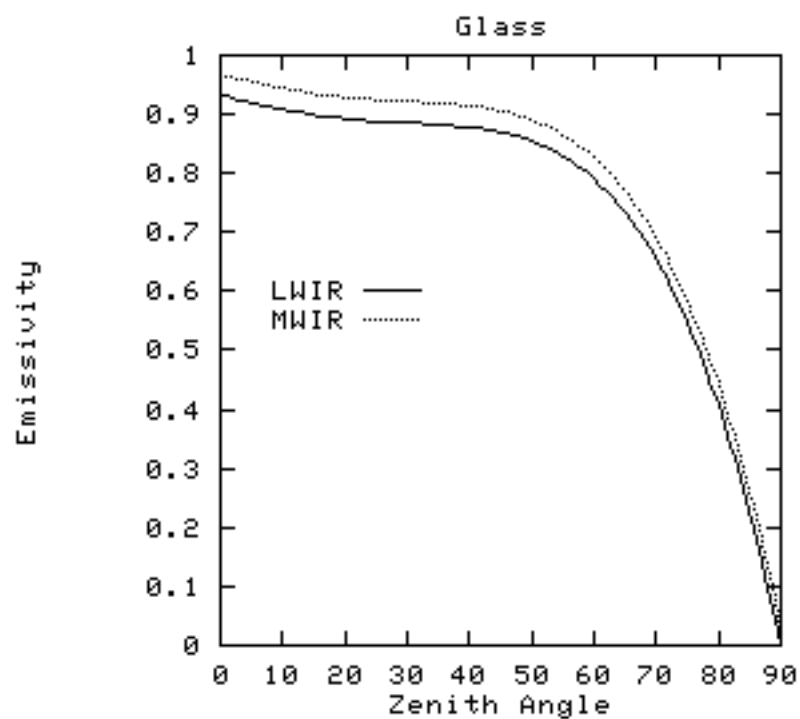


Figure C-9 Glass angular emissivity.

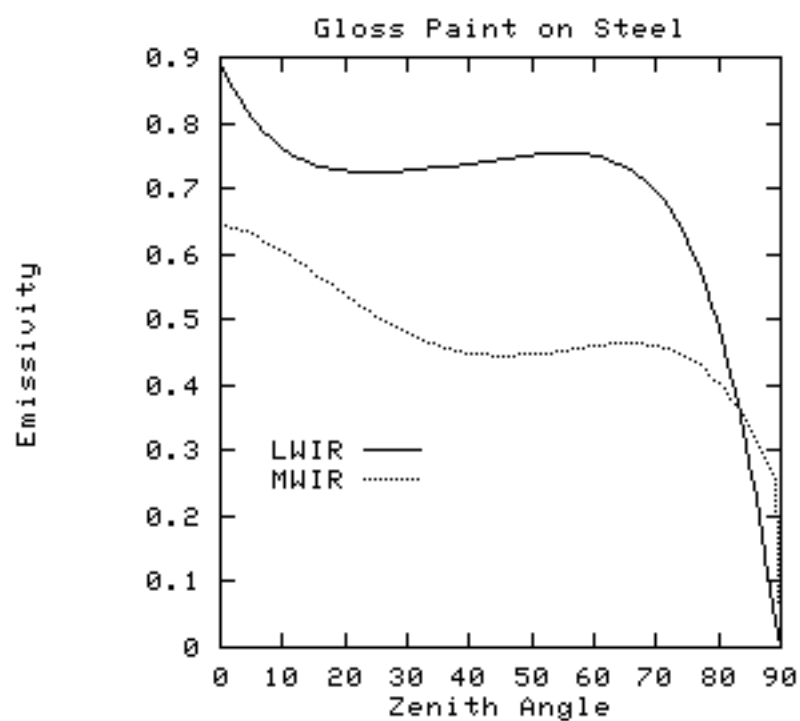


Figure C-10 Gloss paint on steel angular emissivity.

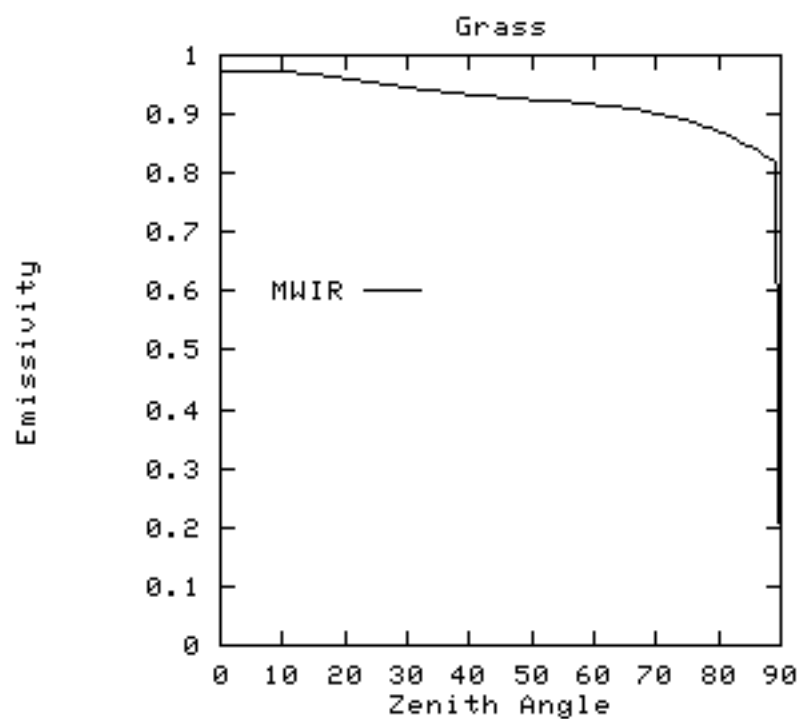


Figure C-11 Grass angular emissivity.

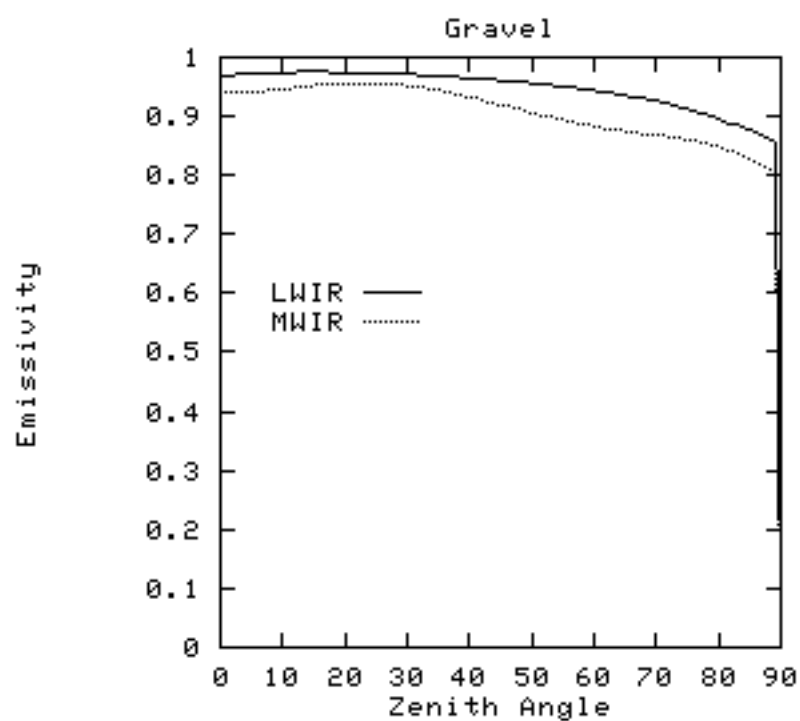


Figure C-12 Gravel angular emissivity.

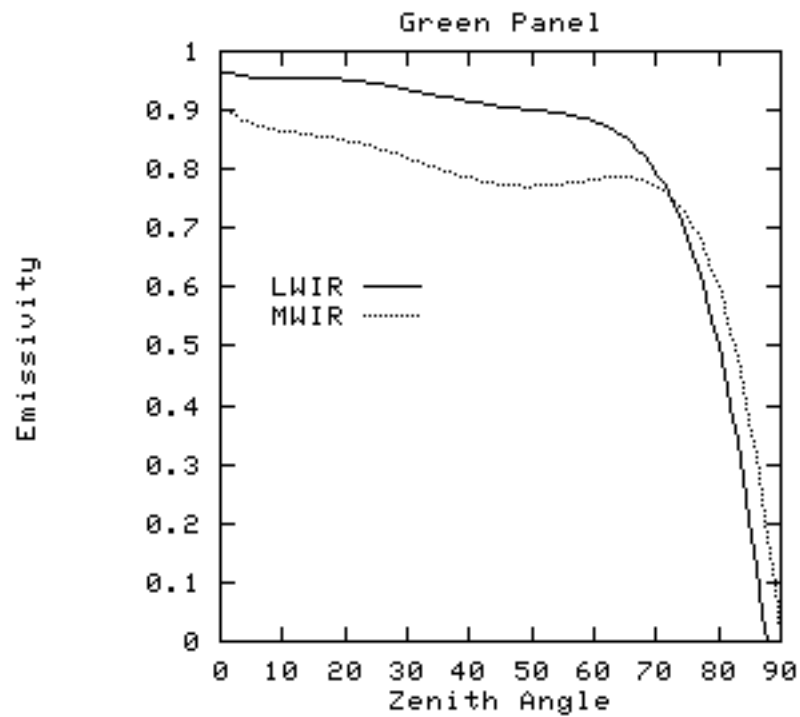


Figure C-13 Green panel angular emissivity.

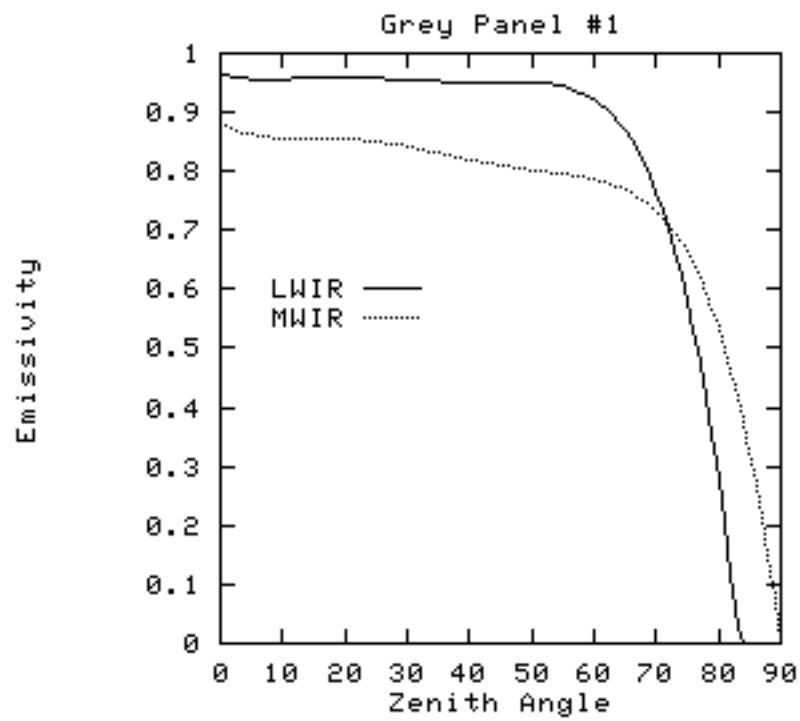


Figure C-14 Grey panel #1 (lightest grey) angular emissivity.

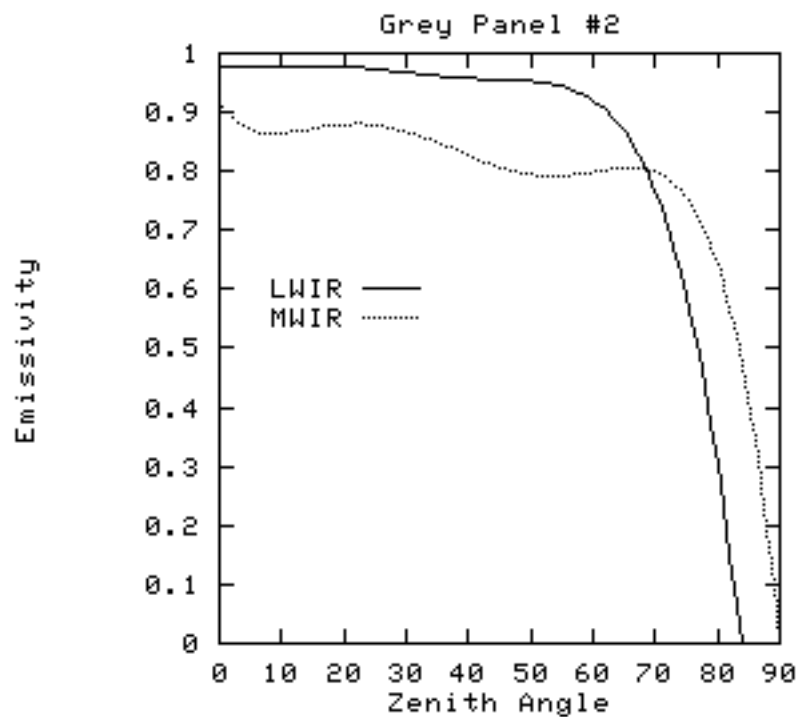


Figure C-15 Grey panel #2 angular emissivity.

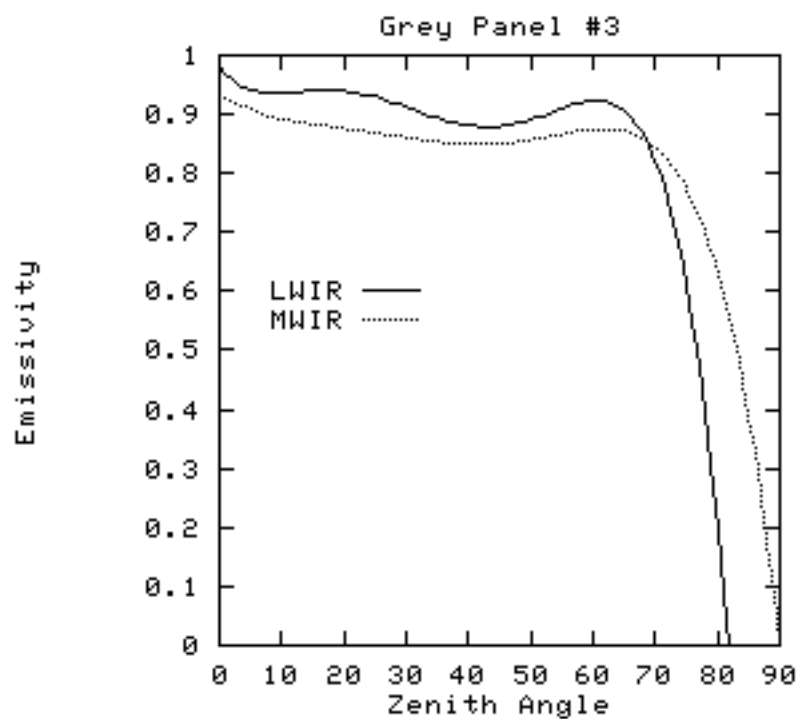


Figure C-16 Grey panel #3 angular emissivity.

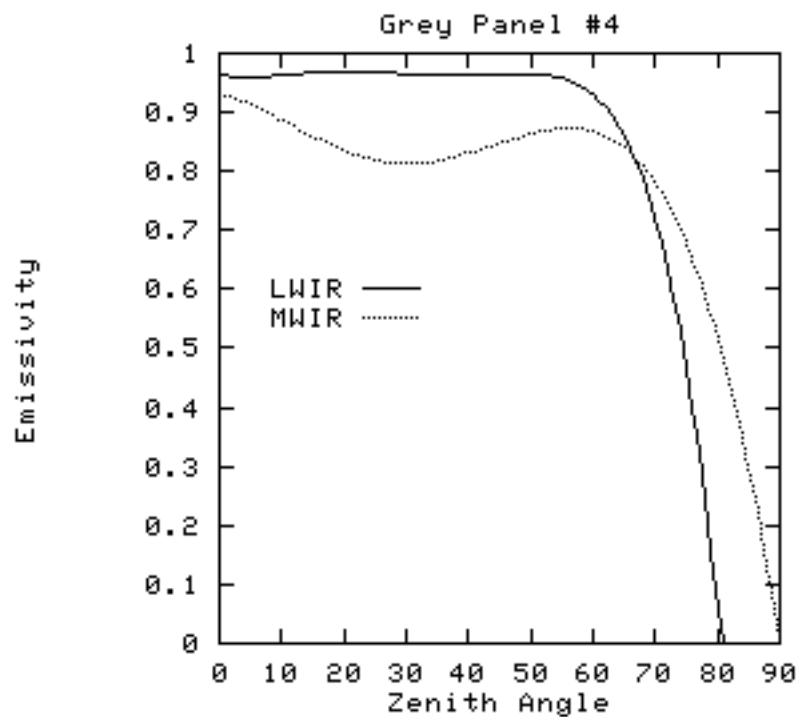


Figure C-17 Grey panel #4 angular emissivity.

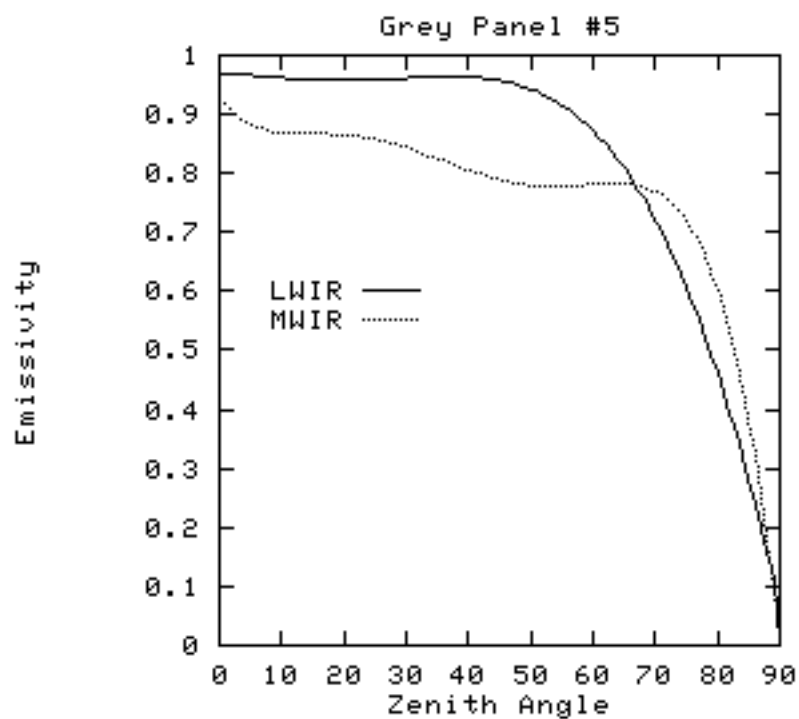


Figure C-18 Grey panel #5 (darkest grey) angular emissivity.

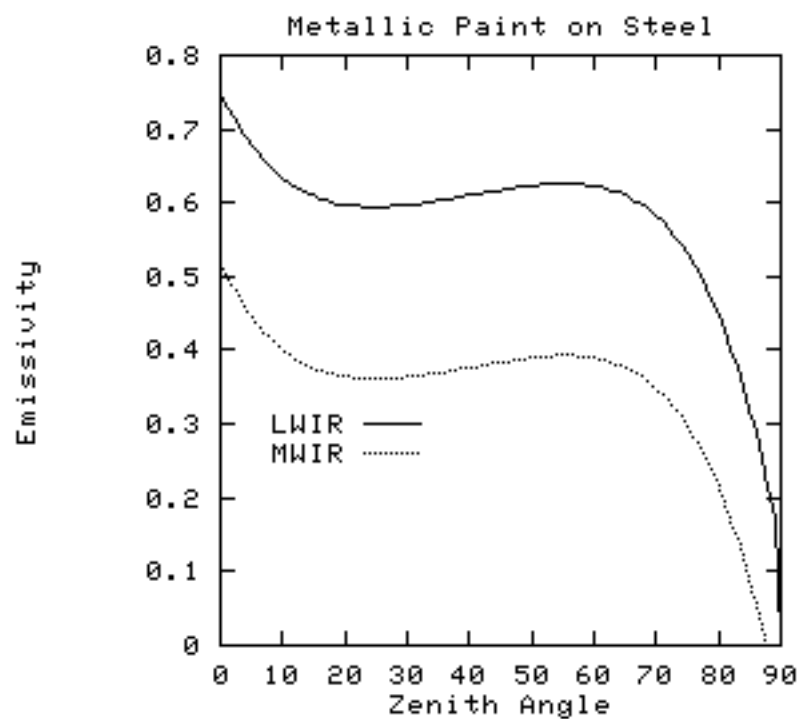


Figure C-19 Metallic paint on steel angular emissivity.

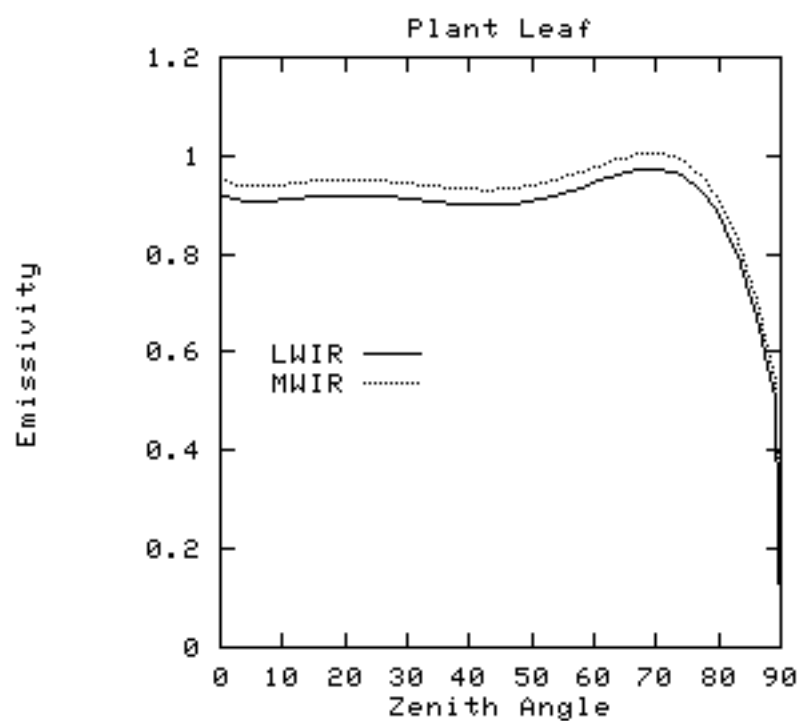


Figure C-20 Plant leaf angular emissivity.

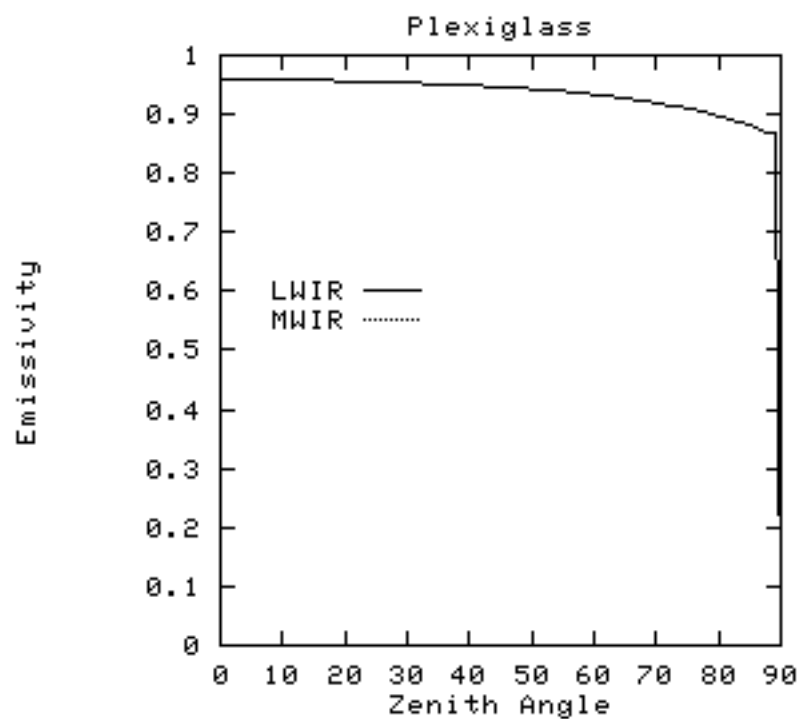


Figure C-21 Plexiglass angular emissivity.

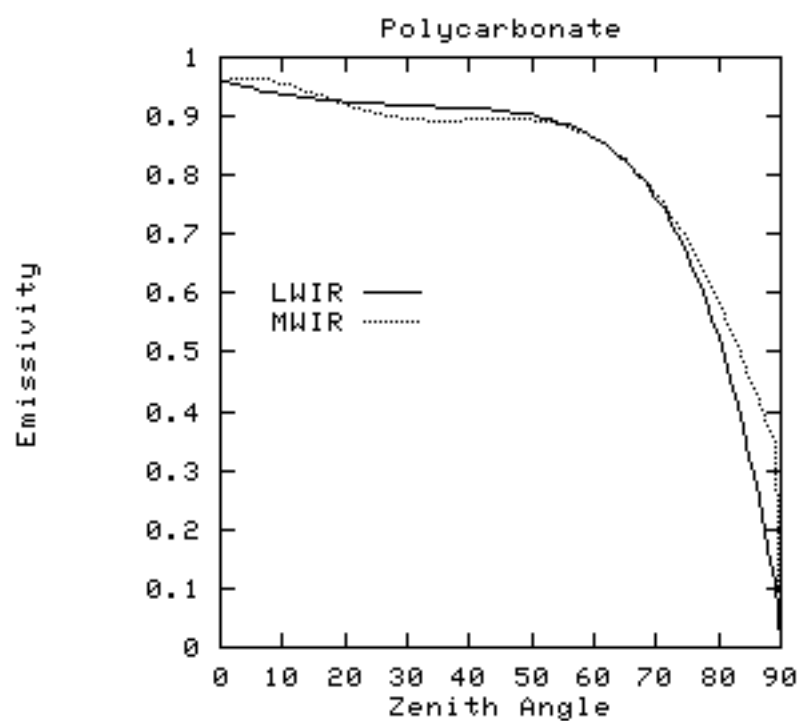


Figure C-22 Polycarbonate angular emissivity.

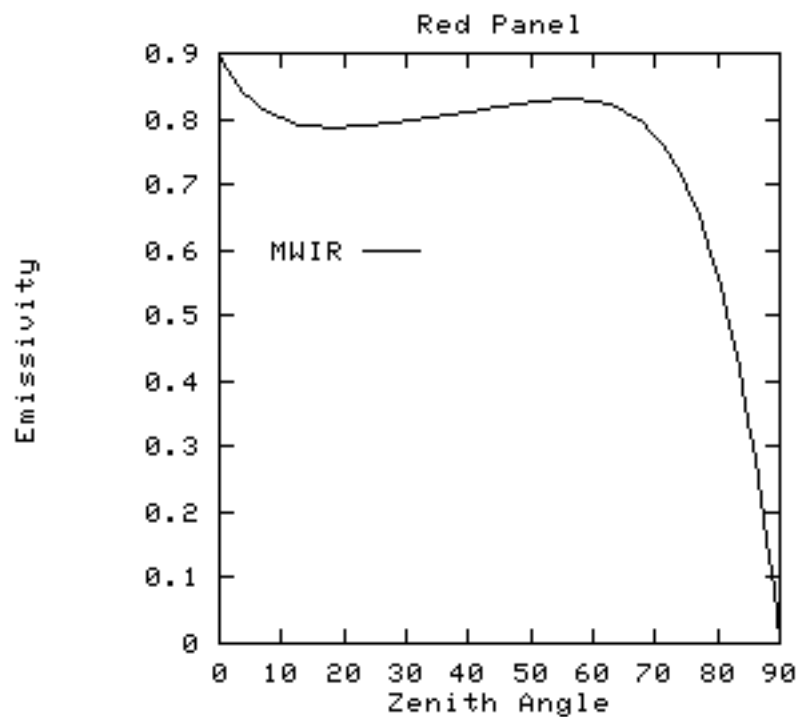


Figure C-23 Red panel angular emissivity.

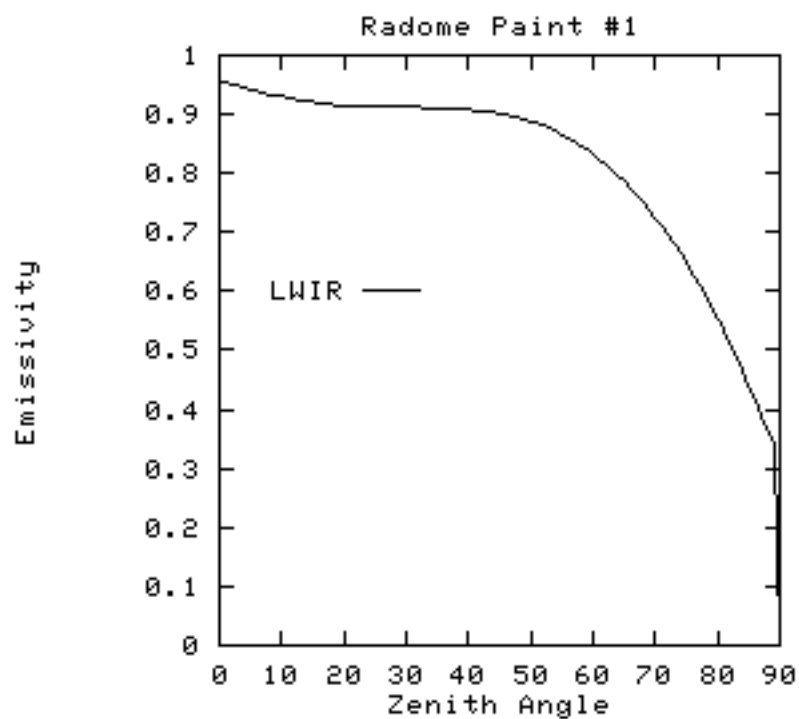


Figure C-24 Radome paint #1 angular emissivity.

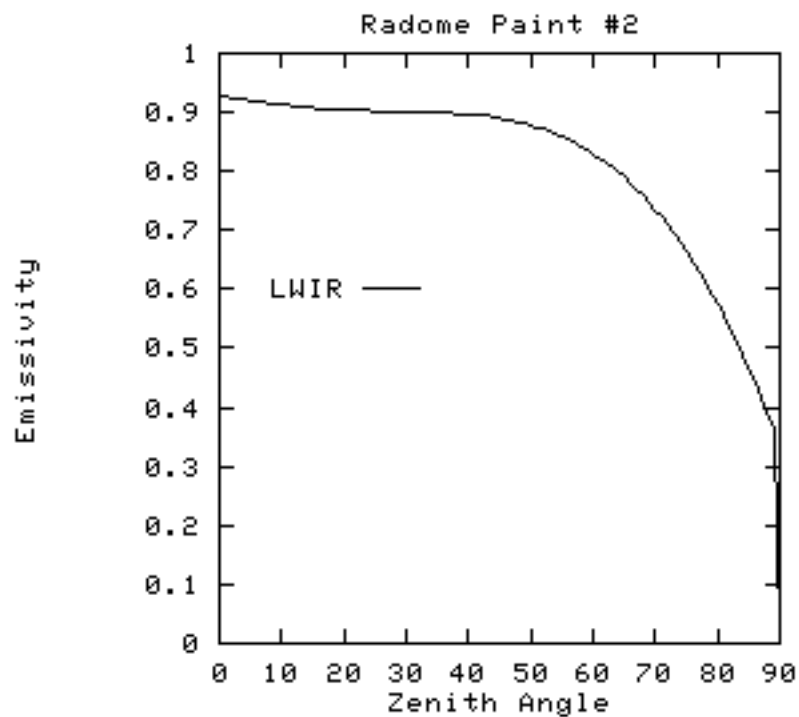


Figure C-25 Radome paint #2 angular emissivity.

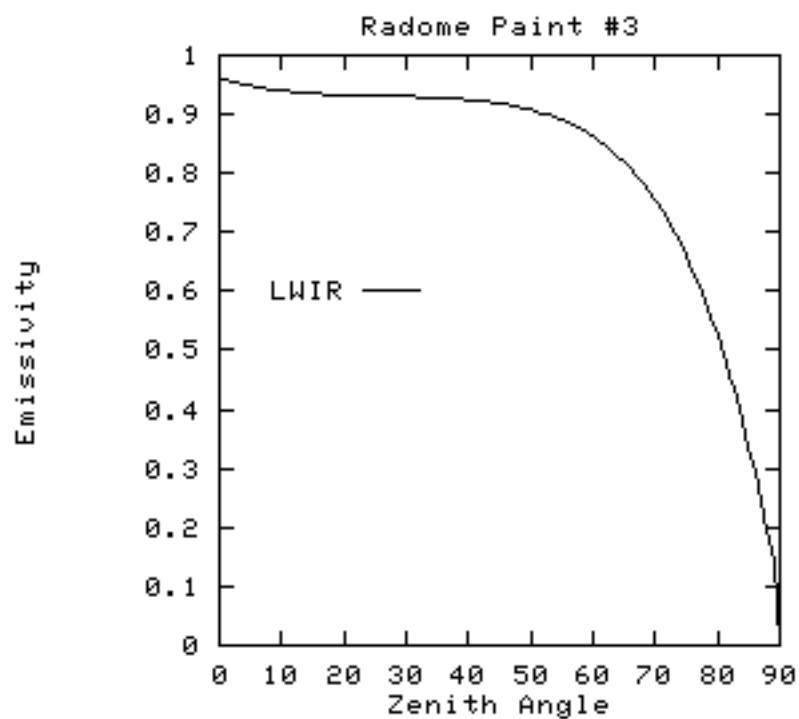


Figure C-26 Radome paint #3 angular emissivity.

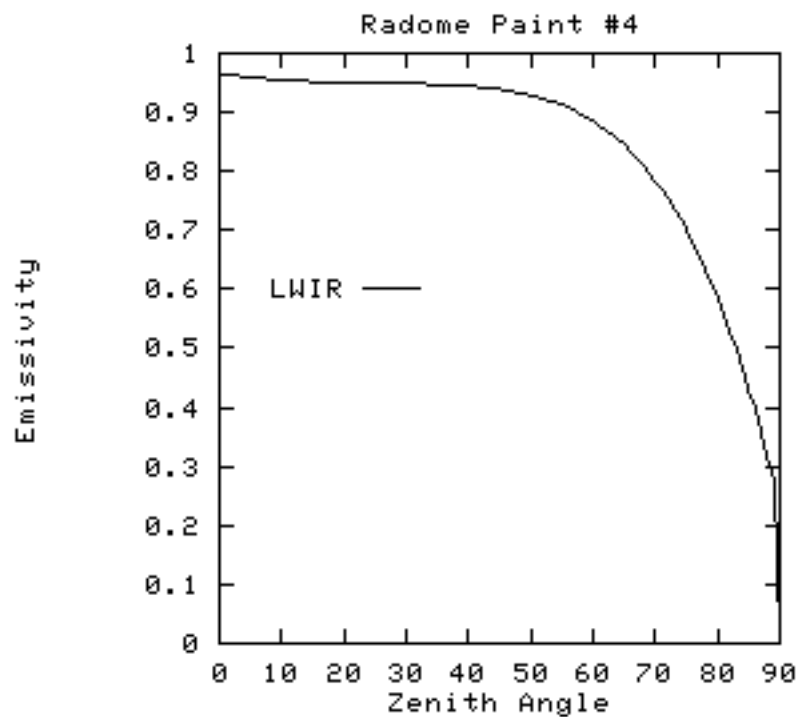


Figure C-27 Radome paint #4 angular emissivity.

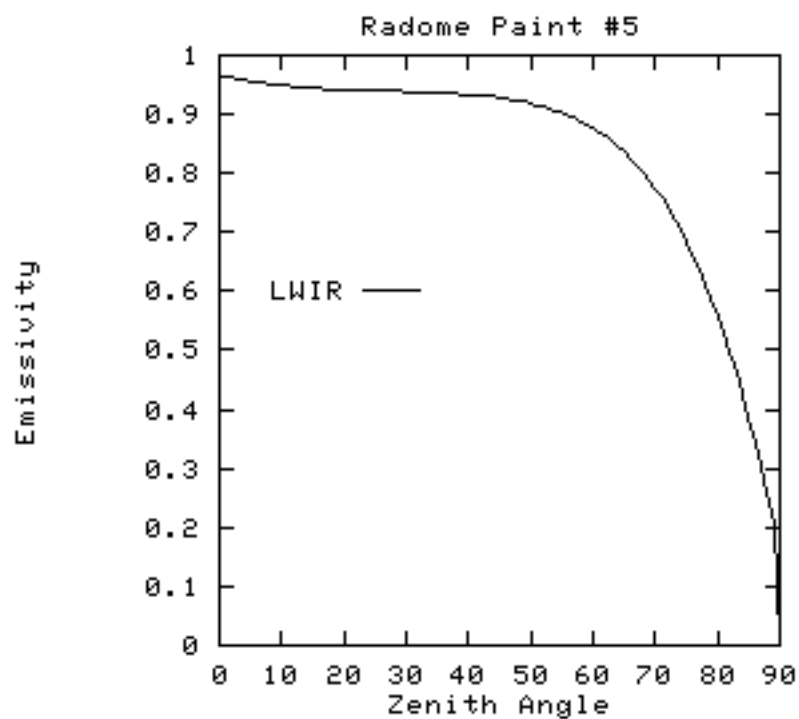


Figure C-28 Radome paint #5 angular emissivity.

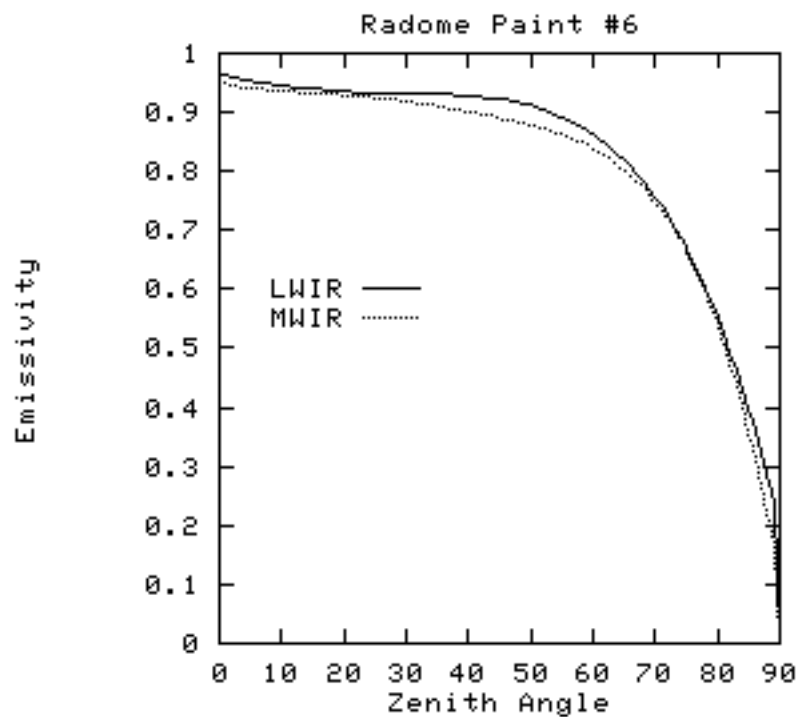


Figure C-29 Radome paint # 6 angular emissivity.

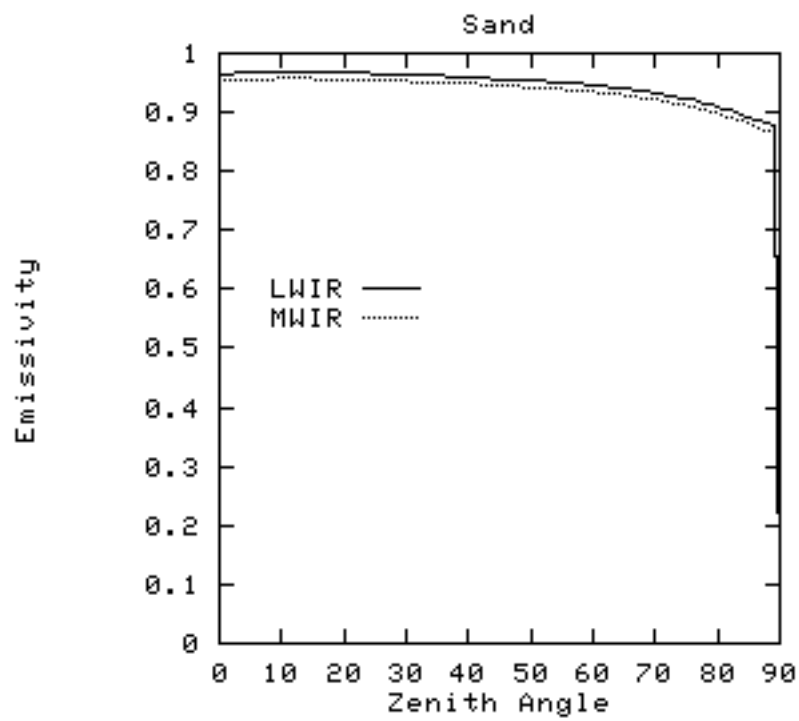


Figure C-30 Sand angular emissivity.

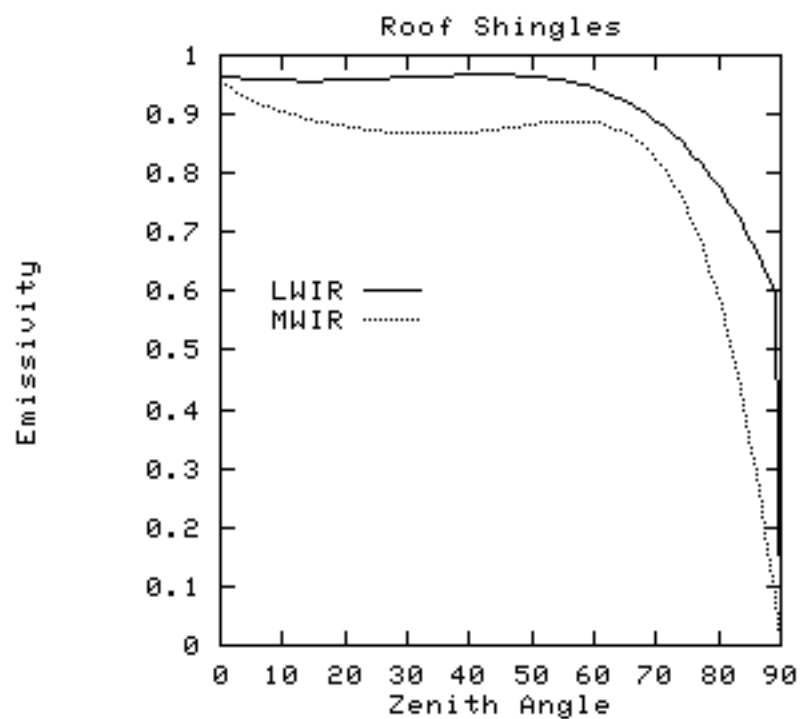


Figure C-31 Roof shingles angular emissivity.

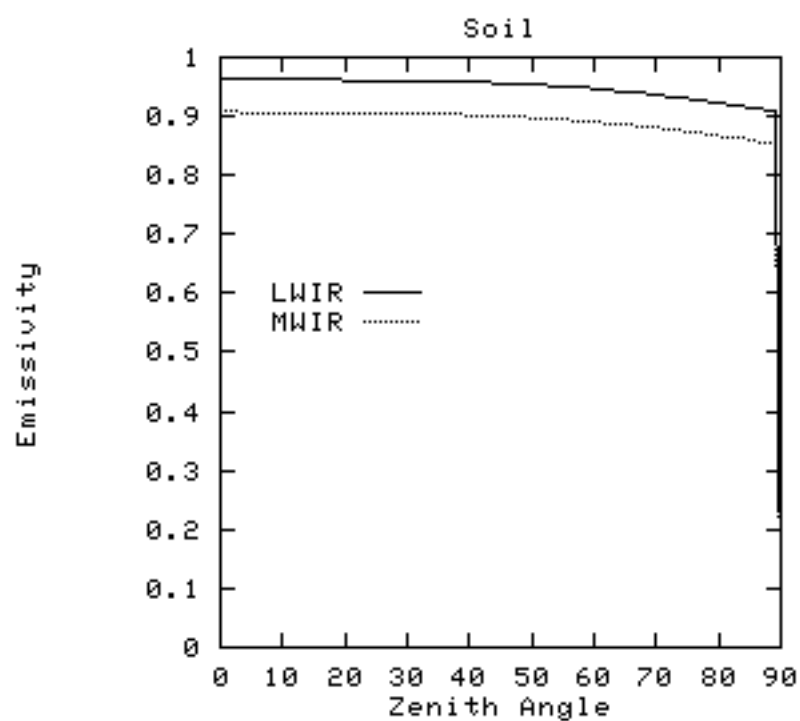


Figure C-32 Soil angular emissivity.

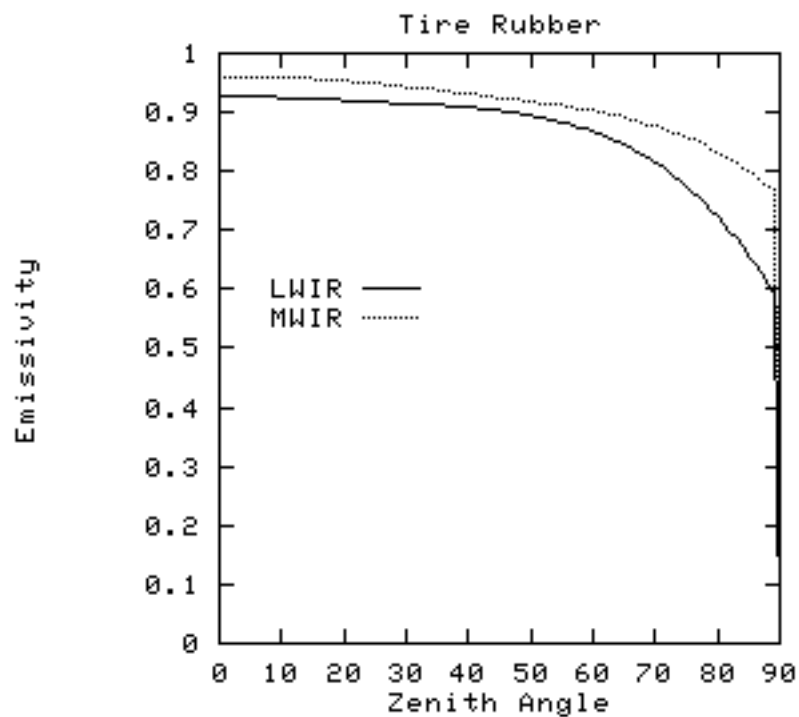


Figure C-33 Tire rubber angular emissivity.

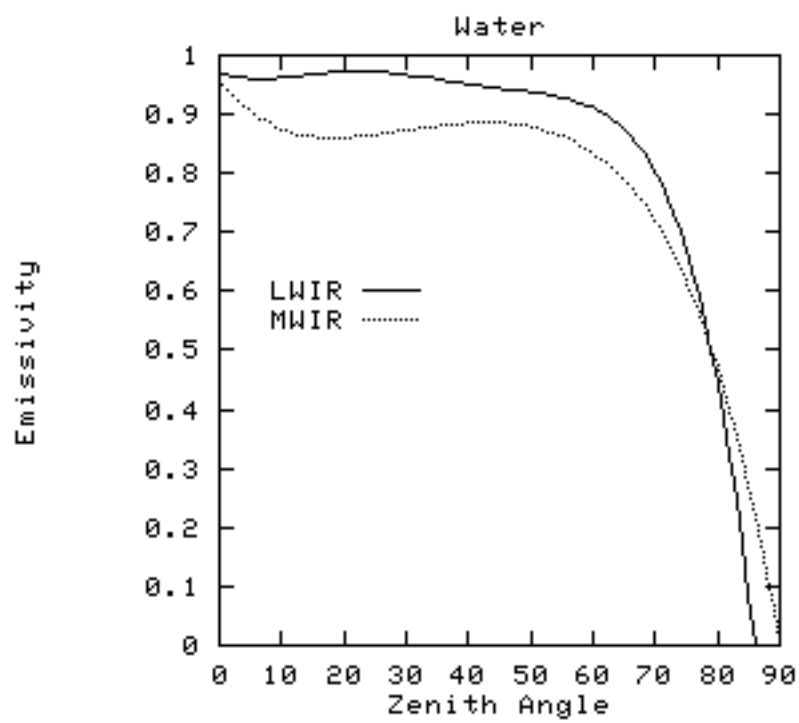


Figure C-34 Water angular emissivity.

APPENDIX D MATERIAL PARAMETERS

Table D-1 Material parameters (June 1992).

Name	Density	Specific Heat	Thermal Conduct.	Thick-ness	Visible Emiss.	Thermal Emiss.	Exposed Area	Self. Power	Slope	Azi-muth
Asphalt	2.114	.22	5.93	2.4	.93	.93	.40	2.2	0	0
Blue Wood	.60	.67	.86	2.4	.60	.78	-.77	0	69	90
Bumper	7.833	.1111	464.4	.12	.88	.44	.69	0	90	90
Car Roof	7.833	.1111	464.4	.09	.88	.44	.53	0	0	0
Car Side	7.833	.1111	464.4	.01	.88	.44	1.0	1.8	90	90
Concrete	2.28	.1601	15.48	4.5	.73	.94	.39	0	0	0
Front Black	.60	.67	.86	2.4	.90	.78	-.77	0	90	90
Front White	.60	.67	.86	2.4	.20	.78	-.77	0	90	90
Green Wood	.60	.67	.86	2.4	.55	.78	-.77	0	69	90
Grey 1	.60	.67	.86	2.4	.50	.78	-.77	0	69	90
Grey 2	.60	.67	.86	2.4	.60	.78	-.77	0	69	90
Grey 3	.60	.67	.86	2.4	.70	.78	-.77	0	69	90
Grey 4	.60	.67	.86	2.4	.80	.78	-.77	0	69	90
Grey 5	.60	.67	.86	6.0	.72	.87	-.55	0	69	90
Red	.60	.67	.86	2.4	.65	.78	-.77	0	69	90
Sand	1.52	.1911	2.84	1.3	.76	.90	.39	0	0	0
Windshield	1.0	.52	12.04	.11	.61	.61	.52	0	17	180
Shingles	1.3	.35	6.36	.05	.74	.91	-.66	0	29	90
Specular	.60	.67	.86	3.0	.72	.87	-.45	0	0	0
Tire	1.198	.2986	1.3	.15	.93	.90	-.82	0	90	90
Water	1.0	1.0	11.0	47.0	.09	.000	-.57	0	0	0
Window	1.0	.52	12.04	.31	.61	.61	.95	.80	67	90

VITA

NAME: Carl Salvaggio

DATE AND PLACE OF BIRTH: January 30, 1963, Perth Amboy, New Jersey.

EDUCATION:

High School, Cedar Ridge High School, Old Bridge, New Jersey, June 1981.

Bachelor of Science, Imaging Science, Rochester Institute of Technology, Rochester, New York, May 1987.

Master of Science, Imaging Science, Rochester Institute of Technology, Rochester, New York, May 1987.

EMPLOYMENT:

Rochester Institute of Technology, 1986-1994, Research Scientist.

Hughes Aircraft Company, 1994-present, Staff Engineer.